Aalto-yliopisto
Insinööritieteiden
korkeakoulu

Erika Toivonen

Physically-based modelling of surface energy fluxes in Australian ecosystems across an aridity gradient

Thesis submitted in a partial fulfillment of the requirements for the degree of Master of Science in Technology.

Espoo, 9.1.2017
Supervisor: Professor Harri Koivusalo
Advisors: D.Sc. (Tech.) Teemu Kokkonen (Aalto University), D.Sc. (Tech.) Kaniska Mallick (Luxembourg Institute of Science and Technology)

Aalto University
School of Engineering

Aalto University, P.O. BOX 11000, 00076 AALTO
www.aalto.fi

Abstract of master's thesis

Author Erika Toivonen

Title of thesis Physically-based modelling of surface energy fluxes in Australian ecosystems across an aridity gradient

Degree programme Civil and Environmental Engineering

Major/minor Water and Environmental Engineering **Code** R3005

Thesis supervisor Professor Harri Koivusalo

Thesis advisors D.Sc. (Tech.) Teemu Kokkonen (Aalto University), D.Sc. (Tech.) Kaniska Mallick (Luxembourg Institute of Science and Technology)

Date 09.01.2017 **Number of pages** 59 + 13 **Language** English

Abstract

Evapotranspiration (ET) is one of the main elements of the water balance after precipitation, and it has an essential role interconnecting energy, water and carbon cycles. Energy flow from the surface as a latent heat flux (λE) connects ET to surface energy balance, and thus to sensible heat flux (H). Understanding of energy and water cycles is important for efficient management of water resources, especially under semi-arid regions, where water availability is one of the key controls on ecosystem processes. Australia is generally a dry continent, where evapotranspiration has been examined by local measurements, including eddy covariance (EC) systems. On the other hand, these methods are not suitable for large-scale monitoring. Instead, remote sensing is the most feasible method to cost-effectively obtain surface energy balance (SEB) fluxes over larger scales. However, some of these models require a large amount of parameterization, which is proven to lead in high uncertainties under water-limited areas.

The main objective of this study was to use a physically-based single-source SEB model, the Surface Temperature Initiated Closure (STIC1.2), to estimate SEB fluxes in Australia across a wide variety of ecohydrologically different sites. STIC1.2 integrates radiometric surface temperature (T_R) measured by thermal infrared remote sensing into a combined Penman-Monteith and Shuttleworth-Wallace equation to analytically retrieve solutions for the SEB fluxes without any land surface parameterization. STIC1.2 was validated against 15 EC towers in Australia over two years 2013 and 2014. The role of ecohydrological differences in determining the errors of the estimated fluxes was identified. The estimates of STIC1.2 were also compared with two SEB models: a modified Priestley-Taylor (PT-JPL) and MODIS global terrestrial evapotranspiration (MOD16) by using MODIS satellite data.

The results showed that STIC1.2 is capable to reliably capture the SEB fluxes across a broad spectrum of ecohydrologically diverse ecosystems in Australia. The accuracy in the STIC1.2 SEB estimates was comparable with PT-JPL, but superior against parameterization dependent MOD16. However, the λE estimates from STIC1.2 showed high uncertainty over water-limited sites, where H was found to be predominant. Therefore, H might be a favoured metric to test the performance of any physically-based model under these conditions. However, a large scale application of STIC1.2 would need more precise satellite-retrieved T_R data. With the availability of more accurate T_R retrieval techniques, e.g. from the recently launched Sentinel-3, an application of STIC1.2 and improvements in the performance over water-stressed ecosystems can be expected.

Keywords Surface energy fluxes, evapotranspiration, land surface temperature, Australia, ecohydrology, Penman-Monteith, Shuttleworth-Wallace

Aalto-yliopisto
Insinööritieteiden
korkeakoulu

Aalto-yliopisto, PL 11000, 00076 AALTO
www.aalto.fi

Diplomityön tiivistelmä

Tekijä Erika Toivonen

Työn nimi Fysikaalisperusteinen maanpinnan energiavirtojen mallintaminen Australian ekosysteemeissä

Koulutusohjelma Yhdyskunta- ja ympäristötekniikan koulutusohjelma

Pää-/sivuaine Vesi- ja ympäristötekniikka **Koodi** R3005

Työn valvoja Professori Harri Koivusalo

Työn ohjaajat TkT Teemu Kokkonen (Aalto-yliopisto), TkT Kaniska Mallick (Luxembourg Institute of Science and Technology)

Päivämäärä 09.01.2017 **Sivumäärä** 59 + 13 **Kieli** Englanti

Tiivistelmä

Haihdunta on yksi tärkeimmistä hydrologisen kierron elementeistä sadannan jälkeen, ja sillä on erityinen rooli energia-, vesi- ja hiilikiertojen yhdistäjänä. Haihdunta voidaan myös käsittää energiavirtana (latenttilämpö, λE), joten se voidaan yhdistää vesitaseen lisäksi energiataseeseen, ja lämmittävään lämpöön (H). Energia- ja vesikiertojen mallintaminen on tärkeää tehokkaalle vesivarojen hallinnalle erityisesti kuivilla alueilla, joissa veden riittävyys on yksi tärkeimmistä ekosysteemin toimintaa rajoittavista tekijöistä. Australia on pääosin kuiva maanosa, jossa haihduntaa on mallinnettu käyttämällä paikallisia mittauksia, kuten *eddy covariance* (EC) -menetelmää. Nämä paikalliset metodit eivät ole käyttökelpoisia haihdunnan laajamittaiseen monitorointiin. Sen sijaan kaukokartoitus on yksi keino mallintaa energiavirtoja kustannustehokkaasti ja laajamittaisesti. Kuitenkin osa näistä malleista vaatii runsaasti parametrisointia, jonka on osoitettu lisäävän mallin epävarmuutta hyvin kuivilla alueilla.

Tämän tutkimuksen tarkoituksena oli käyttää fysikaalisperusteista Surface Temperature Initiated Closure (STIC1.2) -mallia energiavirtojen mallintamiseen Australiassa. STIC1.2-malli perustuu termisen infrapunakaukokartoituksen avulla mitattavan radiometrisen pintalämpötilan (T_R) integroimiseen osaksi Penman-Monteith ja Shuttleworth-Wallace -yhtälökombinaatiota, jotta energiavirtoja (λE ja H) voidaan mallintaa analyyttisesti ilman mallin parametrisointia. Työn päätavoitteena oli validoida STIC1.2-malli vuosina 2013 ja 2014 käyttämällä 15 Australiassa sijaitsevaa EC-asematornia sekä tunnistaa miten alueelliset ekohydrologiset erot vaikuttavat energiavirtaestimaattien virhelähteisiin. Lisäksi STIC1.2-mallin tuloksia verrattiin kahteen haihduntamalliin: muunneltuun Priestley-Taylor (PT-JPL) ja MOD16-malleihin käyttämällä MODIS-satelliittidataa.

Tulosten perusteella STIC1.2-mallin avulla voidaan luotettavasti mallintaa energiavirtoja ekohydrologisesti erilaisissa Australian ekosysteemeissä. STIC1.2:n mallinnustulosten tarkkuus oli verrattavissa PT-JPL-mallin tuloksiin, mutta oli ylivertainen MOD16-malliin verrattuna. STIC1.2:n avulla mallinnetut kuivien alueiden λE-estimaatit sisälsivät kuitenkin paljon epävarmuutta. Vesiniukoissa ekosysteemeissä H-komponentti oli vallitseva, jolloin sitä voitaisiin näissä olosuhteissa käyttää fysikaalisperusteisten haihduntamallien toiminnan testaamisen λE:n sijaan. Laajamittaisen STIC1.2-sovelluksen käyttöönotto vaatisi kuitenkin tarkempia T_R-estimaatteja. Esimerkiksi hiljattain laukaistusta Sentinel3-satelliittista saatava T_R-aineisto mahdollistanee STIC1.2-mallin laajamittaisemman hyödyntämisen myös vesiniukoilla alueilla.

Avainsanat pintaenergiavirrat, haihdunta, pintalämpötila, Australia, ekohydrologia, Penman-Monteith, Shuttleworth-Wallace

Acknowledgements

This thesis was conducted in collaboration with Luxembourg Institute of Science and Technology (LIST) in Luxembourg in the Water Safety and Security Unit at the Department of Environmental Research and Innovation (ERIN) as a part of the Remote Sensing and Ecohydrological Modelling research group. First, I would like to thank LIST for this exquisite opportunity to work in Luxembourg with a very skilled team of researchers. Furthermore, I am grateful for the funding provided by Erasmus+, Maa- ja vesitekniikan tuki ry, Sven Hallinin tutkimussäätiö as well as Vesitekniikan kehittämisrahasto, which all made this experience possible.

I want to thank my supervisor Professor Harri Koivusalo and advisor Dr. Teemu Kokkonen from the Department of Built Environment at Aalto University School of Engineering for the guidance during this study. Especially, I would warmly like to thank my advisor from LIST, Dr. Kaniska Mallick, for encouragement, support and patience throughout this thesis work. Likewise, I appreciate my coworkers' positive attitude and peer support, which made working at LIST very delightful. I also acknowledge the helpful advice from Australian OzFlux site PI:s.

Special thanks are extended to my family and friends, for support during my whole studies. Besides, I want to thank Pierre-Emmanuel, I appreciate your warm support for this project.

Espoo 09.01.2017

Erika Toivonen

Table of contents

Notations

A_c	(W m^{-2})	Energy received by canopy
A_{SOIL}	(W m^{-2})	Energy received by soil
C_C	(s m^{-1})	Canopy conductance
C_L	(s m^{-1})	Mean potential conductance per unit leaf area
C_S	(s m^{-1})	Stomatal conductance
D_0	(hPa)	Atmospheric vapor pressure deficit at the source/sink height
D_A	(hPa)	Saturation deficit of the air
$D_{A_{open}}$	(Pa)	Variable in MOD16 (Saturation deficit of the air)
$D_{A_{close}}$	(Pa)	Variable in MOD16 (Saturation deficit of the air)
E	(mm)	Evapotranspiration (evaporation + transpiration) as a depth of water
E_p	(mm)	Potential evapotranspiration as a depth of water
E^*_{PM}	(mm)	Potential evapotranspiration as a depth of water according to Penman-Monteith
E^*_{PT}	(mm)	Potential evapotranspiration as a depth of water according to Priestley-Taylor
F_{in}	(mm/timestep)	Inflow of E to the surface
F_{out}	(mm/timestep)	Outflow of E from the surface
G	(W m^{-2})	Ground heat flux
G_{CU}	(s m^{-1})	Leaf cuticular conductance
Gl_{sh}	(m s^{-1})	Leaf conductance to sensible heat per unit LAI
G_S^2	(s m^{-1})	Leaf boundary-layer conductance
G_{Sday}	(s m^{-1})	Daytime stomatal conductance

H	(W m^{-2})	Sensible heat flux
LAI	Unitless	Leaf area index
M	Unitless	Relative wetness of the surface
$MAPD$	(%)	Mean absolute percentage deviation
$NDVI$	Unitless	Normalized difference vegetation index
$\overline{O}$	(W m^{-2})	Mean of observed values
O_i	(W m^{-2})	Observed value
P	(mm)	Precipitation
$\widehat{P}_i$	(W m^{-2})	Estimated value
P_a	(Pa)	Atmospheric pressure
P_i	(W m^{-2})	Model-predicted value
P_{tot}	(mm)	Total precipitation
R	(mm)	Runoff
R^2	Unitless	Coefficient of determination
RH	(%)	Relative humidity
$R_{L\uparrow}$	(W m^{-2})	Up-welling longwave radiation
$R_{L\downarrow}$	(W m^{-2})	Down-welling longwave radiation
$RMSD$	(W m^{-2})	Root mean square deviation
$RMSD_N$	(%)	Normalized root mean square deviation
$RMSD_S$	(W m^{-2})	Systematic root mean square deviation
$RMSD_U$	(W m^{-2})	Non-systematic root mean square deviation

R_N	(W m^{-2})	Net radiation
R_{Nc}	(W m^{-2})	Net radiation to canopy
R_{Ns}	(W m^{-2})	Net radiation to soil
RRMSD	(%)	Relative root mean square deviation
$R_{S\uparrow}$	(W m^{-2})	Up-welling shortwave radiation
$R_{S\downarrow}$	(W m^{-2})	Down-welling shortwave radiation
S	(%)	Sensitivity of the fluxes
SAVI	Unitless	Soil adjusted vegetation index
T_0	(°C)	Aerodynamic temperature
T_A	(°C)	Air temperature near the canopy
T_{Amax}	(°C)	Maximum air temperature near the canopy
T_D	(°C)	Dew-point temperature
T_i	(°C)	Daytime/night-time temperature
T_{max}	(°C)	Maximum air temperature
T_{min}	(°C)	Minimum air temperature
T_{opt}	(°C)	Optimum plant growth temperature
T_{SD}	(°C)	Dew-point temperature at the source/sink height
T_{su}	(°C)	The surface temperature of water
$\overline{V}$	(W m^{-2})	Mean of the variable (either the mean of observed values $\overline{O}$ or the mean of model-predicted values $\overline{P}$)
V_i	(W m^{-2})	Variable (either observed value O_i or model-predicted value P_i)
V_s	(mm)	SEB flux for the seasons

b_1	Unitless	Constant in PT-JPL
b_2	Unitless	Constant in PT-JPL
c	Unitless	Intercept of linear regression
c_p	(MJ kg^{-1} K^{-1})	The specific heat of dry air
cV_θ	Unitless	Coefficient of variation for soil moisture
d	(m)	Zero-plane displacement height
e	(hPa)	Vapor pressure
e_0	(hPa)	Atmospheric vapor pressure at the source/sink height
e_0^*	(hPa)	Saturation vapor pressure at the source/sink height
e_A	(hPa)	Atmospheric vapor pressure at the level of T_A measurements
e_A^*	(hPa)	Saturation vapor pressure at the level of T_A measurements
e_S^*	(hPa)	Saturation vapor pressure at the surface
f_{APAR}	Unitless	Fraction of PAR absorbed by total vegetation cover
f_c	Unitless	Fractional total vegetation cover
f_g	Unitless	Green canopy fraction
f_{IPAR}	Unitless	Fraction of PAR intercepted by total vegetation cover
f_M	Unitless	Plant moisture constraint
f_{SM}	Unitless	Soil moisture constraint
f_T	Unitless	Plant temperature constraint
f_{wet}	Unitless	Relative surface wetness (PT-JPL) or water cover fraction (MOD16)
g_A	(m s^{-1})	Aerodynamic conductance

g_C	(m s^{-1})	Canopy conductance
g_{Cmax}	(m s^{-1})	Maximum canopy conductance
g_{cu}	(m s^{-1})	Cuticular conductance per unit *LAI*
gl_{bl}	(m s^{-1})	Leaf-scale boundary layer conductance
gl_{eww}	(m s^{-1})	Leaf conductance to evaporated water vapor unit *LAI*
i	Unitless	Variable value at daytime and night-time
k_{NR}	Unitless	Constant in PT-JPL
k_{PAR}	Unitless	Constant in PT-JPL
m	Unitless	Slope of linear regression
m_1	Unitless	Constant in PT-JPL
m_2	Unitless	Constant in PT-JPL
$m(D_A)$	Unitless	Multiplier which reduces the potential stomatal conductance in case of high D_A
$m(T_{min})$	Unitless	Multiplier which limits potential conductance by minimum air temperatures
n	Unitless	Number of observations
r	Unitless	Correlation coefficient
r_a	(s m^{-1})	Aerodynamic resistance
r_{as}	(s m^{-1})	Aerodynamic resistance at soil surface
rbl_{max}	(s m^{-1})	Variable in MOD16
rbl_{min}	(s m^{-1})	Variable in MOD16
r_{corr}	(s m^{-1})	Corrected resistance
r_h	(s m^{-1})	Convective heat transfer

r_{hc}	(s m^{-1})	Wet canopy resistance to H
r_{hrc}	(s m^{-1})	Aerodynamic resistance (wet conditions)
r_{hs}	(s m^{-1})	Boundary layer resistance
r_{NIR}	Unitless	Surface reflectance, near-infrared
r_r	(s m^{-1})	Radiative heat transfer
r_{rc}	(s m^{-1})	Resistance to radiative heat transfer through air
r_{rs}	(s m^{-1})	Radiative heat transfer (soil)
r_{si}	(s m^{-1})	Dry canopy surface resistance to transpiration
r_{tot}	(s m^{-1})	Total aerodynamic resistance
r_{totc}	(s m^{-1})	Total aerodynamic resistance to vapor transport constant
r_{vc}	(s m^{-1})	Wet canopy resistance
r_{VIS}	Unitless	Surface reflectance, visible
s	(hPa K^{-1})	Slope of saturation vapor pressure versus temperature curve (estimated at T_A)
s_0	(hPa K^{-1})	Slope of the saturation vapor pressure and temperature between (T_0–T_A) versus (e_0^*–e_A^*) (approximated as s)
s_1	(hPa K^{-1})	Slope of the saturation vapor pressure and temperature between (T_{SD}–T_D) versus (e_0–e_A) (approximated at T_D)
s_2	(hPa K^{-1})	Slope of the saturation vapor pressure and temperature between (T_R–T_D) versus (e_s^*–e_A)
s_3	(hPa K^{-1})	Slope of the saturation vapor pressure and temperature between (T_R–T_{SD}) versus (e_s^*–e_S) (approximated at T_R)
s_4	(hPa K^{-1})	Slope of the saturation vapor pressure and temperature between (T_A–T_D) versus (e_0–e_A)
u	(m s^{-1})	Wind speed
$u*$	(m s^{-1})	Friction velocity
x	(W m^{-2})	Intependent variable

y	(W m^{-2})	Dependent variable
z_0	(m)	Roughness length
α	Unitless	Priestley-Taylor parameter
β	(kPa)	Constant in PT-JPL or MOD16 or the linear least squares fit (sensitivity analysis, unitless) or Bowen ratio (unitless)
γ	(hPa K^{-1})	Psycrometric constant
σ	(J k^{-4} m^{-2} s^{-1})	Stefan-Boltzmann constant
σ^2_i	Squared unit of the variable	Variance (i represents the variable)
ΔS	(mm)	Change in the water storage
$\Delta\sigma^2_{\lambda E}$	(W^2 m^{-4})	Residual variance for λE (between predicted and observed λE)
$\Delta\sigma^2_H$	(W^2 m^{-4})	Residual variance for H (between predicted and observed H)
$\Delta\lambda E$	(W m^{-2})	Residual error for λE (between predicted and observed λE) or Bowen ratio correction variable for λE
ΔH	(W m^{-2})	Residual error for H (between predicted and observed H) or Bowen ratio correction variable for H
ε	Unitless	Thermal infrared surface emissivity
θ	(m^3 m^{-3})	Soil moisture
κ	Unitless	Ratio between (e^*_0–eA) and (e^*_s–eA)
Λ	Unitless	Evaporative fraction
λ	(J kg^{-1})	Latent heat of evaporation
λE	(W m^{-2})	Evapotranspiration
λE_c	(W m^{-2})	Canopy transpiration
λE_{eq}	(W m^{-2})	Equilibrium latent heat flux
λE_i	(W m^{-2})	Interception evaporation

λE_{imp}	(W m^{-2})	Imposed latent heat flux
λE_{POT}	(W m^{-2})	Potential latent heat flux
λE_{pot_trans}	(W m^{-2})	Potential plant transpiration
λE_{s}	(W m^{-2})	Soil evaporation
λE_{SOIL}	(W m^{-2})	Actual soil evaporation
λE_{SOIL_POT}	(W m^{-2})	Potential soil evaporation
λE_{trans}	(W m^{-2})	Plant transpiration
λE_{wet_c}	(W m^{-2})	Wet canopy surface evaporation
λE_{wet_SOIL}	(W m^{-2})	Evaporation from wet soil surface
ρ	(kg m^{-3})	Density of air
ϕ	(W m^{-2})	Net available energy
Ω	Unitless	Decoupling coefficient, omega

Abbreviations

AA	Advection-aridity
ASTER	Advanced Spaceborne Thermal Emission and Reflection Radiometer
CF	Compact flash
EC	Eddy covariance
ET	Evapotranspiration
GED	Global Emissivity Database
IRGA	Infra-red gas analyser
L1…L6	Data quality level 1 to 6
LP DAAC	Land Processes Distributed Active Archive Center
MODIS	MODerate resolution Imaging Spectroradiometer
MOD16	MODIS global terrestrial evapotranspiration
NASA	National Aeronautics and Space Administration
NATT	North Australian tropical transect
PAR	Photosynthetically active radiation
PM	Penman-Monteith
PT	Priestley-Taylor
PT-JPL	Priestley-Taylor method by Jet Propulsion Laboratory
SEB	Surface energy balance
SEBS	Surface Energy Balance System
SSEBop	Operational Simplified Surface Energy Balance
SSR	Surface spectral reflectance
STIC1.2	Surface Temperature Initiated Closure model version 1.2
SW	Shuttleworth-Wallace
TIR	Thermal infrared
VI	Vegetation indices

List of figures

List of tables

1 Introduction

Evapotranspiration (ET) is an aggregated process, which combines direct evaporation from canopy and litter, the soil and water surfaces as well as plant transpiration (Guerschman et al., 2009). ET is one of the main elements of the terrestrial water balance after precipitation (P) (Leuning et al., 2008), and it has an essential role interconnecting the energy, water and carbon cycles (Vinukollu et al., 2011). Evaporation can also be seen as an energy flow from the surface as the vapor is transporting energy as a latent heat flux (λE) connecting ET to surface energy balance (SEB), and therefore to sensible heat flux (H). However, understanding and quantifying both energy and water cycles are important for instance for efficient use and management of water resources (e.g. Guerschman et al., 2009; Ma et al., 2012), especially under climate change (Lauenroth and Bradford, 2006). Accurate estimates of λE and H are particularly crucial in arid and semi-arid regions, where water availability is one of the key controls on ecosystem processes (Lauenroth and Bradford, 2006).

Australia is generally a dry continent, where water resources are being used for many competing purposes (Guerschman et al., 2009). A large seasonality and annual variability in precipitation are the main characteristics of the continent mainly due to El Niño Southern Oscillation, Southern Annular Mode and Indian Ocean Dipole (Risbey et al., 2009; Glenn et al., 2011). In most areas over the continent, potential evapotranspiration (E_p) is exceeding precipitation, and approximately 90% of precipitation evaporates back to the atmosphere as actual evapotranspiration (Glenn et al., 2011) with the residue generating soil, surface and groundwater resources (Guerschman et al., 2009). Moreover, the major part of climate is either desert (i.e. arid) (38%) or grassland (i.e. semi-arid) (36%) (Beringer et al., 2016), and average canopy cover is less than 50% (Glenn et al., 2011). In contrast, there are locations where annual average precipitation exceeds 4000 mm (Glenn et al., 2011).

Although the importance of understanding the key processes in the water budget of semi-arid regions is recognized, the information is still limited (Lauenroth and Bradford, 2006). Even though local measurements, such as eddy covariance (EC) systems and sap flux sensors, have been used to examine canopy-scale processes in Australia (Glenn et al., 2011), they are not suitable for large-scale monitoring of land surface fluxes (Ershadi et al., 2014) due to high cost, complexity and siting requirements. In addition, there are very few studies related to the estimation of water fluxes especially in semi-arid regions due to a large spatial heterogeneity of the vegetation and relatively small fluxes, which are difficult to measure (Meyer et al., 2015).

However, there is an urgent need to be able to estimate evapotranspiration patterns across a large scale of different ecosystems, as opposed to point and local measurements of λE (Glenn et al., 2011). The most feasible method to cost-effectively obtain surface fluxes over regional and continental scales with high spatial and temporal frequencies is to use remote sensing (e.g. Anderson et al., 2008; Ershadi et al., 2014; Sommer et al., 2016). Various approaches have been developed to estimate λE and H by remote sensing, and they can roughly be classified into (i) surface energy balance models using land surface temperature (T_R), (ii) methods based on vegetation indices (VI), and (iii) hybrid methods combining data of both surface temperature and VI (Yebra et al., 2013). One of the SEB approaches is to use thermal infrared (TIR) imagery from satellite or aircraft to measure T_R to constrain estimates of surface fluxes as the T_R variable is sensitive to moisture conditions and also to evaporative cooling (Anderson et al., 2012). However, some of these methods require a large amount of

data to define site-specific characteristics and parameters (e.g. Anderson et al., 2008), which can be difficult to obtain by the reason of data limitations and the lack of accurate measurements (Glenn et al., 2011).

Combining the Penman-Monteith (PM) equation with measurements of T_R has also been proven to be successful (Moran et al., 1996), and it was initially introduced by Jackson et al. (1981) in the formulation of crop water stress index. Likewise, the Shuttleworth-Wallace (SW) model (Shuttleworth and Wallace, 1985) is another preeminent physical model for SEB flux estimation. The PM equation treats the vegetation canopy as a "big-leaf" (Monteith 1965) and it combines aerodynamic and energy bases to estimate evaporation (Dhungel et al., 2014). Although the PM equation has widely been used to estimate terrestrial λE (Leuning et al., 2008), it requires parameters (aerodynamic and canopy conductances, g_A and g_C, respectively) which are vegetation specific and difficult to measure directly (Wang and Dickinson, 2012). The parametrization of these conductances is the major source of uncertainty (Vinukollu et al., 2011) especially in sparsely vegetated and water stressed areas, thus leading to high errors in latent heat flux estimations (e.g. Leuning et al., 2008; Morillas et al., 2013; Dhungel et al., 2014).

Given the need to overcome the above mentioned limitations for reliable estimates of surface fluxes at large-scale and across a wide range of different ecohydrological areas, this study uses a physically-based single-source SEB model, the Surface Temperature Initiated Closure (STIC1.2) (Mallick et al., 2014, 2015, 2016), to estimate surface energy balance fluxes in Australia. The STIC framework integrates radiometric surface temperature (T_R) measured by TIR remote sensing into the combined PM-SW equation to analytically retrieve solutions for surface and atmospheric conductances and surface energy balance fluxes. Therefore, there is no need for any land surface parametrization.

The first objective of this study is to link T_R and STIC1.2 model to predict SEB flux components (λE and H) over a wide range of ecohydrologically divergent ecosystems in Australia, and compare the predicted fluxes to EC observations from Australian OzFlux network. The second objective is to identify the role of ecohydrology in determining the errors and variability of the estimated latent and sensible heat flux components. The third objective is to compare the STIC1.2 model with other SEB models: the Priestley-Taylor method by Jet Propulsion Laboratory (PT-JPL by Fisher et al., 2008) and MODIS global terrestrial evapotranspiration model (MOD16 by Mu et al., 2011) by using MODerate resolution Imaging Spectroradiometer (MODIS) satellite data. The partitioning of λE into surface evaporation and transpiration by STIC1.2 has been previously evaluated in Amazon by Mallick et al. (2016). However, this study will particularly focus on the evaluation of the total λE and H fluxes across aridity gradient in the Australian ecosystems at 15 different OzFlux sites. Therefore, the partitioning of λE is left outside of the study scope. The selected study years were 2013 and 2014, and the selection was based on the OzFlux data availability.

2 Background

2.1 Links between hydrological cycle, evaporation and energy balance

The main concept of the hydrological cycle is based on the movement of water. A water budget for a specific area, for example land or water body, states that the income (i.e. precipitation) to the area will form runoff (i.e. surface runoff, subsurface runoff and groundwater flow after infiltration), percolate, transpire from plants, evaporate from soil or directly from water surface or form water storages (i.e. groundwater). The hydrological cycle can be very short (precipitated water is evaporating quickly back to the atmosphere) or very slow (water movement within the groundwater flow). (Lundin, 2000.) At annual scale, approximately 62% of the continental precipitation is being either evaporated or transpired (Vinukollu et al., 2011). The hydrological cycle is illustrated in Figure 1, and general water balance equation for a specific area is shown in Equation 1.

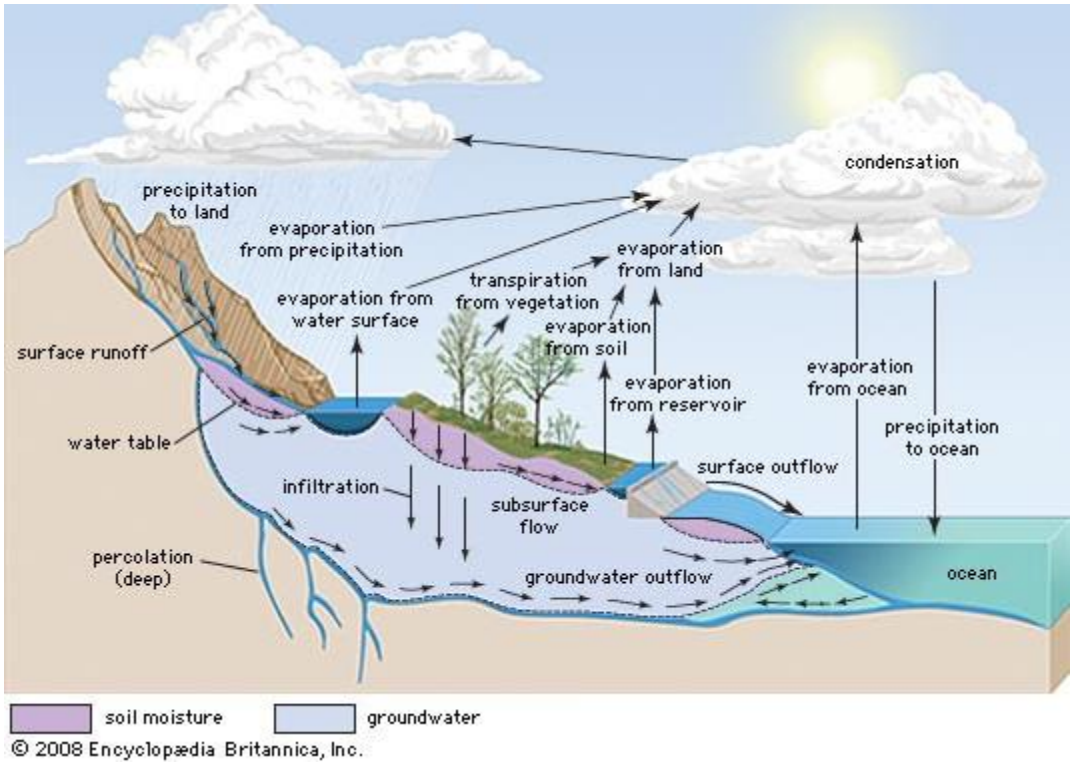

Figure 1 The illustration of hydrological cycle. Modified from Encyclopædia Britannica (2008).

$$P = E + R + \Delta S \tag{1}$$

where P is precipitation (mm/a), E evaporation (mm/a), R runoff (mm/a) and ΔS the change in the storage (mm/a).

Unlike the other main terms in the water budget, evaporation is challenging to measure directly (e.g. Liou and Kar, 2014). Evaporation can be defined as a water vapor flow from both sea and land to the atmosphere as a net flux of water molecules moving between vapor and liquid phases of water (Figure 2). The flow rate depends on the difference between vapor pressure in the evaporating surface and the atmospheric vapor. In case of wet surface, the rate of evaporation is increasing when surface temperature is increasing and air humidity

near the surface is decreasing. However, evaporation process requires energy for changing the phase of liquid water into vapor. (Lundin, 2000.) This is called a latent heat of vaporisation, and the process is cooling the evaporating surface. For example, one gram of water needs 2454 joules to change its phase into vapor at 20 °C (Bonan, 2002). The required energy can be originated directly from sun by solar radiation, but also indirectly from the heat storages (i.e. soil, water or vegetation), which are heated by the sun. Also warm air can provide a heat flow to increase evaporation. In case of high evaporation rate from the very dry surface, the surface warmer than the air is generating a heat flow (sensible heat flux, *H*) to the air. Therefore, a part of the available energy is going to the sensible heat flux instead of latent heat flux. (Lundin, 2000.)

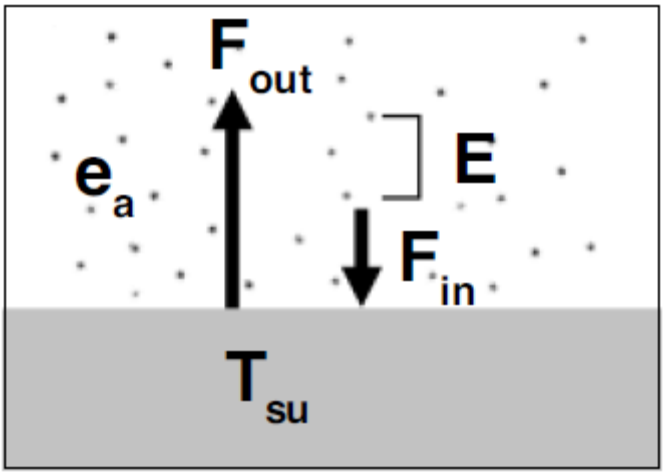

Figure 2 The illustration of evaporation (*E*), which is a net flow of water molecules between the evaporating surface (here liquid) and the vapor in the air. F_{out} is the outflow from the surface, and proportional to the saturation vapor pressure at the surface, $e_{sat}(T_{su})$, where T_{su} is the suface temperature of water. F_{in} is the inflow proportional to the vapor pressure of the air (e_A). Thus, E (= F_{out}–F_{in}) is proportional to the vapor pressure deficit $e_{sat}(T_{su})$–e_A. (Lundin, 2000.)

In addition to available energy ($\phi = R_N – G$, where R_N is the net radiation and G the ground heat flux), the other factors affecting the evaporation rate are air humidity, an efficient transport mechanism for the vapor from the air near the evaporating surface and wind conditions. The air humidity is depending on the surrounding air mass and its origin. The vapor transport is also due to wind, which is generating turbulence. (Lundin, 2000.) The air motion consisting of irregular swirls, eddies, is creating a vertical transport of vapor and heat in the direction of lower vapor pressure (Wang and Dickinson, 2012). For example, the rate of evaporation is increasing in case of drier air and stronger wind. Also the local climate can affect evaporation: for instance large open water bodies are increasing the air humidity, and therefore reducing evaporation near the water bodies. Water availability is also one main factor in terms of the evaporation rate: water can evaporate directly from soil water or wetlands, lakes and open water surfaces, but usually from land areas through vegetation. This is called transpiration, whose rate is depending especially on the vegetation type and the degree of the total leaf area per unit ground area, the leaf area index (*LAI*). Evaporation can also occur from snow, but since the temperature of snow is not higher than 0°C, the vapor pressure difference becomes limited and evaporation rate stays small. (Lundin, 2000.)

Evapotranspiration (ET) is a combination of evaporation from water surfaces and soil water as well as transpiration. Water is mainly transpiring through the stomata, which can be defined as microscopic openings of the leaves. Stomata is being opened for CO_2 uptake for

photosynthesis and biomass building. At the same time, vegetation has to supply water to the atmosphere due to the vapor pressure difference. Therefore, vegetation has to uptake water from the soil. In case of dry soil, the vegetation will wilt due to insufficient water uptake. Although transpiration is a response to the atmospheric demand for water, the plants are able to regulate the transpiration rate by controlling the closing and opening of the stomata. (Lundin, 2000.) Sometimes water can also evaporate directly from the leaves of the plant, which is called interception. Interception is approximately 10–20% of annual precipitation. (Bonan, 2002.) Evaporation from a surface with optimal water supply is called the potential evaporation (E_p), and it represents the ability of the atmosphere to generate evaporation (Lundin, 2000).

As previously mentioned, the hydrological cycle is also linked with radiation from the sun, which is one of the main driving forces of the cycle in addition to the slope of terrain (gravitation). Net radiation is the main driver of latent and sensible heat fluxes, whereas the slope is determining the route for the surface water and groundwater flow. As discussed earlier, evaporation can be seen as an energy flow from the surface as the vapor is transporting energy as a latent heat flux. (Lundin, 2000.) The energy budget for a surface can generally be expressed as follows:

$$R_N = H + \lambda E + G \tag{2}$$

where R_N is the net radiation (net supply to the surface by solar radiation) (W m^{-2}), H is the sensible heat flux (W m^{-2}), which is occurring due to temperature difference between the surface and the air, λE is the latent heat flux (W m^{-2}), where E is the evaporation rate and λ the latent heat of vaporisation, and G is the ground heat flux (W m^{-2}) presenting the heat conduction from the ground. (Liou and Kar, 2014.) Equation 2 should also include the energy required for photosynthesis in case of vegetation. However, it is usually neglected, because it is relatively small compared to other terms in the energy balance. (Lundin, 2000.) The equation for R_N is expressed as follows:

$$R_N = R_{S\downarrow} - R_{S\uparrow} + R_{L\downarrow} - R_{L\uparrow} \tag{3}$$

where $R_{S\downarrow}$ is the down-welling shortwave radiation, $R_{S\uparrow}$ is the up-welling shortwave radiation, $R_{L\downarrow}$ is the down-welling longwave radiation and $R_{L\uparrow}$ is the up-welling longwave radiation (all in W m^{-2}) (Kalma et al., 2008).

The partitioning into sensible and latent heat fluxes is depending on surface temperature, air temperature, the humidity of air as well as water availability. In case of wet surface conditions, the latent heat flux is exceeding the sensible heat flux. For instance, the latent heat flux can be 1 or 2 times higher than the sensible heat flux for the wet green grass. The opposite is true for dry conditions, when the sensible heat flux is dominating. (Lundin, 2000.)

2.2 Modelling of evapotranspiration

2.2.1 The development of evapotranspiration modelling

The concept of evaporation arises from 500 B.C., but the most crucial factors has been identified within the last 200 years. For example, the relationship between vapor pressure deficit ($D_A = e_{sat} – e_A$ in Figure 2) of the near surface air and the rate of evaporation was first recognised in 1802 by Dalton. This was followed by the development of a wide range of

empirical relationships using other environmental variables. (Vinukollu et al., 2011.) Penman (1948) developed the well-known Penman equation from energy considerations and turbulent flux theory to model evaporation for surfaces which are not restricted by the availability of water. Monteith (1965) improved it by introducing biophysical considerations, and therefore the Penman–Monteith (PM) combination equation took also into account the vegetation control on transpiration rates. Ultimately, Priestley and Taylor (PT) (1972) gave a simplified version of this equation for moist surfaces by integrating a unitless constant α (originally set to 1.26) into the Penman equation. Later, it was shown that the value for α is decreasing from its original value when the surface is under a water stress (Vinukollu et al., 2011). The Shuttleworth-Wallace (SW) model is an extension of the PM equation, and it is estimating total evapotranspiration as a sum of both transpiration and soil evaporation (dual source) (Shuttleworth and Wallace, 1985).

Historically, the first field estimates of ET for agricultural purposes were based on pan evaporation or lysimeters. These methods were followed by a development of eddy covariance (EC) technique, when the instrumentation for scalar flux and vertical wind measurements became available in the 1970s. (Vinukollu et al., 2011.) Local transpiration can also be measured for instance by sap flow techniques, and total ET by scintillometers or water balance techniques at site or catchment scale (Glenn et al., 2011). These methods are estimating ET with a very good temporal resolution, but they require maintenance, and are spatially limited, time consuming, expensive and vulnerable to instrumentation failure (e.g. Guerschman et al., 2009; Liou and Kar, 2014).

One way forward from field observations is to use satellite remote sensing techniques for evaporation estimations. Satellite data have been available since the late 1970s., and currently, there are several methods for estimating ET from remotely sensed data. (e.g. Kalma et al., 2008; Guerschman et al., 2009). Nowadays, it is widely recognised that reliable estimates of ET are crucial for applications in hydrology, agriculture, forestry, water management and also climate research (e.g Vinukollu et al., 2011). However, obtaining accurate global estimates of ET without field calibrations remains a challenge (García et al., 2008). Field measurements are especially needed for calibration of methods which rely on satellite data (Liou and Kar, 2014).

2.2.2 Eddy covariance method

Eddy covariance technique is one of the most reliable field estimation methods of ET for the areas of hundreds to thousands of square meters. By using EC method, sensible and latent heat fluxes can be measured directly within and above the canopy. (Glenn et al., 2011.) The general instrumentation consists of three-dimensional wind sensor to measure the orthogonal wind components and the speed of sound in addition to an infrared gas analyser for estimating the density of water vapor and CO_2 concentration. The general principle of EC technique is to measure the characteristics of each eddy parcel from air flow and the speed of the vertical air movement. The characteristics include gas concentration, air temperature and humidity. With this information, it is possible to calculate the vertical upward or downward fluxes of gas concentration, temperature and humidity as it is possible to measure how many molecules are moving and how fast they went up or down over a time period. Thus, the mathematical representation of the method is a covariance between the vertical velocity measurements, the upward and downward movement of the parcels and the concentration of the flux of interest. (Burba, 2013.)

The EC technique is complex, and currently there are several differen calculation processes for this method (Wang and Dickinson, 2012). EC measurements include uncertainty and errors ranging between 5–30% (Glenn et al, 2011; Wang and Dickinson, 2012). The uncertainty is related to the energy closure error arising from the surface energy balance equation (Equation 2). The energy balance closure can be expresses as $R_N–G = \lambda E + H$. Generally, λE and H are argued to underestimate $R_N–G$ by 10-30% (e.g. Glenn et al., 2011). This closure error can be due to instrumental limitation in case of high moisture fluxes, the scaling mismatches of the measurements of different energy balance components or the secondary large eddies, which are hard to capture by EC towers (Figure 3). These large-scale eddies might occur when the landscape is heterogeneous. Measuring ET by EC towers is also challenging during rainfall. (Glenn et al., 2011.)

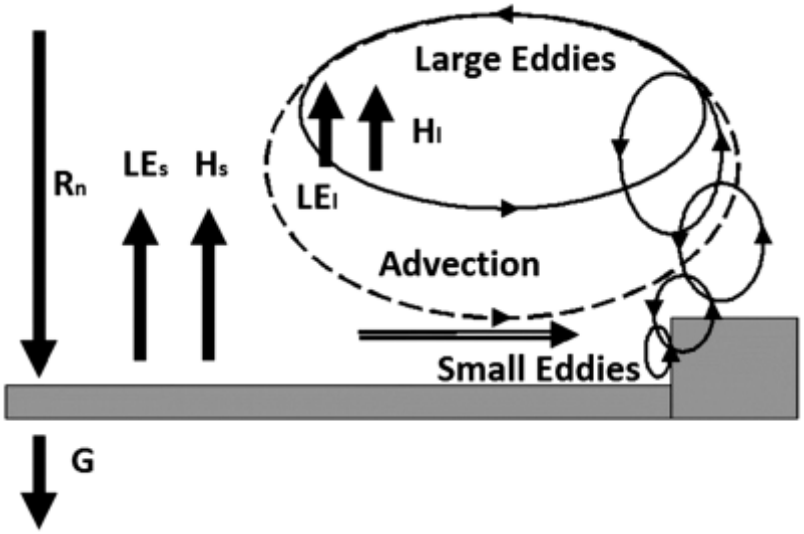

Figure 3 The diagram of eddies produced by landscape features. The large-scale eddies are not measurable by EC flux tower instruments, which is one factor to prevent obtaining the energy balance closure. R_N is the net radiation, G is the ground heat flux, λEs and Hs are the latent and sensible heat fluxes (measured), respectively, produced by small-scale eddies, and λEi and Hi the latent and sensible heat fluxes (not measured) from large-scale eddies. (Glenn et al., 2011.)

2.2.3 Thermal infrared method

Thermal infrared methods (TIR) using remote sensing have widely been developed since 1980s (Kalma et al., 2008). Nowadays, there are many available TIR applications, such as Surface Energy Balance Algorithm for Land, two-source energy balance and Atmosphere-Land Exchange Inverse. A single or blended source thermal gradient-resistance model is treating the land-surface as a homogenous flux and radiometric emission source and a dual source method as a contribution of both the soil and canopy components. (Anderson et al., 2012.) One of the main inputs of the model is land surface temperature, T_R, which can be measured by satellite sensors (e.g. Landsat, MODIS and ASTER). Some of the methods are also based on the use of vegetation indices (e.g. normalized difference vegetation, *NDVI*) in addition to T_R. (Kalma et al., 2008.)

Generally, the gradient-resistance model is estimating evapotranspiration by using the energy balance equation and portioning the available energy ($R_N–G$) into sensible and latent heat fluxes (Anderson et al., 2012) (see Equation 2). In a basic TIR approach, sensible heat flux is computed using the aerodynamic temperature (T_0, °C) and air temperature near the canopy (T_A, °C) as follows:

$$H = \rho c_P \frac{T_0 - T_A}{r_A} \quad (4)$$

where ρ is the air density (kg m^{-3}), c_P the specific heat of dry air (MJ kg^{-1} K^{-1}), and r_A the aerodynamic resistance (s m^{-1}), which depends on the wind speed, surface roughness and stability in the near atmospheric surface layer. If the quantity for available energy is known, the latent heat flux can be calculated as a residual of Equation 2. (Anderson et al., 2012.)

However, there are some limitations in the computation of H when using Equation 4. First, the aerodynamic temperature cannot be measured directly as it is a theoretical variable. It is related to T_R, but these variables are not equal. The relationship between these two variables depends on, for instance, the viewing angle of the TIR sensor, the vegetation cover fraction and the surface roughness length of heat and momentum. In addition, the inaccuracy of T_R estimations arising from inappropriate calibration and also improper correction of emissivity as well as inaccurate T_A measurements affect the results. These issues have been hindering the use of TIR methods for ET estimations. More recently, the TIR method has been recognized as a viable option when these discrepancies in T_R and T_A estimations are acknowledged and land-atmosphere interactions as well as radiometric emissivity from a heterogeneous land surface are properly expressed. (Anderson et al., 2012.)

3 Data

3.1 OzFlux

3.1.1 Introduction to OzFlux

OzFlux is a national research network of eddy covariance flux tower sites in Australia and New Zealand, which provides continental-scale observations of energy, carbon and water cycles (OzFlux, 2016a). OzFlux is part of continuously operated international FLUXNET network of currently over 650 micrometeorological flux tower sites operating within USA (AmeriFlux), Asia (AsiaFlux), China (ChinaFlux) and Canada (Fluxnet Canada) in addition to Australia (Beringer et al., 2016). The main objectives of the OzFlux network are to monitor and assess trends and extend the understanding of terrestrial biosphere and climate in Australia (Beringer et al., 2016). Observations are also valuable for parameterizing and validating models and they support validation of estimations obtained via remotely sensed data (OzFlux, 2016a).

The long-term EC measurements in Australia started in 2000 when the first EC site Tumbarumba (AU-Tum) was established (Beringer et al., 2016). Currently, there are 26 active OzFlux sites, which are located over a wide range of ecohydrologically divergent landscapes (OzFlux, 2016b). Most of the OzFlux sites were originally established for specific purposes under short term research grants. Recognising the importance of continuous measurements, the sites have been operated on a long-term basis. In general, site operators have responsibility for operating the sites, processing the data and controlling the quality of the data. (Beringer et al., 2016.)

3.1.2 Selected OzFlux sites

In this study, the level-3 quality controlled (see Section 3.1.3 for data processing) surface flux and meteorological data is used for the years 2013 and 2014 from 15 OzFlux sites located across nine different ecoregions in Australia: deserts and xeric shrublands (Alice Springs Mulga AU-ASM, Ti Tree East AU-TTE), pasture (Riggs Creek AU-Rig), Mediterranean woodlands (Calperum AU-Cpr, Gingin AU-Gin, Great Western Woodlands AU-GWW), temperate broadleaf (and mixed) forest (Tumbarumba AU-Tum, Wombat AU-Wom), temperate grassland (Yanco AU-Ync), temperate woodlands (Cumberland Plains AU-Cum, Whroo AU-Whr), tropical and subtropical moist broadleaf forest (Cow Bay AU-Cow), tropical grassland (Sturt plains AU-Stp) and tropical savannas (Howard Springs AU-How, Dry River AU-Dry) (OzFlux, 2016b). In general, the mean annual precipitation in Australia is ranging between 134 and 2804 mm and mean annual temperature between 3.8–29 °C (Beringer et al., 2016). We divided selected sites into three different ecohydrological classes based on annual precipitation: dry (P < 350 mm: AU-ASM, AU-Cpr, AU-GWW and AU-TTE), semi-dry (350 < P < 700 mm: AU-Gin, AU-Rig, AU-Stp, AU-Whr, AU-Wom and AU-Ync), and wet (P > 700 mm: AU-Cow, AU-Cum, AU-Dry, AU-How and AU-Tum), respectively. The characteristics of each site are represented in Tables A1 and A2 (Appendix).

The selected 15 study sites are located under 8 different Köppen climates (Figure 4): Hot semi-arid steppe (BSh: AU-ASM, AU-GWW, AU-Stp), cold semi-arid steppe (BSk: AU-Cpr: AU-Ync), hot arid desert (BWh: AU-TTE), warm temperate climate with dry, hot summer (Csa: AU-Gin), warm temperate fully humid climate with hot summer (Cfa: AU-Cum), warm temperate fully humid climate with warm summer (Cfb: AU-Rig, AU-Whr,

AU-Wom, AU-Tum), tropical monsoon (Am: AU-Cow) and tropical savanna with dry winter (Aw: AU-Dry, AU-How) (FLUXNET, 2016).

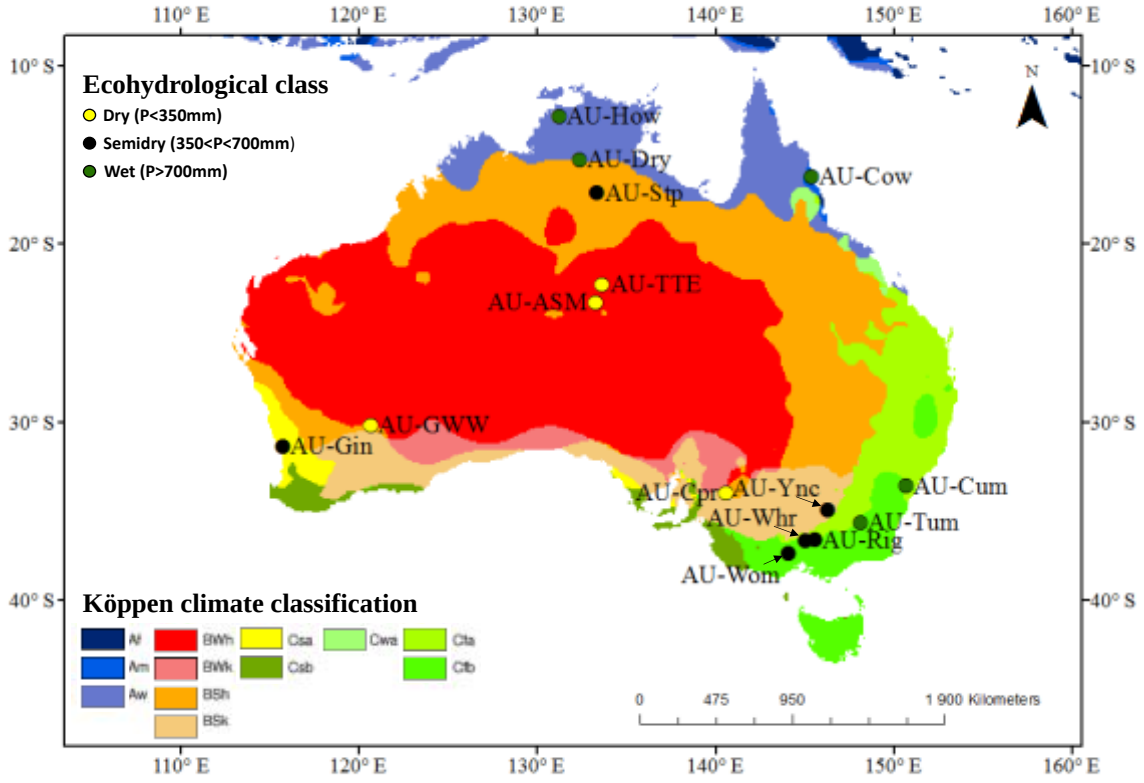

Figure 4 Map of Australia representing the location and climate classifications of OzFlux sites. Outside the Köppen climates of selected sites, Af represents tropical rainforest, BWk cold arid desert, Csb warm temperate climate with dry, warm summer and Cwa warm temperate climate with dry winter and hot summer (Peel et al., 2007).

3.1.3 Instrumentation of OzFlux sites

The instrumentation of OzFlux sites is nearly consistent. In general, the tower instrumentation consist of a CSAT3 sonic anemometer (Campbell Scientific, Logan, Utah, USA) (Beringer et al., 2016), which is measuring wind velocities and sonic temperature (OzFlux, 2016b). Atmospheric pressure and the densities of CO_2 and H_2O are measured either using a Li-7500[A] (Li-COR, Lincoln, Nebraska, USA) or EC-150/155 (Campbell Scientific, Logan, Utah, USA) open path infra-red gas analyser (IRGA) placed at the top of the tower. These measurements are recorded either at 10 or 20 Hz at all the sites. (Beringer et al., 2016.)

Complementary measurements include slow response wind speed (various, Gill Instruments Ltd, Lymington, Hampshire, UK; R.M. Young, Traverse City, Michigan, USA), air temperature and humidity (various, Vaisala, Helsinki, Finland) made at one height in minimum. Soil related measurements are in general made at several depths. These measurements include soil water content (various, Campbell Scientific, Logan, Utah, USA), soil temperature (various, TCAV, Campbell Scientific, Logan, Utah, USA) and ground heat flux (CN3, Middleton, Newtown, Austalia; HFT3, Campbell Scientific, Logan, Utah, USA; HFP01, Hukseflux, Delft, The Netherlands). Radiation fluxes (CNR1 and CNR4, Kipp & Zonen; NR01, Hukseflux; Delft, The Netherlands) are measured at the top of the tower and precipitation (CS702, Campbell Scientific, Logan, Utah, USA; CS7000, Hydrological

Services, Warwick Farm, NSW, Australia) in general at the ground level. (Beringer et al., 2016.)

Systems measuring also the profiles of H_2O and CO_2 concentration within the canopy are installed at three sites, AU-Tum, AU-Wom and AU-Whr, which are included in this study. At most sites, the data are recorded using Campbell data loggers (various, Campbell Scientific, Logan, Utah, USA). The recorded data are retrieved through either modem or compact flash (CF) cards, and archived by the site operator's institute. (Beringer et al., 2016.) More details of instrumentation at the specific OzFlux sites can be found from the website of OzFlux (http://www.ozflux.org.au/monitoringsites/index.html).

3.1.4 Data processing of OzFlux

The logger data are recorded as average covariances (30 min frequency, 1h at AU-Tum) and processed further through six levels according to the standard OzFluxQC software processing scripts (Beringer et al., 2016). Turbulence data are processed into average flux values using available software packages such as EddyPro (Li-COR), which is followed by various data controlling steps. (Isaac et al., 2016.) These stages are as follows and illustrated in Figure 5:

- L1 (level 1): processing the flux tower data and writing the data as a netCDF file.
- L2 (level 2): quality controlling the L1 data.
- L3 (level 3): correcting the L2 data.
- L4 (level 4): gap filling the radiation, meteorological and soil data.
- L5 (level 5): gap filling the flux data.
- L6 (level 6): partitioning the gap filled net ecosystem exchange of carbon into gross primary production and ecosystem respiration.

In the end the stages generate a CF-compliant netCDF file (Isaac et al., 2016). The OzFlux data are public and available online at
http://data.ozflux.org.au/portal/pub/listPubCollections.jspx.

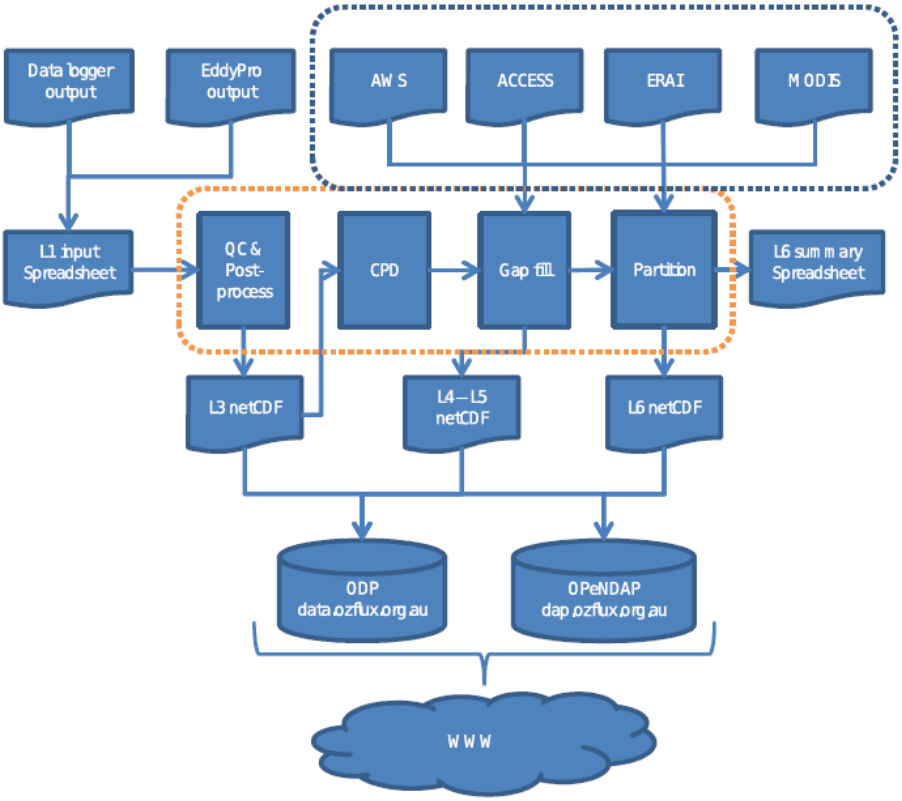

Figure 5 The diagram of the OzFlux data processing stages (Isaac et al., 2016).

In this study, the quality controlled L3-data are used. The level 1 data is first combined from the input data and metadata entered by the user into a single netCDF file. The input data can originate from two sources: Campbell data loggers or a software, which is designed to process the turbulence data, for example the earlier mentioned EddyPro. For data from the logger, the OzFluxQC checks the average covariance output values, applies coordinate rotation to the covariances and calculates the fluxes at L3. If the data comes from the software, the checks are conducted, but the other corrections and calculations are not performed at L3. (Isaac et al., 2016.)

The quality control and control checks by OzFluxQC include checking that values are within a plausible range, detecting possible spikes, checking the dependence between the variables and rejecting manually the sonic and IRGA values based on their diagnostic values or signal strength. By using dependency check, one variable can be rejected based on another variable. One example is the rejection of flux measurements if the wind direction is not within an acceptable range. These limits and ranges are set specifically to each month due to a large variability in different seasons in Australian ecosystems. L3-stage includes calculation of meteorological variables, standard corrections (e.g. two-dimensional coordinate rotation and sensor line-averaging) and calculation of SEB fluxes, for instance. Fluxes and meteorological quantities are then re-calculated based on the rotated and corrected covariances. Fluxes are further corrected and available energy calculated. (Isaac et al., 2016.) After the L3-stage, data can be gap filled as described in Isaac et al. (2016).

Instead of gap filling, missing sub-daily λE and H values (for data availability see Table A3 in Appendix) were not included in the computation in this study. Although the data is quality controlled, the Bowen ratio closure (Bowen, 1926) is used as described by Chávez et al.

(2005) and later on adopted by Anderson et al. (2008) and Mallick et al. (2014, 2015, 2016) to correct the observed fluxes (for calculation see Appendix 1).

3.2 MODIS Terra

3.2.1 Introduction to MODIS Terra

In addition to eddy covariance data provided by OzFlux, this study uses Moderate Resolution Imaging Spectroradiometer (MODIS) data provided by National Aeronautics and Space Administration (NASA). MODIS is one of the main instruments of satellites Terra (formerly known as EOS AM-1) and Aqua (formerly known as EOS PM-1). Terra is passing the Earth from the direction of north to south across the equator in the morning, whereas Aqua passes across the equator from the opposite direction, south to north, in the afternoon. Together these satellites provide data over the whole Earth's surface every 1 to 2 days using 36 spectral bands or groups of wavelengths ranging from visible to infrared light. (NASA, 2016a.) Terra was launched in December 1999 with the first MODIS flight instrument, ProtoFlight Model, and Aqua three years later in May 2002 with the second MODIS flight instrument, Flight Model 1 (NASA, 2016b). These instruments aim to offer data to a wide community of international users to improve the understanding of global processes occurring on the land, in the oceans and in the atmosphere. MODIS is also crucial for further development of Earth system models. (NASA, 2016a.) In this study, MODIS data acquired via Terra satellite is used.

Terra satellite is circling the Earth 16 times a day and crossing the equator approximately at 10:30 a.m. The satellite is located at an altitude of 705km from the Earth (NASA, 1999a). Terra includes five different on-board sensors, which are providing coincident measurements of the Earth system. (NASA, 2016c.) In addition to MODIS, these sensors are (NASA, 2016c)

- Advanced Spaceborne Thermal Emission and Reflection Radiometer (ASTER)
- Clouds and Earth's Radiant Energy System (CERES)
- Multi-angle Imaging Spectroradiometer (MISR)
- Measurements of Pollution in the Troposphere (MOPITT).

3.2.2 MODIS Terra data products

In this study, two different MODIS Terra products are used: MOD11A2 and MOD09A1. The selected study sites for MODIS analysis included sites within the north Australian tropical transect NATT (AU-ASM, AU-Dry, AU-How, AU-Stp) and AU-Tum. Both datasets were available for selected sites as 2.5 x 2.5 km^2 grid. MOD11A2 dataset provides the level-3 MODIS land surface temperature (T_R) and emissivity data, which is composed from MOD11A1 on daily 1-km T_R product and stored on a 1-km sinusoidal grid as the average clear-sky land surface temperatures over a period of 8-days. This product provides for instance daytime and night-time T_R values, quality assessment, observation times, view angles, the amount of clear-sky days and emissivities, which are estimated from land cover types. (Land Processes Distributed Active Archive Center LP DAAC, 2016a.)

MOD09A1 level-3 dataset provides estimates of the surface spectral reflectance (SSR) from the Bands 1–7 at 500 m resolution in the sinusoidal projection. The pixels contain the best L2G observation, which is made during an 8-day time interval. L2G means that the low-level data is being corrected for atmospheric gases and aerosols. Dataset includes quality assessment, the observation date in addition to reflectance values for Bands 1–7. (LP DAAC,

2016b.) All the SSR, T_R and emissivity products are validated over a set of locations (LP DAAC, 2016a, 2016b). These data are available at http://daacmodis.ornl.gov/cgi-bin/MODIS/GLBVIZ_1_Glb/modis_subset_order_global_col5.pl (ORNL DAAC, 2016).

4 Methods

4.1 Models

4.1.1 Surface Temperature Initiated Closure (STIC1.2)

In this study, we are using STIC (version STIC1.2) model, which is based on physical integration of T_R into a combined structure of the Penman-Monteith (PM) and Shuttleworth-Wallace (SW) models (PM-SW). The main objective is to obtain analytical solution for the aerodynamic and surface conductances, followed by simultaneous estimation of H and λE (Mallick et al., 2016). The primary assumption in STIC1.2 is that g_A and g_C are depending on the aerodynamic temperature (T_0) and soil moisture (θ) through T_R, which allows direct integration of T_R into the PM-SW system (Mallick et al., 2016). The external inputs in STIC1.2 are net radiation (R_N), ground heat flux (G), air temperature (T_A), relative humidity (RH) or vapor pressure (e_A) at the reference level (in this study from Ozflux data) in conjunction with T_R observations via satellites (in this study from MOD11A2). All the models are coded using Matlab R2014b program by MathWorks.

If direct T_R observations are not used, the STIC1.2 model requires outgoing longwave radiation ($R_{L\uparrow}$) and land cover based surface emissivity (ε) values as extra inputs for estimation of T_R based on Sun and Pinker (2003) (Equation 5). A unique value of emissivity was assigned for each site (see Table A3 in Appendix 2) based on ASTER Global Emissivity Database (GED) (Hulley et al., 2015). In this study, $R_{L\uparrow}$ (from OzFlux data) and ε values are used to validate the STIC1.2 model. Satellite data of T_R is used for STIC1.2 when comparing λE and H fluxes between different models.

$$T_R = \left(\frac{R_{L\uparrow}}{\sigma\varepsilon}\right)^{0.25} - 273.15 \tag{5}$$

where $R_{L\uparrow}$ is the outgoing longwave radiation (W m^{-2}), σ Stefan-Boltzmann constant (J K^{-4} m^{-2} s^{-1}) and ε emissivity (unitless).

The expressions of λE and H according to PM equation are as follows (Monteith, 1965):

$$\lambda E = \frac{s\phi + \rho c_P g_A D_A}{s + \gamma\left(1 + \frac{g_A}{g_C}\right)} \tag{6}$$

$$H = \frac{\gamma\phi\left(1 + \frac{g_A}{g_C}\right) - \rho c_P g_A D_A}{s + \gamma\left(1 + \frac{g_A}{g_C}\right)} \tag{7}$$

where E is the evaporation rate (kg m^{-2} s^{-1}), λ the latent heat of evaporation (J kg^{-1}), ρ the air density (kg m^{-3}), c_P the specific heat of dry air (MJ kg^{-1} K^{-1}), γ the psychrometric constant (hPa K^{-1}), s the slope of the saturation vapor pressure versus air temperature (hPa K^{-1}), D_A is the saturation deficit of the air (hPa) or vapor pressure deficit at the reference level and ϕ the

net available energy (W m^{-2}) ($\phi = \lambda E + H$). The units of conductances are expressed in m s^{-1}. For a full vegetation and (or) bare surface, g_C represents the canopy conductance and (or) bare surface conductance, respectively. In the case of partial canopy cover, g_C represents an aggregated surface conductance of both canopy and soil.

By integrating T_R with SEB theory, STIC is formulating four "state equations" that eliminate the need for exogenous parametric submodels for g_A, g_C, and associated aerodynamic variables. The state equations of STIC1.2 are as follows and their detailed derivations are described in Appendix 1 as well as in Mallick (2014, 2015, 2016).

$$g_A = \frac{\phi}{\rho c_P\left[(T_o - T_A) + \left(\frac{e_0 - e_A}{\gamma}\right)\right]} \tag{8}$$

$$g_C = g_A \frac{(e_0 - e_A)}{(e_0^* - e_0)} \tag{9}$$

$$T_o = T_A + \left(\frac{e_0 - e_A}{\gamma}\right)\left(\frac{1-\Lambda}{\Lambda}\right) \tag{10}$$

$$\Lambda = \frac{2\alpha s}{2s + 2\gamma + \gamma\frac{g_A}{g_C}(1+M)} \tag{11}$$

where T_0 is the temperature at the apparent source/sink height of momentum (i.e., sum of roughness length, z_0 and zero-plane displacement height d) (or in-canopy air stream) (°C), T_A is the air temperature (ºC), e_0 is the atmospheric vapor pressure at the source/sink height (hPa), e_A atmospheric vapor pressure at the level of T_A measurement (hPa), e_0^* is the saturation vapor pressure at the source/sink height (hPa), Λ is the evaporative fraction (the ratio of λE and ϕ), α is the Priestley-Taylor parameter (unitless) (Priestley and Taylor, 1972) and M is a unitless quantity which describes the relative wetness (or moisture availability) of the surface.

With the values of R_N, G, T_A and RH or e_A, these Equations 8–11 can be solved simultaneously to derive analytical solutions for the four state variables (g_A, g_C, T_0 and Λ). The state equations have four associated unknowns: e_0^*, e_0, M and α. As a result, there are 4 equations with 8 unknowns. Therefore, an iterative solution is needed to determine these four unknown variables. In this study, the unknowns are described as follows:

$$e_0^* = e_A + \left[\frac{\gamma\lambda E(g_A + g_C)}{\rho c_P g_A g_C}\right] \tag{12}$$

$$e_0 = e_0^* - D_0, \text{ where } D_0 = D_A + \left[\frac{\{s\phi - (s+\gamma)\lambda E\}}{\rho c_P g_A}\right] \tag{13–14}$$

$$M = \frac{s_1(T_{SD}-T_D)}{\kappa s_2(T_R-T_D)},\ where\ T_{SD} = T_D + \frac{\gamma\lambda E}{\rho c_P g_A s_1} \quad (15–16)$$

$$\alpha = \frac{g_C\left(e_0^* - e_A\right)\left[2s+2\gamma+\gamma\frac{g_A}{g_C}(1+M)\right]}{2s\left[\gamma(T_0-T_A)\left(g_A+g_C\right)+g_C\left(e_0^*-e_A\right)\right]} \quad (17)$$

where D_0 is the atmospheric vapor pressure deficit at the source/sink height (hPa), T_{SD} is the dew-point temperature at the source/sink height (ºC), T_D is the dew-point temperature (ºC), κ is the ratio between (e_0^*–e_A) and (e_S^*–e_A) (unitless), where e_S^* represent the saturation vapor pressure at the surface (hPa), s_1 is the slope of saturation vapor pressure versus temperature between (T_{SD}–T_R) versus (e_0–e_A) (hPa K^{-1}) and s_2 the slope of the saturation vapor pressure and temperature between (T_R–T_D) versus (e_S^*–e_A) (hPa K^{-1}), where T_R is the radiometric surface temperature (ºC). More detailed derivations of Equations 13 to 17 in conjunction with initial values and equations of these unknown variables can be found in Appendix 1 and Mallick et al. (2016).

Finally, the surface energy fluxes are estimated by using dimensionless decoupling coefficient (omega, Ω) by Jarvis and McNaughton (1986), which is considered to present the degree of stomatal control on transpiration. In other words, Ω is presenting the magnitude of coupling between the surface conditions and the free air stream, and it is ranging from 0.0 (perfect coupling) to 1.0 (complete isolation) (Kumagai et al., 2004). Ω is presented as follows (Jarvis and McNaughton, 1986):

$$\Omega = \frac{\frac{s}{\gamma}+1}{\frac{s}{\gamma}+1+\frac{g_A}{g_C}} \quad (18)$$

When introducing Ω into Penman-Monteith equation (Equation 6), λE can be written as follows and H estimated using the surface energy balance ($\phi = H + \lambda E$):

$$\lambda E = \Omega\lambda E_{eq} + (1 - \Omega)\lambda E_{ipm} \quad (19)$$

$$\lambda E_{eq} = \frac{s\phi}{s+\gamma} \quad (20)$$

$$\lambda E_{ipm} = \frac{\rho c_P}{\gamma} g_C D_A \quad (21)$$

$$H = \phi - \lambda E \quad (22)$$

where λE_{eq} represents the equilibrium latent heat flux, which could be obtained over a wide surface with uniform moisture availability (Jarvis and McNaughton, 1986). λE_{eq} is depending on the net available energy (Equation 20). λE_{imp} is presenting the imposed latent

heat flux, which is occurring under limited soil moisture availability. This flux is imposed by the atmosphere through vapor pressure deficit, and λE becomes proportional to g_C.

In addition to estimation for surface energy fluxes, STIC1.2 consists of a feedback loop describing the relationship between T_R and λE. The initial estimates of the unknowns described earlier (e_0^*, e_0, M and α) are calculated as explained in Appendix 1 in order to calculate the first estimates of state variables, which can further be used to calculate the first estimates of λE and H. When this initial calculation step is completed, the unknowns are estimated again based on the first estimate of λE. This iteration loop continues until stable values of e_0^*, e_0, M, α and λE are obtained. Mallick et al. (2016) reported that stable values can be achieved within approximately 25 iterations. The whole STIC1.2 framework is presented in Figure 6. The main differences between STIC versions 1.0, 1.1 and 1.2 are presented in Mallick et al. (2016).

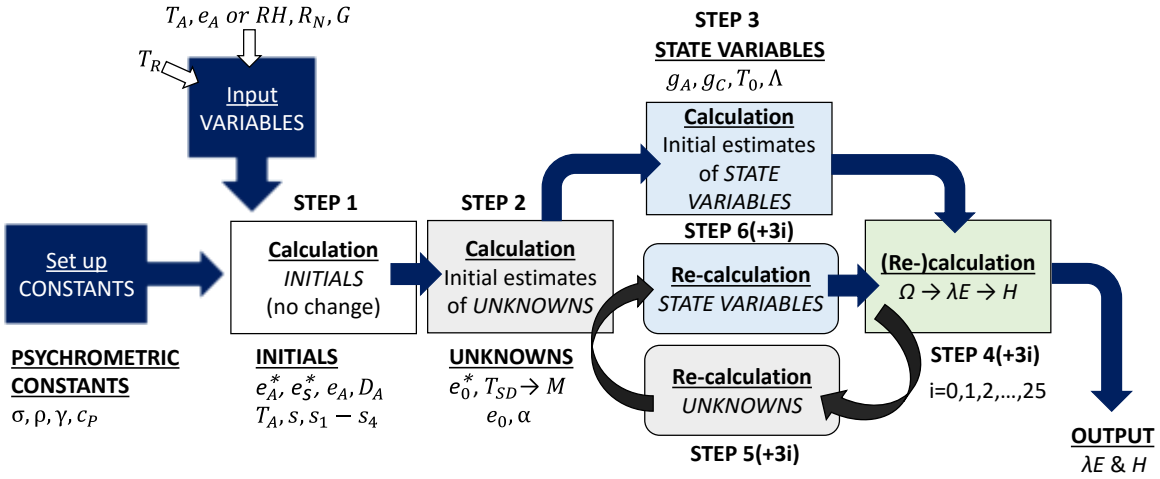

Figure 6 The calculation process of STIC1.2. The re-calculation loop is repeated until the steady values of state variables and flux estimates are obtained (requires approximately 25 iterations).

4.1.2 Priestley-Taylor-JPL (PT-JPL)

Surface energy fluxes are estimated using the Priestley-Taylor method by Jet Propulsion Laboratory (PT-JPL) to assess the performance of STIC1.2. PT-JPL method is based on a bio-meteorological approach which aims to estimate PT based potential ET as actual ET without the need of site specific parametrization. The inputs of PT-JPL are R_N, G, normalized difference vegetation index (*NDVI*), soil adjusted vegetation index (*SAVI*), maximum air temperature (T_{max}) and e_A or *RH*. (Fisher et al., 2008.) R_N and G are directly taken from the OzFlux data, and T_{max} and e_A or *RH* can be assigned from the same OzFlux dataset.

In this study, *NDVI* and *SAVI* are calculated following Fisher et al. (2008) and using MODIS surface reflectance product (MOD09A1). The theoretical range of these variables is between -1–1 (Fisher et al., 2008), and the used equations for these are as follows:

$$NDVI = \frac{r_{NIR} - r_{VIS}}{r_{NIR} + r_{VIS}} \quad (23)$$

$$SAVI = 1.5\frac{r_{NIR}-r_{VIS}}{r_{NIR}+r_{VIS}+0.5} \quad (24)$$

where r_{VIS} is the visible surface reflectance (unitless) and r_{NIR} is the infrared surface reflectance (unitless).

The parameters and their equations required in PT-JPL are described in Table 1. However, to solve these equations, a few other parameters and constants are needed. Following the initial set up by Fisher et al. (2008), these are saturation vapor pressure deficit D_A (hPa) (calculated as in A34 in Appendix 1), the Priestley-Taylor parameter α (1.26, unitless), the psychrometric constant γ (0.67 hPa K^{-1}), β (1.0 kPa), k_{R_N} (0.6, unitless), k_{PAR} (0.5, unitless), m_1 (1.2×1.136, unitless), b_1 (1.2×(-0.04), unitless), m_2 (1.0, unitless) and b_1 (-0.05, unitless).

Table 1 Parameters and their equations used in PT-JPL following Fisher et al. (2008)

Parameter	Description	Equation	Units	Eqn. number
LAI	Total leaf area index	$-ln(1-f_c)/k_{PAR}$	$m^2\ m^{-2}$	(25)
R_{Nc}	Net radiation to canopy	$R_N - R_{Ns}$	$W\ m^{-2}$	(26)
R_{Ns}	Net radiation to soil	$R_N exp(-k_{R_N} LAI)$	$W\ m^{-2}$	(27)
T_{opt}	Optimum plant growth temperature	T_{max} at max $\{R_N f_{APAR} T_{Amax}/D_A\}$	°C	(28)
f_{APAR}	Fraction of PAR absorbed by green vegetation cover	$m_1 SAVI + b_1$	Unitless	(29)
f_{IPAR}	Fraction of PAR intercepted by total vegetation cover	$m_2 NDVI + b_2$	Unitless	(30)
f_c	Fractional total vegetation cover	f_{IPAR}	Unitless	(31)
f_g	Green canopy fraction	f_{APAR}/f_{IPAR}	Unitless	(32)
f_M	Plant moisture constraint	$f_{APAR}/f_{APARmax}$	Unitless	(33)
f_T	Plant temperature constraint	$exp\left[-\left(\left(T_{max}-T_{opt}\right)/T_{opt}\right)^2\right]$	Unitless	(34)
f_{wet}	Relative surface wetness	RH^4	Unitless	(35)
f_{SM}	Soil moisture constraint	$RH^{D_A/\beta}$	Unitless	(36)

Table 1 Parameters and their equations used in PT-JPL following Fisher et al. (2008) (continuing from the previous page)

Parameter	Description	Equation	Units	Eqn. number
s	Slope of saturation-to-vapor pressure curve	$4098\frac{e_a^*}{(T_A\text{-}273.3)^2}$ (e_a^* as A30)	hPa K^{-1}	(37)
λE	Evapotranspiration	$\lambda E_c + \lambda E_i + \lambda E_s$	W m^{-2}	(38)
λE_c	Canopy transpiration	$(1\text{-}f_{wet})f_g f_T f_M \alpha \frac{s}{s+\gamma} R_{Nc}$	W m^{-2}	(39)
λE_i	Interception evaporation	$f_{wet}\alpha\frac{s}{s+\gamma}R_{Nc}$	W m^{-2}	(40)
λE_s	Soil evaporation	$\left(f_{wet}+f_{SM}(1\text{-}f_{wet})\right)\alpha\frac{s}{s+\gamma}(R_{Ns}\text{-}G)$	W m^{-2}	(41)

In this study, the calculation of T_{opt} differs slightly from the original proposed PT-JPL framework as it is calculated as T_{max}, which can be obtained as the maximum value of a formula $R_N f_{APAR} T_{Amax}/D_A$, where T_{Amax} represents the maximum observed air temperature (°C). In the original version photosynthetically active radiation PAR is used instead of net radiation. The sensible heat flux, H, is calculated as in Equation 22 ($H = \phi - \lambda E$). The whole PT-JPL framework is presented in Figure 7.

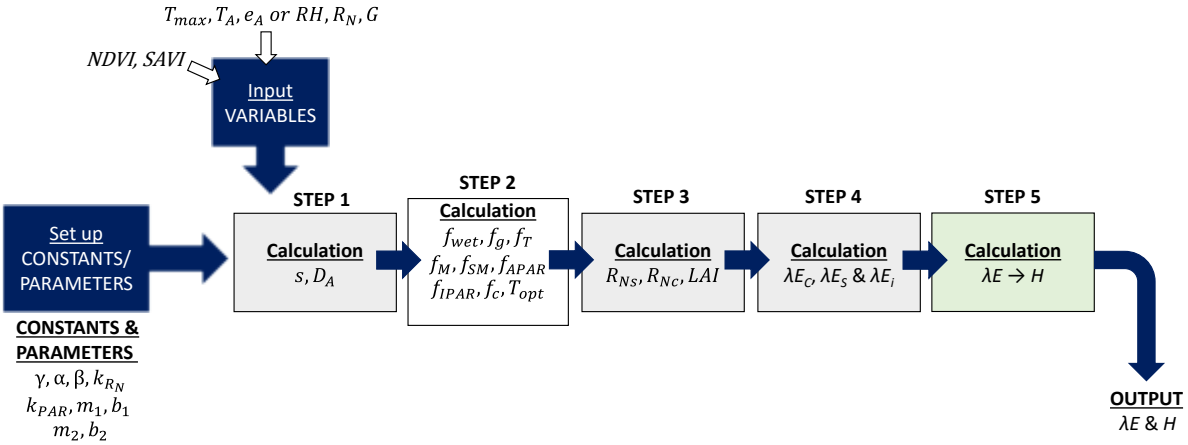

Figure 7 The calculation process of PT-JPL.

4.1.3 MODIS global terrestrial evapotranspiration algorithm (MOD16)

Similarly to PT-JPL, we are using MODIS global terrestrial evapotranspiration (MOD16) algorithm to estimate surface energy fluxes to compare the performance of STIC1.2 and PT-JPL. As the main inputs, this method is requiring land cover, *LAI* and *NDVI* in conjunction with T_A, e_A or *RH* (Mu et al., 2011). In this study, R_N and G are also required and directly taken from the available OzFlux data instead of calculating these by using MODIS data. Also other needed meteorological variables are taken from the Ozflux dataset.

In this study, *NDVI* is calculated as presented in Equation 23, *LAI* as in Equation 25 and fractional total vegetation cover (f_c) as in Equation 31 using the MODIS surface reflectance

product (MOD09A1). MOD16 method also requires many other constants and parameters, which are partly site specific. In general, this method is estimating separately evaporation from wet canopy surface, plant transpiration and soil evaporation.

Table 2 presents the used equations for estimating wet canopy evaporation. The used constants are the psychrometric constant γ (6.7 Pa/K), Stefan-Boltzmann constant σ (5.678×10^{-8} J K^{-4} m^{-2} s^{-1}), specific heat for constant pressure c_P (1003.5 J/kg/K) and the air density ρ (1.234 kg m^{-3}) and s is the slope of the saturation vapor pressure versus air temperature (hPa K^{-1}) (calculated as A35 but using e_S^*). Saturation vapor pressure e_S^* is calculated followed by Henderson-Sellers (1984) and vapor pressure (e) as atmospheric vapor pressure ($e = e_S^* - D_A$). T_i (°C) represents the daytime or night-time average temperature. Leaf conductance to sensible heat per unit LAI (gl_{sh}) (s m^{-1}) and leaf conductance to evaporated water vapor per unit LAI (gl_{eww}) (s m^{-1}) are site specific. These values for different biomes are described in Table A4 (Appendix 2) along with other site specific parameter values, which are used to calculate plant transpiration and soil evaporation.

Table 2 Parameters and their descriptions, equations and units for calculation of wet canopy surface evaporation following Mu et al. (2011)

Parameter	Description	Equation	Unit	Eqn. number
A_c	Energy received by canopy	$f_c R_{N,}$	W m^{-2}	(42)
e_A	Atmospheric vapor pressure	e_S^* - $D_{A,}$ where D_A calculated as in A35	Pa	(43)
e_S^*	Saturation vapor pressure	$2.1718*10^{10} exp\left[\frac{-4157}{(T_A+273)-33.91}\right]$	Pa	(44)
f_{wet}	Water cover fraction	$\begin{cases} 0.0 & RH<70\% \\ RH^4 & 70\%\leq RH\leq 100\% \end{cases}$	Unitless	(45)
r_{hc}	Wet canopy resistance to H	$\frac{1}{gl_{sh} LAI f_{wet}}$	s m^{-1}	(46)
r_{hrc}	Aerodynamic resistance	$\frac{r_{hc} r_{rc}}{r_{hc}+r_{rc}}$	s m^{-1}	(47)
r_{rc}	Resistance to radiative heat transfer through air	$\frac{\rho C_P}{4\sigma T_i^3}$	s m^{-1}	(48)
r_{vc}	Wet canopy resistance	$\frac{1}{gl_{eww} LAI f_{wet}}$	s m^{-1}	(49)
λE_{wet_c}	Wet canopy surface evaporation	$\frac{\left(sA_c f_c+\rho c_P\left(e_S^* - e_A\right) f_c / r_{hrc}\right) f_{wet}}{s+\gamma \frac{r_{vc}}{r_{hrc}}}$	W m^{-2}	(50)

Table 3 presents the used equations to estimate plant transpiration evaporation, which includes transpiration occurring both at daytime and night-time. There C_L represents the mean potential conductance per unit leaf area (s m^{-1}), $m(T_{min})$ a multiplier that limits potential conductance by minimum air temperatures (T_{min}, °C) and $m(D_A)$ a multiplier that reduces the

potential stomatal conductance in case of high D_A (Pa). These variables are site specific and their values can be found in Table A4 (Appendix 2). *i* represents the variable value at daytime and night-time. In this study, P_a is set as 10000 Pa. T_i (°C) represents the daytime or night-time average temperature. g_{cu} represents cuticular conductance per unit *LAI* and it is constant for all the sites (000001 s m^{-1}). Leaf conductance to sensible heat per unit *LAI* (gl_{sh}) (s m^{-1}) is set as described earlier in this Section, and it is equal to leaf-scale boundary layer conductance gl_{bl} (s m^{-1}). Radiative heat transfer (r_r) is calculated similarly to r_{rc} in Equation 48. Water cover fraction f_{wet} is calculated as in Equation 45. The rest of the constants (σ, c_P, ρ, s and γ) and variables (A_c, T_i, f_c, e_{sat} and e) have been described earlier in this Section. The Priestley-Taylor constant (α) is set to 1.26.

Table 3 Parameters and their descriptions, equations and units for calculation of plant transpiration evaporation following Mu et al. (2011)

Parameter	Description	Equation	Unit	Eqn. number
C_C	Canopy conductance	$C_S LAI$	s m^{-1}	(51)
C_{Ci}	Canopy conductance	$\begin{cases} \frac{G_S2(G_{Si}1+G_{CU})}{G_{Si}1+G_S2+G_{CU}} LAI(1-f_{wet}), \\ if\ (LAI>0, (1-f_{wet})>0 \\ 0.0, \quad if\ (LAI=0, (1-f_{wet})=0) \end{cases}$	s m^{-1}	(52)
C_S	Stomatal conductance	$C_L m(T_{min}) m(D_A)$	s m^{-1}	(53)
G_{CU}	Leaf cuticular conductance	$g_{cu} r_{corr}$	s m^{-1}	(54)
G_S2	Leaf boundary-layer conductance	gl_{sh}	s m^{-1}	(55)
G_{Sday}	Daytime stomatal conductance	$C_L m(T_{min}) m(D_A) r_{corr}$	s m^{-1}	(56)
r_a	Aerodynamic resistance	$\frac{r_h r_r}{r_h + r_r}$	s m^{-1}	(57)
r_{corr}	Corrected resistance	$\frac{1.0}{\frac{101300}{P_a} * \left(\frac{T_i+273.15}{293.15}\right)^{1.75}}$	s m^{-1}	(58)
r_h	Convective heat transfer	$\frac{1.0}{gl_{bl}}$	s m^{-1}	(59)
r_{si}	Dry canopy surface resistance to transpiration	$\frac{1.0}{C_{Ci}}$	s m^{-1}	(60)
λE_{trans}	Plant transpiration	$\frac{\left(s+A_C F_C+\rho c_P (e_S^* - e_A)\frac{F_C}{r_a}\right)(1-f_{wet})}{s+\gamma(1+\frac{r_s}{r_a})}$	W m^{-2}	(61)
λE_{pot_trans}	Potential plant transpiration	$\frac{\alpha s A_C (1-f_{wet})}{s+\gamma}$	W m^{-2}	(62)

Table 4 represents the used equations for the last part of MOD16 calculations, soil evaporation, which includes saturated soil surface potential evaporation (λE_{SOIL_POT}) and moist soil surface evaporation (λE_{wet_SOIL}). The needed constants (σ, c_P, ρ, s and γ) and variables (D_A, f_c, f_{wet}, e_{sat}, e and r_a) have been described earlier in this Section. Radiative heat transfer (r_{rs}) is calculated similarly to r_{rc} in Equation 48. The variable β is set to 200. The variables needed for total aerodynamic resistance (r_{tot}) are rbl_{max}, rbl_{min}, $D_{A_{open}}$ (water stress is not affecting transpiration) and $D_{A_{close}}$(water stress conditions affecting transpiration and causing stomata to close) are site specific and are represented in Table A4 (Appendix 2). r_{corr} is calculated as earlier (Equation 58) and r_{hs} is assumed to be a boundary layer resistance, which can be calculated similarly to r_{tot}.

Table 4 Parameters and their descriptions, equations and units for calculation of soil evaporation following Mu et al. (2011)

Parameter	Description	Equation	Unit	Eqn. number
A_{SOIL}	Energy received by soil	$(1-f_c)(R_N-G)$	W m^{-2}	(63)
r_{as}	Aerodynamic resistance at soil surface	$\frac{r_{hs}r_{rs}}{r_{hs}+r_{rs}}$	s m^{-1}	(64)
r_{tot}	Total aerodynamic resistance to vapor transport	$r_{totc}r_{corr}$	s m^{-1}	(65)
r_{totc}	Total aerodynamic resistance to vapor transport constant	$\begin{cases} rbl_{max}, if D_A \le D_{A_{open}} \\ rbl_{max} - \frac{(rbl_{max} - rbl_{min})(D_{A_{close}} - D_A)}{(D_{A_{close}} - D_{A_{open}})}, \\ if D_{A_{open}} < D_A < D_{A_{close}} \\ rbl_{min}, if D_A \ge D_{A_{close}} \end{cases}$	s m^{-1}	(66)
λE_{SOIL}	Actual soil evaporation	$\lambda E_{wet\_SOIL} + \lambda E_{SOIL\_POT}\left(\frac{RH}{100}\right)^{D_A/\beta}$	W m^{-2}	(67)
λE_{SOIL_POT}	Potential soil evaporation	$\frac{\left(sA_{SOIL} + \rho c_P\left(1-f_c\right)\frac{D_A}{r_{as}}\right)(1-f_{wet})}{s+\gamma\frac{r_{tot}}{r_{as}}}$	W m^{-2}	(68)
λE_{wet_SOIL}	Evaporation from wet soil surface	$\frac{\left(sA_{SOIL} + \rho c_P\left(1-f_c\right)\frac{D_A}{r_{as}}\right)f_{wet}}{s+\gamma\frac{r_{tot}}{r_{as}}}$	W m^{-2}	(69)

Finally, the total evaporation can be calculated as a sum of the three evaporation terms in Tables 2–4 (from wet and dry canopy and soil surface) (Equation 70). Similarly, the total potential evaporation can be calculated as a sum of potential evaporation from wet and dry canopies and soil surface (Equation 71). The sensible heat flux is calculated as in Equation 22 ($H = \phi - \lambda E$) in the same way as in STIC1.2 and PT-JPL. The whole MOD16 framework is presented in Figure 8.

$$\lambda E = \lambda E_{wet\_c} + \lambda E_{trans} + \lambda E_{SOIL} \quad (70)$$

$$\lambda E_{POT} = \lambda E_{wet\_c} + \lambda E_{POT\_trans} + \lambda E_{wet\_SOIL} + \lambda E_{SOIL\_POT} \quad (71)$$

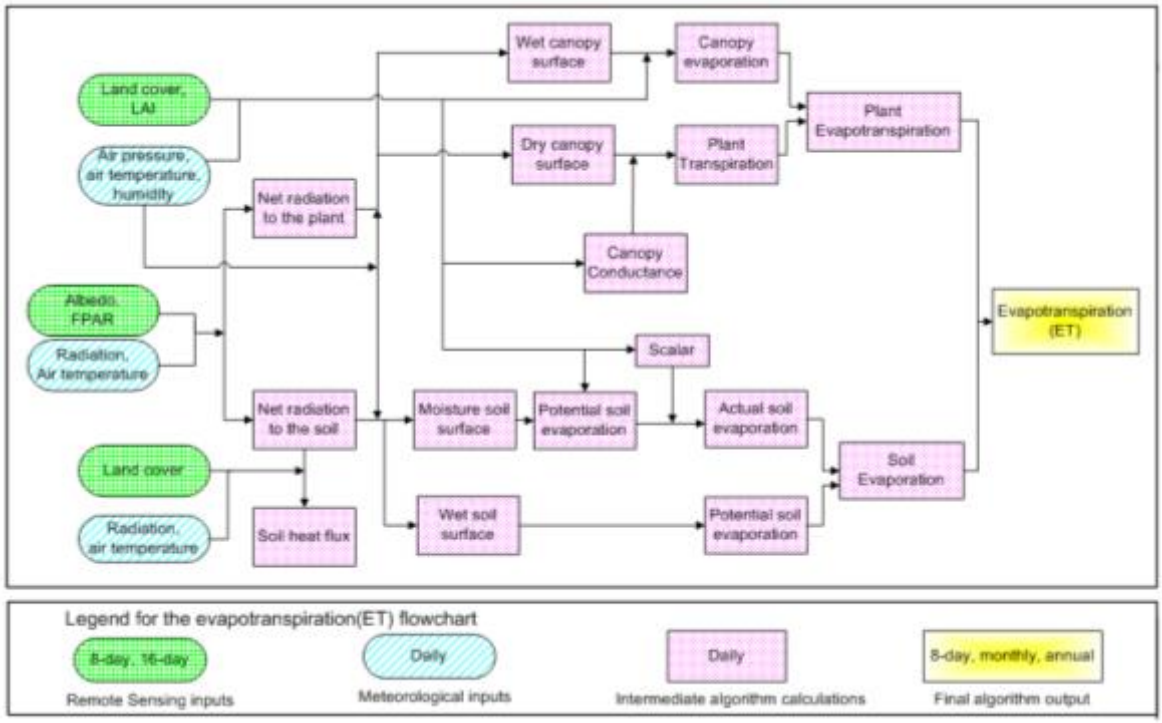

Figure 8 The flowchart of the MOD16 calculation process (Mu et al., 2011).

4.2 Analysis

4.2.1 Statistical analysis

In order to evaluate the efficiency of the proposed modelling technique STIC1.2 and compare its performance against other model results, the following statistical metrics are used: the coefficient of determination (R^2) (Legates and McCabe, 1999), root mean square deviation (*RMSD*) (Willmott, 1982), relative root mean square deviation (*RRMSD*) (Kalma et al., 2008), mean absolute percentage deviation (*MAPD*) (Liu et al., 2010), and the ratio of squared systematic *RMSD* to squared *RMSD* ($RMSD_S^2/RMSD^2$) (Willmott, 1982) (Equation 72 to 76). Total *RMSD* is the sum of $RMSD_S$ and non-systematic *RMSD* ($RMSD_U$) (Willmott, 1982). In general, in a "good model" R^2 value should be high, *RMSD* low and a systematic *RMSD* close to 0 (Yebra et al., 2013). According to Willmott (1982) $RMSD_S$ should be less than $RMSD_U$, and the proportion of the total *RMSD* arising from systematic biases is reflected in the quantity $RMSD_S^2/RMSD^2$. However, $RMSD_S^2/RMSD^2$ is reported only for the sub-daily and 8-day flux estimates. All the calculations are made using Matlab R2014b program by MathWorks.

$$R^2 = \left\{ \frac{\sum_{i=1}^{n} (O_i - \bar{O})(P_i - \bar{P})}{\left[\sum_{i=1}^{n} (O_i - \bar{O})^2\right]^{0.5} \left[\sum_{i=1}^{n} (P_i - \bar{P})^2\right]^{0.5}} \right\}^2 \quad (72)$$

$$RMSD = \left[\frac{1}{n} \sum_{i=1}^{n} (P_i - O_i)^2\right]^{0.5} \quad (73)$$

$$RRMSD = 100\left[\frac{RMSD}{\bar{O}}\right] \quad (74)$$

$$MAPD = \frac{100}{N}\left[\sum_{i=1}^{n}\left|\frac{P_i - O_i}{P_i}\right|\right] \quad (75)$$

$$\frac{RMSDs^2}{RMSD^2} = 100\frac{\left[\frac{1}{n}\sum_{i=1}^{n}(\hat{P}_i - O_i)^2\right]^{0.5}}{\left[\frac{1}{n}\sum_{i=1}^{n}(P_i - O_i)^2\right]^{0.5}} \quad (76)$$

where O_i represents the observed value, P_i is the model-predicted value, n is the number of observations, $\hat{P}_i$ is the estimated value based on the ordinary least-square regression ($\hat{P}_i = c + mO_i$); where m and c are the slope and intercept of linear regression between predicted value on observed value, and $\bar{O}$ is the mean of observed values.

In addition, Taylor diagrams (Taylor, 2001) are used to be able to compare the model performances. The normalised *RMSD* ($RMSD_N$, Equation 77) and R^2 are used as inputs for the Taylor diagram code provided by Rochford (2015). Coefficient of variation for soil moisture (cV_θ) is calculated similarly to the $RMSD_N$ (UCLA, 2016). In addition, the unbiased sample variances (σ^2) of the STIC 1.2 predicted and OzFlux observed surface flux values ($\sigma^2_{\lambda E}$, σ^2_H) as well as the variances of precipitation (σ^2_P), soil moisture (σ^2_θ), surface temperature ($\sigma^2_{T_R}$), air temperature ($\sigma^2_{T_A}$), vapor pressure deficit ($\sigma^2_{D_A}$), wind speed (σ^2_u) and friction velocity (σ^2_{u*}) were calculated as in Equation 78. The values are used to create a scatter between observed and predicted $\sigma^2_{\lambda E}$ (and σ^2_H) at monthly scale as well as correlation matrices between the residual variance in $\sigma^2_{\lambda E}$ or σ^2_H ($\Delta\sigma^2_{\lambda E} = \sigma^2_{\lambda E\ STIC1.2} - \sigma^2_{\lambda E\ observed}$ and $\Delta\sigma^2_H = \sigma^2_{H\ STIC1.2} - \sigma^2_{H\ observed}$) against the other calculated variances.

$$RMSD_N = 100\left[\frac{RMSD}{\bar{O}}\right] \quad (77)$$

$$\sigma^2 = \frac{1}{n-1}\sum_{i=1}^{n}(V_i - \bar{V})^2 \quad (78)$$

where $\bar{O}$ is the mean of observed values, RMDS is calculated as in Equation 73, n is the number of observations, V_i is the variable (either observed value O_i or model-predicted value P_i) and $\bar{V}$ is the mean of the variable.

4.2.2 Daily, monthly, annual and seasonal analysis for STIC1.2 validation

STIC1.2 model was validated using the OzFlux EC data. Daily SEB fluxes (in W m^{-2}) were computed by averaging half-hourly (hourly for AU-Tum) observed fluxes and those predicted by STIC1.2. Monthly E (in mm) and H (converted to equivalent water in mm) (Allen et al., 1998) were computed by summing the daily λE and H values for three ecohydrologically contrasting sites: AU-ASM, AU-Wom and AU-Cow. Annual E and H (both in mm) are calculated for every site by summing the daily SEB fluxes.

Performance of STIC1.2 was also evaluated for dry and wet seasons. The seasons were defined based on monthly precipitation and soil moisture patterns, and therefore the timing and duration of the seasons vary between different sites (Table A5 in Appendix 2).

4.2.3 8-day analysis for model comparison

To be able to analyse the performance of STIC1.2, PT-JPL and MOD16 models which are using MODIS 8-day data and OzFlux data, the mean of EC data is calculated for 8-days (in W m^{-2}). This sub-daily EC value of SEB fluxes for each day was selected at the time when the satellite was passing (ranging between 10 to 12 a.m.). After this calculation, MODIS and OzFlux data were comparable.

4.2.4 Uncertainty analysis

Uncertainty analysis was performed at monthly scale by calculating a "normalised sensitivity" of seasonal evaporation (E) and sensible heat (H) to seasonal precipitation (P) following Fatichi and Ivanov (2014) to analyse the ecohydrological responses of the fluxes. The normalized sensitivity of the fluxes (S) to monthly precipitation was computed from the slope of the linear relationship (the linear least squares fit, β) between an estimated SEB flux variable (E or H) at monthly scale and monthly precipitation multiplied by the ratio of total precipitation (P_{tot}) to the SEB flux for the seasons (V_s) (Equation 79). The one-month lag to the sensitivity of E to P (zero lag for H to P) was computed from daily data for all the sites. Monthly P, E, and H were also segregated according to dry and wet season for every site, followed by grouping of the sites according to the three ecohydrological classes.

$$S = \beta \frac{P_{tot}}{V_s} \tag{79}$$

5 Results

5.1 Validation of STIC1.2 using OzFlux data

5.1.1 Evaluating sub-daily, daily, and annual SEB fluxes

Estimates of λE and H from STIC1.2 at half-hourly (hourly for AU-Tum) temporal resolution are compared to the EC flux observations and the error statistics of individual sites are detailed in Appendix 2 (Table A6). Statistical errors for λE for three ecohydrologically contrasting ecosystem classes show that for all the sites the average of R^2 was 0.59, *RMSD* 48 W m^{-2}, *MAPD* 49% and $RMSD_S^2/RMSD^2$ 46%.

The poorest agreement between modelled and measured values is detected in the dry sites (annual P < 350 mm), where the average R^2 was the lowest (0.36), and *MAPD* as well as *RRMSD* were the highest (61% and 78%, respectively) (Figures 9a, 9b, 9c). Also, the average ratio of $RMSD_S^2/RMSD^2$ was relatively high for the dry sites (52%, range 34% to 76%). However, the average *RMSD* was the lowest, 37 W m^{-2}. Contrastingly, the relationship between modelled and observed λE was stronger for the semi-dry (350 mm < P < 700 mm) and wet (annual P > 700 mm) sites, where the average R^2 varied between 0.54 and 0.85, respectively. Also a substantial reduction was detected in *MAPD* and *RRMSD*: the average *MAPD* values were 55% and 32% and *RRMSD* values 70% and 37% for the semi-dry and wet sites, respectively (Figures 9a, 9b, and 9c). Also the average $RMSD_S^2/RMSD^2$ values were reduced to 37% for the semi-dry sites and to 13% for the wet sites, which reveals a high systematic error in the soil moisture controlled ecosystems when compared to the radiation controlled ecosystems (Figure 9d). However, the average *RMSD* values were slightly higher for the semi-dry (50 W m^{-2}) and wet sites (53 W m^{-2}).

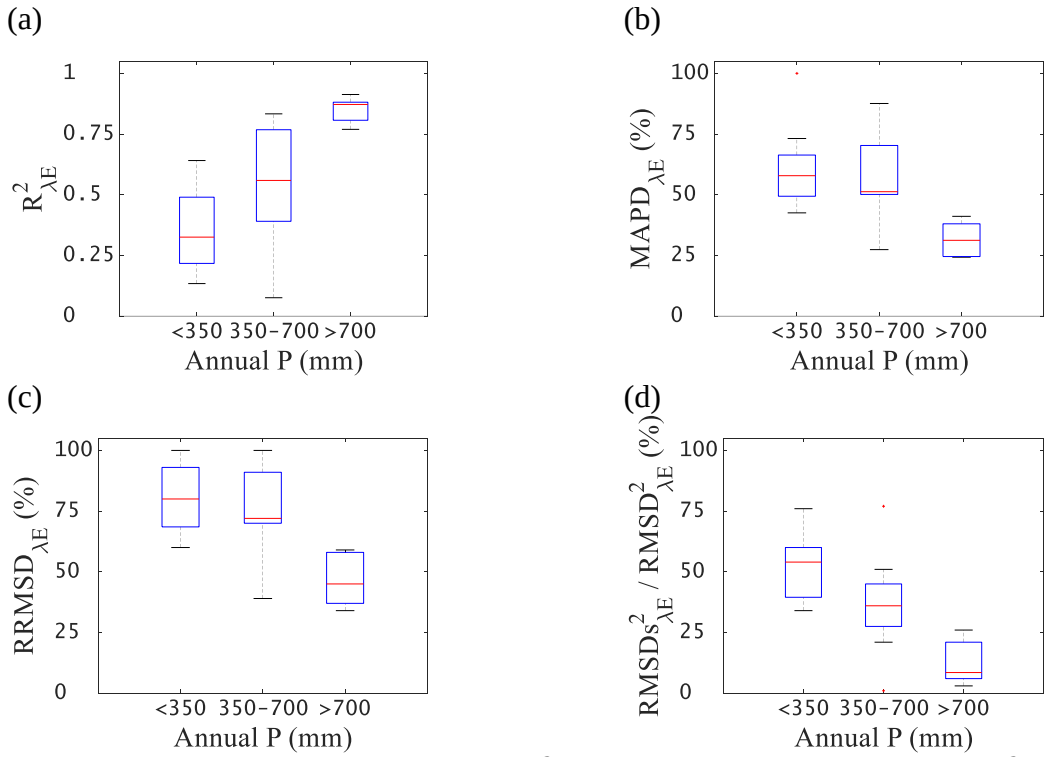

Figure 9 Boxplots of statistical error matrices (R^2 (a), *MAPD* (b), *RRMSD* (c) and $RMSD_S^2/RMSD^2$ (d)) between STIC1.2 predicted versus observed λE in three ecohydrologically diverse Australian ecosystem groups. P represents the amount of received precipitation.

The predictive accuracy of *H* followed the opposite pattern when compared to λE, featuring the maximum average R^2 (0.96) and minimum average errors (15% *MAPD* and 12% *RRMSD*) in the water-controlled dry ecosystems compared to the more energy-controlled semi-dry and wet ecosystems, where the average R^2 varied between 0.84–0.91, *MAPD* 25–40%, and *RRMSD* 35–60%, respectively (Figures 10a, 10b, 10c). Interestingly, the average ratio of $RMSD_S^2/RMSD^2$ varied between 19–23% (Figure 10d) for all the sites, thus indicating low systematic errors in *H* estimates over a broad spectrum of ecohydrologically contrasting environments. The RMDS values were similar than for the λE estimations: the lowest values were detected for the dry sites (33 W m^{-2}) and higher values for the semi-dry (50 W m^{-2}) and wet sites (53 W m^{-2}). The mean values for all the sites were: 0.90 (R^2), 46 W m^{-2} (*RMSD*), 27% (*MAPD*) and 22% ($RMSD_S^2/RMSD^2$).

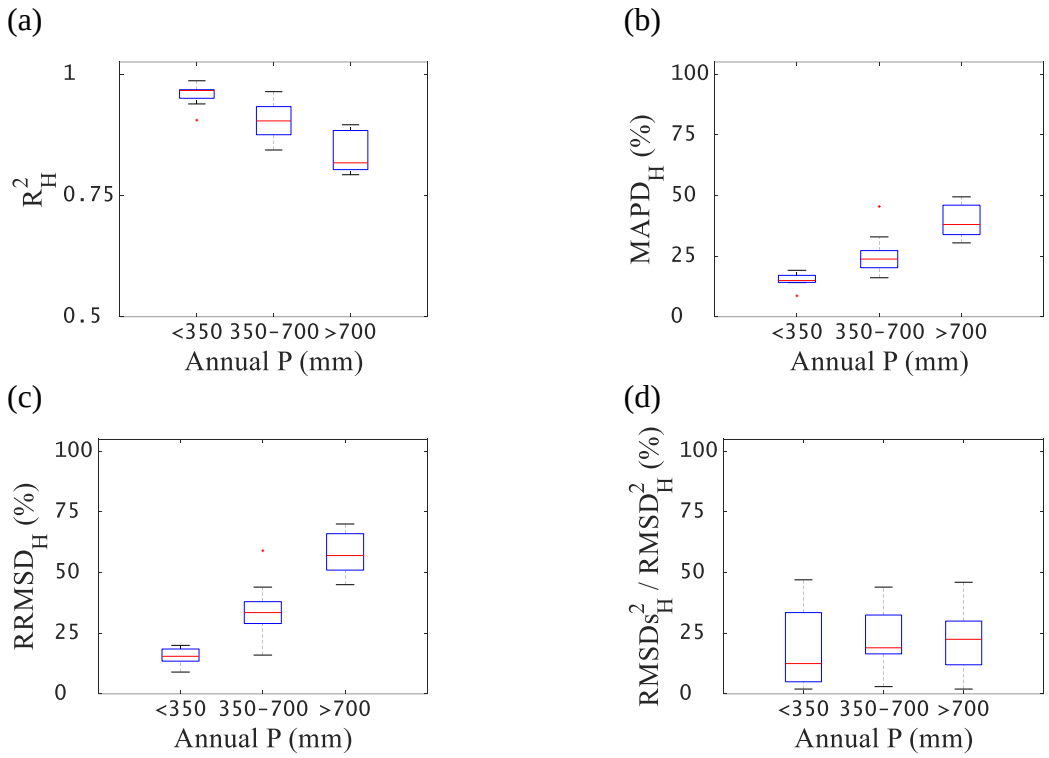

Figure 10 Boxplots of statistical error matrices (R^2 (a), *MAPD* (b), *RRMSD* (c) and $RMSD_S^2/RMSD^2$ (d)) between STIC1.2 predicted versus observed *H* in three ecohydrologically diverse Australian ecosystem groups. *P* represents the amount of received precipitation.

STIC1.2 showed better performance in capturing the daily λE and *H* magnitudes over all the ecosystems. Thus, the errors in daily fluxes were reduced when compared to half-hourly fluxes due to cancellation of random errors. For daily values over the dry sites, the average R^2 increased from 0.36 (sub-daily) to 0.55, *MAPD* and *RMSD* reduced from 61% (sub-daily) to 55% and from 37 W m^{-2} (sub-daily) to 11 W m^{-2}, respectively (Figure 11a). The slopes of regression varied to the order of 0.55 (Figure 11a). For the semi-dry and wet ecosystems, the average R^2 stayed in the similar range (0.65–0.81) compared to sub-daily values (0.54–0.85), *MAPD* values decreased from 32–55% to 20–39% in addition to decreasing RSMS values from 50–53 W m^{-2} to 17–18 W m^{-2} (Figures 11b, 11c). The slopes of regression varied between 0.70 and 0.84 for the semi-dry and wet sites (Figures 11b, 11c).

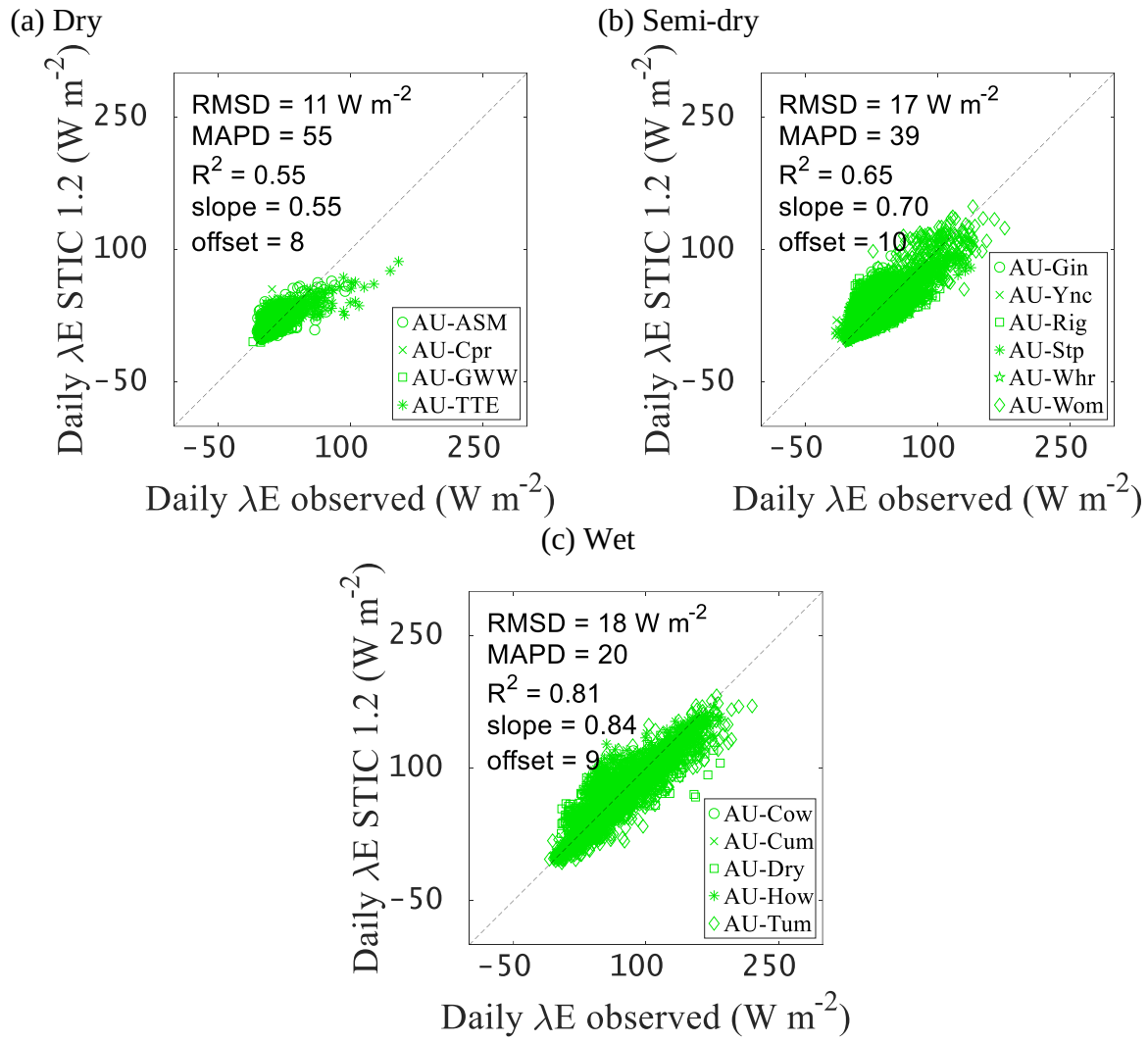

Figure 11 Comparison of STIC1.2 predicted daily *λE* with measured SEBS flux components in ecohydrologically dry (a), semi-dry (b) and wet (c) ecosystem groups. Data from the sites falling under the same ecohydrological class are combined together.

The statistics of daily *H* fluxes showed that the mean R^2 decreased slightly from 0.96 (sub-daily) to 0.93 for the dry sites (Figure 12a). However, both *MAPD* and *RMSD* decreased from 15% (sub-daily) to 12% and from 33 W m^{-2} to 12 W m^{-2} (Figure 12a). Similarly than for the dry sites, the average R^2 for the semi-dry and wet sites decreased from 0.84 and 0.91 (sub-daily) to 0.73 and 0.87. Also in this case, the average *MAPD* (25–37%) and *RMSD* (19–20 W m^{-2}) values were lower than for sub-daily fluxes (*MAPD* 25–40%, RMDS 50–53 W m^{-2}) (Figures 12b, 12c). As for sub-daily statistics, the predictive errors in daily *H* were the lowest in the dry ecosystems.

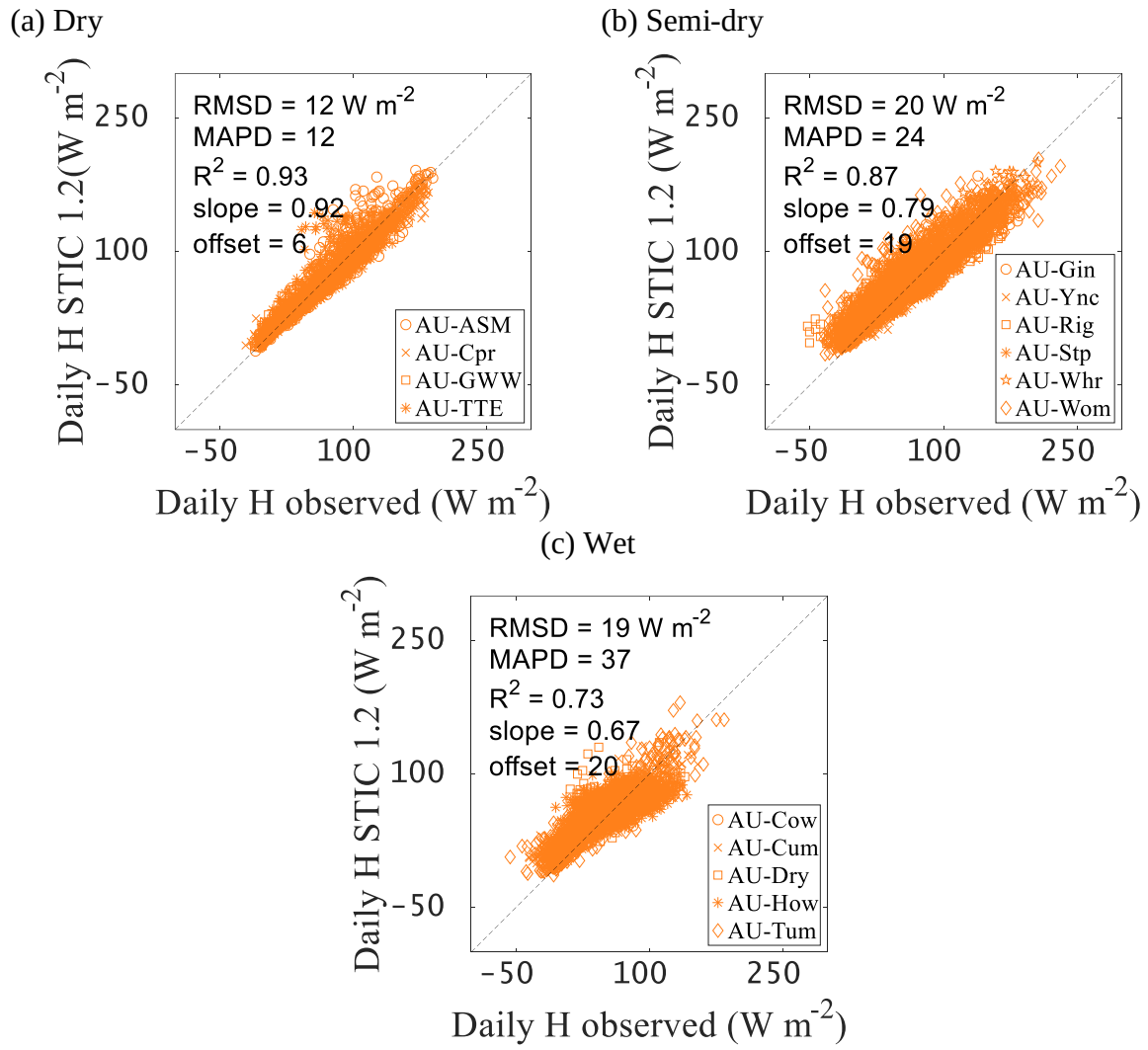

Figure 12 Comparison of STIC1.2 predicted daily *H* with measured SEBS flux components in ecohydrologically dry (a), semi-dry (b) and wet (c) ecosystem groups. Data from the sites falling under the same ecohydrological class are combined together.

The magnitude and variability of annual *E* and *H* (both observed and predicted) across an ecohydrological transect (latitude) from North to South of Australia revealed a wide amplitude in both variables, ranging from 100 to 1250 mm (Figures 13a, 13b) accompanied by a substantial rainfall variability between 200 to 4000 mm. In general, low values of *E* (100–125 mm) and high values of *H* (900–1200 mm) were found between latitudes of 20–30 °S representing the dry and semi-dry ecosystems. In contrast, high values of *E* (500–1250 mm) and low values of *H* (400–700 mm) were found between latitudes of 12–18 °S and 35–40 °S representing sub-humid to humid ecosystems, respectively. An evaluation of annual fluxes in Figure 14 showed a very good agreement between the observed and predicted *E* and *H* where STIC1.2 explained 93–97% of the measured variability, with *MAPD* and *RMSD* being in the order of 10% and 60–92 mm, respectively.

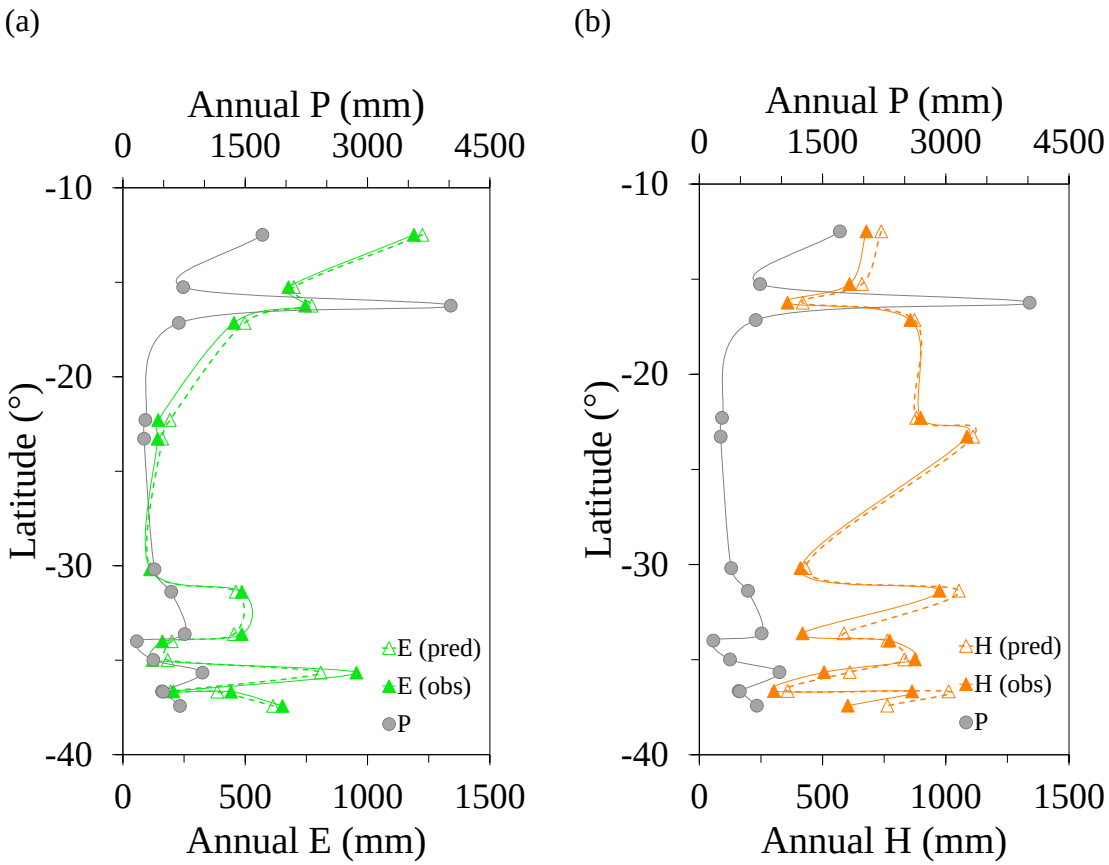

Figure 13 Variability of observed and predicted annual *E* (a) and *H* (b) along latitudinal transect of Australian ecosystems representing the ecohydrological gradient. Precipitation (*P*) is shown as a reference.

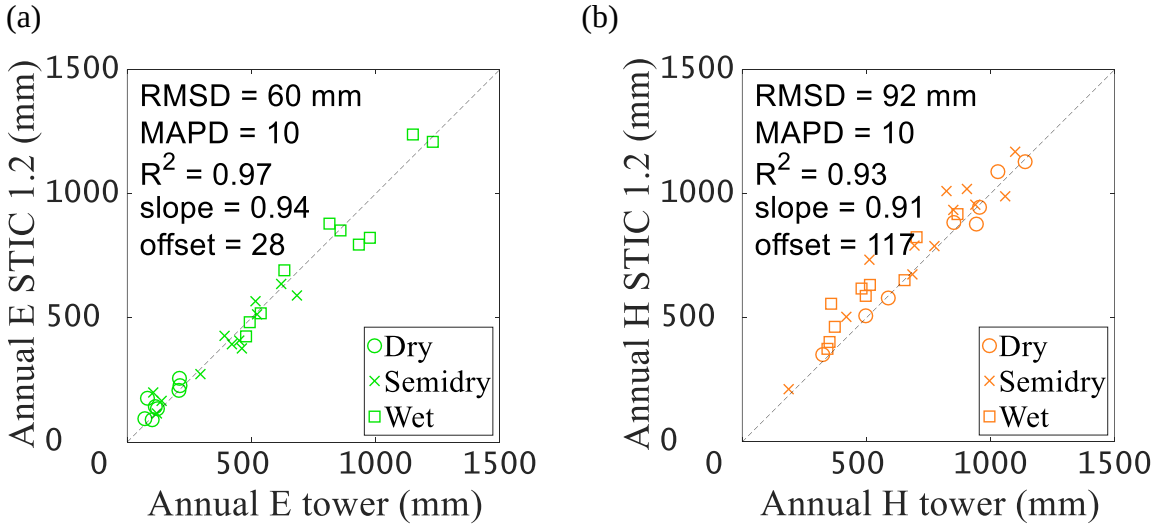

Figure 14 Validation of STIC1.2 estimates of annual *E* (a) and *H* (b) against EC tower measurements. These are the annual sum of *E* and *H* for years 2013 and 2014 at each of the flux tower sites categorized according to their ecohydrological class.

5.1.2 Monthly flux variability

Over two example years (2013–2014), distinct dry and wet seasons were identified in the semi-dry and wet ecosystems. In the dry ecosystem (AU-ASM, Figure 15a), low P and θ resulted in a nearly constant E rate without a substantial month-to-month variation. P is highly variable, but most of the precipitation occurs in the wet season from November to December. However, a correlation between precipitation and evaporation rate can be detected: E is increasing (and H decreasing) after precipitation events (result not shown). Relatively lower E was found in 2014 due to a 50% reduction in annual P and therefore, H was larger than E. The STIC1.2 modelling framework faithfully captured the observed ecohydrological effects on seasonal E and H dynamics in a water-controlled ecosystem. In the semi-dry ecosystem (AU-Wom, Figure 15b), E during the dry season was reduced due to low P and θ, which caused substantial water limitations from January to April in both years. E rate during the dry season is still higher compared to the winter time wet season (May to October), suggesting the ecosystem is not water-limited but rather radiation-controlled. In this semi-dry ecosystems, the magnitudes of both E and H were found to be similar. Interestingly, in the wet ecosystem (AU-Cow, Figure 15c), monthly E decreased by 20–70% during the wet season of year 2014 (January–May) when P was larger than 600 mm per month. This is in contrast to the wet season of year 2013 when P was nearly 1500 mm below the average. In the wet ecosystem, E during the dry season (June–October) was found to be higher than during the wet season (December–January), and E was found to dominate over H during all seasons.

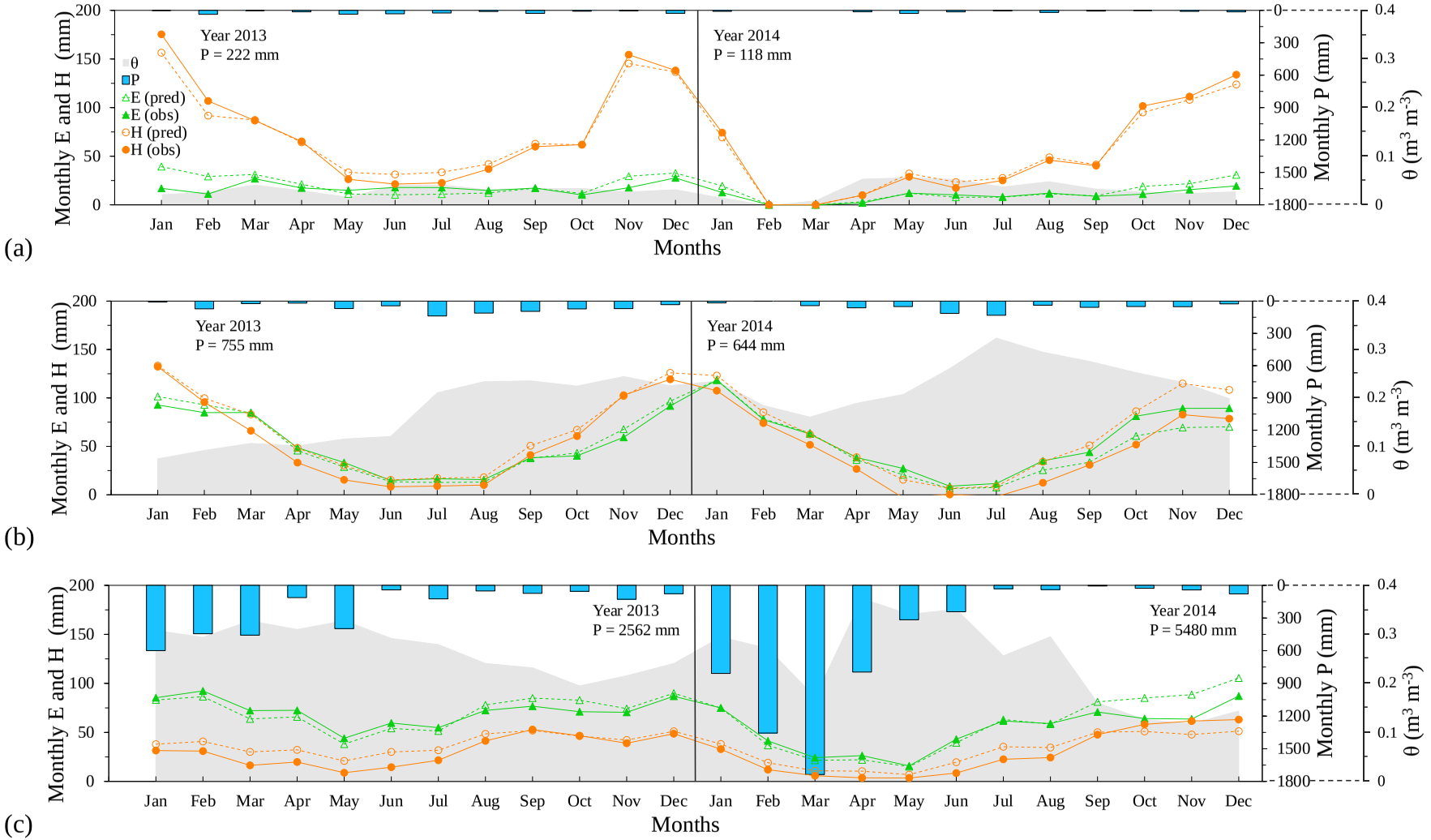

Figure 15 Illustrative examples of monthly variability of observed and predicted *E* and *H* along with monthly rainfall (*P*) and soil moisture (*θ*) in three representative dry (AU-ASM, a), semi-dry (AU-Wom, b) and wet (AU-Cow, c) ecosystems for the years 2013 and 2014.

5.1.3 Dry versus wet season fluxes

The Taylor diagram (Figure 16, see Section 4.2.1 for the description of the Taylor diagram) reveals overall low errors of STIC1.2 predicted *H* for the dry and semi-dry ecosystems during both dry and wet seasons, with $RMSD_N$ and correlation between observed and modelled *H* of 28–30% and 0.76–0.95, respectively. However, we can see that the errors in modelled *H* are slightly increasing in the dry and semi-dry sites during the wet season. The correlation coefficient (*r*) for *H* in the dry sites is decreasing from 0.95 (dry season) to 0.9 (wet season), but in the semi-dry sites there is no difference between the two seasons. However, the errors of *H* in the wet sites are higher ($RMSD_N$ 79–100%) and correlation coefficients (0.64–0.72) are lower compared to the dry and semi-dry sites. Also, the agreement between observed and modelled fluxes is better during the wet season for the wet sites as opposite to the dry and semi-dry sites.

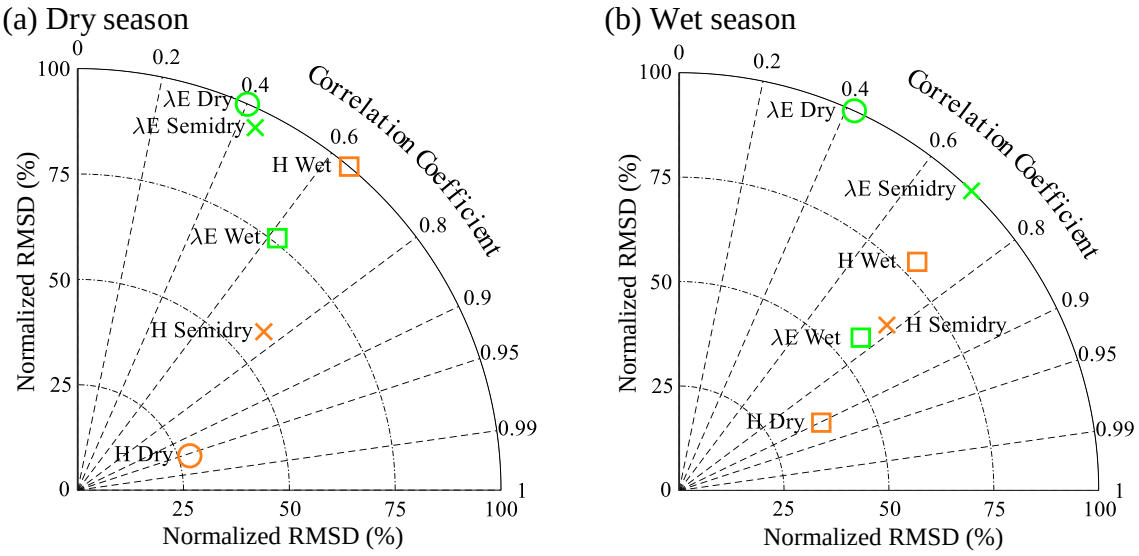

Figure 16 Taylor diagram of error statistics showing the $RMSD_N$ and correlation coefficient between observed and predicted λE and *H* during dry (a) and wet (b) seasons of 2013–2014 in three ecohydrologically contrasting Australian ecosystem groups (dry, semi-dry, and wet). Data from the sites falling under same ecohydrological class are combined together.

Figure 16 shows no substantial differences between the errors of λE during the wet and dry seasons for the dry and semi-dry ecosystems ($RMSD_N$ 95–100%), and there was almost no change for *r* in the dry sites (0.40–0.42). However, for the semi-dry sites, *r* increased for the wet season (0.70) compared to dry season (0.44). This was also detected for the wet sites, where *r* increased from 0.62 (dry season) to 0.76 (wet season). In addition, the error of λE was lower (57%) during the wet season in the wet ecosystems as compared to the dry seasons (76%).

Table 5 shows the sensitivities of observed and STIC 1.2 estimated *E* and *H* to variability in *P* and ϕ. The sensitivity of *H* to variability in *P* ($S_{H,P}$) (see Section 4.2.4 for description of *S*) revealed substantially high $S_{H,P}$ during the dry season in the dry and semi-dry ecosystems [(-0.61)–(-0.71) and (-0.43)–(-0.45), respectively] as compared to $S_{E,P}$ which was lower during the dry season in the wet ecosystems [(-0.15)–(-0.18)]. During the wet season, the dry ecosystems have higher $S_{H,P}$ [(-0.08)–(0.14)] when compared to the semi-dry and wet ecosystems, which are almost insensitive to the precipitation variability [(-0.01)–(-0.02)]. In

comparison, the sensitivity of E to P variability ($S_{E,P}$) show that during the wet season $S_{E,P}$ is higher for the dry and semi-dry ecosystems (0.42–0.61) compared to the wet ecosystems ($S_{E,P}$ 0.3). Interestingly, during the dry season, $S_{E,P}$ is moderate for the semi-dry sites (0.3–0.34), and low for the dry and wet sites (0.09–0.13). E was more closely associated with the available energy during the dry season in the wet ecosystems (r = 0.82) and during both the seasons in the semi-dry ecosystems as evident from the good correlation (r = 0.65–0.87). For the dry ecosystems, the E is not as radiation-controlled either during the dry or the wet season (r = 0.18 and r = 0.44, respectively).

Table 5 Sensitivity of observed and STIC1.2 derived E and H to P ($S_{E,P}$ and $S_{H,P}$) during the dry and wet season over ecohydrologically dry, semi-dry and wet ecosystem groups along with the correlation between E and net available energy (ϕ) ($r_{E,\phi}$). See section 4.2.4 for the definitions of $S_{E,P}$ and $S_{H,P}$.

Ecohydrological class	$S_{E,P}$ (obs.)		$S_{E,P}$ (STIC)		$S_{H,P}$ (obs.)		$S_{H,P}$ (STIC)		$r_{E,\phi}$	
	Dry	Wet	Dry	Wet	Dry	Wet	Dry	Wet	Dry	Wet
Dry	0.13	0.61	0.09	0.55	-0.71	-0.14	-0.61	-0.08	0.18	0.44
Semi-dry	0.34	0.42	0.30	0.53	-0.45	-0.01	-0.43	-0.02	0.65	0.87
Wet	0.15	0.30	0.09	0.30	-0.18	-0.02	-0.15	-0.02	0.82	0.44

5.1.4 Ecohydrological factors and error characterization

To examine the effects of ecohydrological signatures on the prediction of SEB fluxes, further investigation was made on the patterns of *MAPD* in daily λE and H in comparison to the coefficient of variation of θ (cV_θ, see Section 4.2.1 for calculation), evaporative index (annual E/R_N ratio), ε, and Budyko climatic dryness (annual E_P/P ratio) (Figure 17). The directions of relationships between *MAPD* and ecohydrological indicators are opposite to each other for λE and H. ε (Figure 17a) and the annual E/R_N ratio (Figure 17b) had maximum impact on the *MAPD* of both fluxes. As evident from the slopes of the regression lines, 1% increase in ε was found to cause approximately 17% decrease and 15% increase in $MAPD_{\lambda E}$ and $MAPD_H$, respectively. An increase of 10% in E/R_N would cause a 76% decrease and 55% increase in $MAPD_{\lambda E}$ and $MAPD_H$, respectively. A systematic increase in $MAPD_{\lambda E}$ was found with increasing cV_θ (Figure 17c). However, the impact of cV_θ was approximately 50% less for the accuracy of predicted H, as evident from the slope of the regression line (slope = 0.19). Interestingly, a logarithmic increase in $MAPD_{\lambda E}$ was found with increasing climatic dryness (Figure 17d). $MAPD_{\lambda E}$ varied between 18–30% for E_P/P ratio of 0–2.5 and it progressively increased to 55–100% when E_P/P ratio exceeded 5 (Figure 17d). The scatter between annual E and P (Figure 17e) also revealed that STIC1.2 modelling framework is capable of capturing the precipitation driven variability over different ecosystems: annual E rate is exceeding P in the dry sites but does not increase linearly when precipitation rates are increasing.

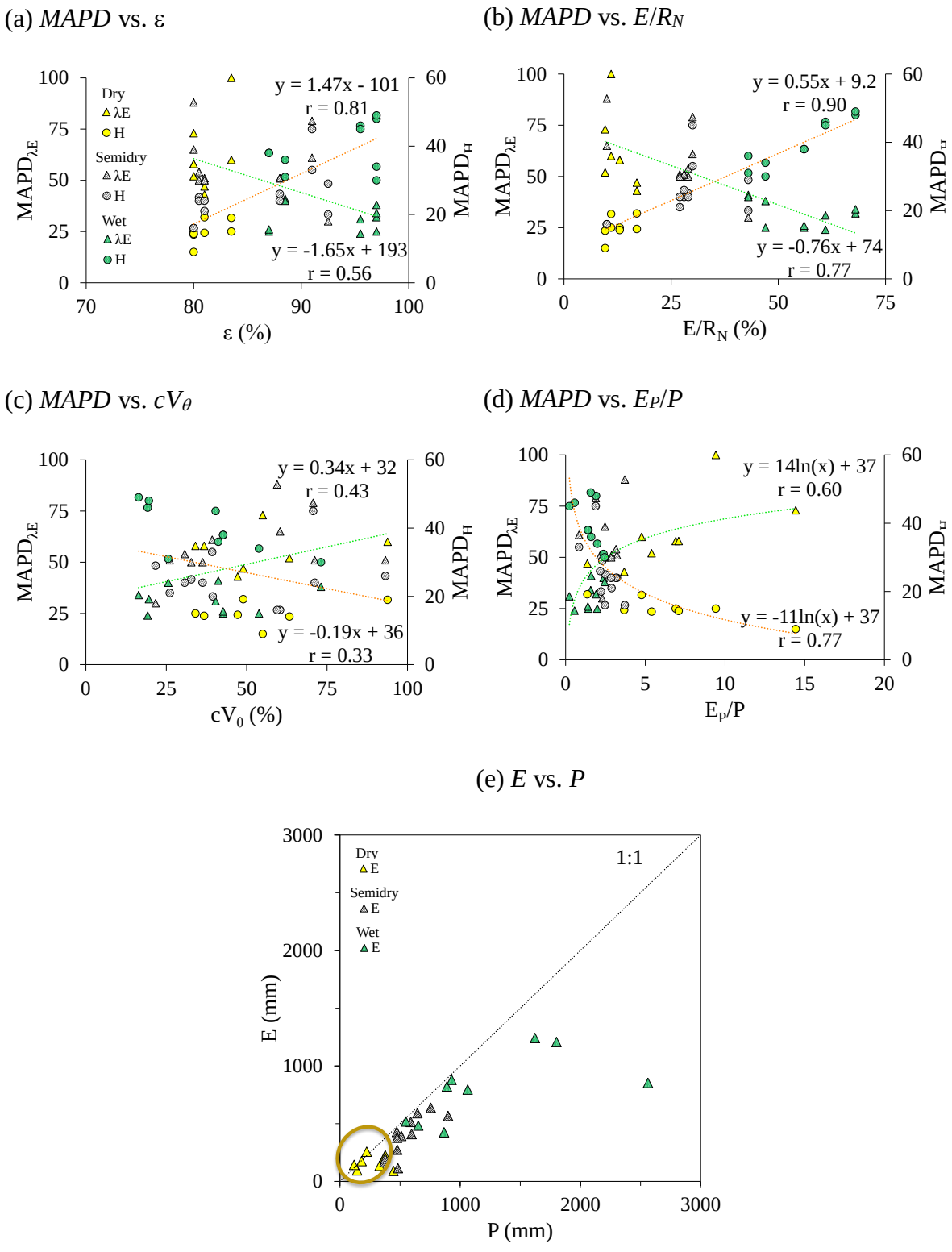

Figure 17 Scatters between *MAPD* in daily *E* and *H* versus ecohydrological and land surface variables (emissivity *ε* (a), evaporative index E/R_N (b), the coefficient of variation of *θ* (cV_θ) (c) and Budyko climatic dryness index E_p/P (d)) when data from three contrasting Australian ecosystem groups are combined. *y* represents the dependent variable, *x* the independent variable, and *r* the correlation coefficient. (e) A scatter plot between STIC1.2 derived annual *E* versus annual *P* (precipitation).

The scatter plots of monthly variances in predicted versus observed λE and H ($\sigma^2_{\lambda E}$ and σ^2_H) revealed the capacity of STIC1.2 to explain 88–90% of the observed flux variances for all ecohydrological conditions (Figure 18). The correlation matrix of the residual variance in the fluxes ($\Delta\sigma^2_{\lambda E} = \sigma^2_{\lambda E\ STIC1.2} - \sigma^2_{\lambda E\ observed}$ and $\Delta\sigma^2_H = \sigma^2_{H\ STIC1.2} - \sigma^2_{H\ observed}$) against a host of ecohydrological and meteorological variables revealed the absence of any strong systematic relationship between $\Delta\sigma^2_{\lambda E}$ versus for instance $\sigma^2_{T_R}$, σ^2_θ, σ^2_P and σ^2_u ($r = \pm 0.2$) (Figure 19a). For H, the similar analysis revealed 20–40% correlation between $\Delta\sigma^2_H$ and $\sigma^2_{T_R}$ and $\sigma^2_{T_A}$, but no strong relationship against other variables was found (Figure 19b).

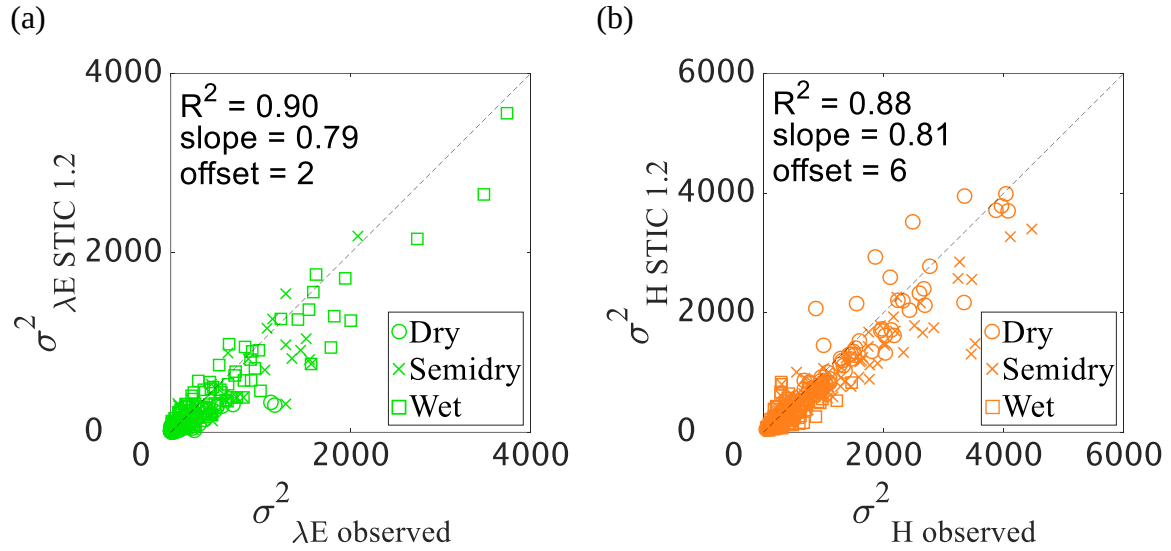

Figure 18 Scatters of monthly variance of STIC1.2 versus observed (a) λE ($\sigma^2_{\lambda E}$) and (b) H (σ^2_H) in three ecohydrologically contrasting Australian ecosystem groups (dry, semi-dry and wet).

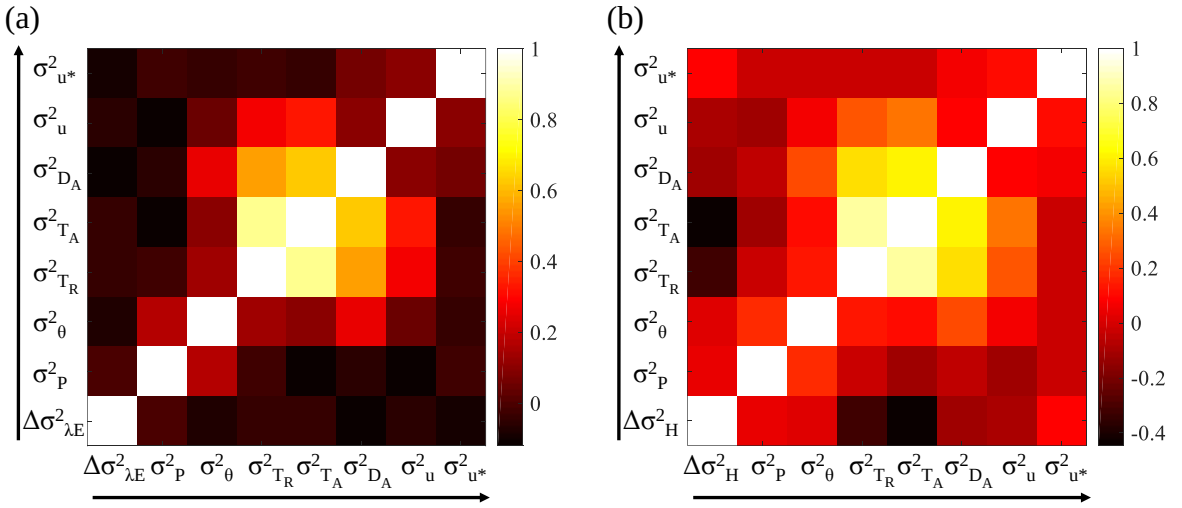

Figure 19 Correlation matrices showing the relationship between the residual variances in λE (a, $\Delta\sigma^2_{\lambda E} = \sigma^2_{\lambda E\ STIC1.2} - \sigma^2_{\lambda E\ observed}$) and H (b, $\Delta\sigma^2_H = \sigma^2_{H\ STIC1.2} - \sigma^2_{H\ observed}$) versus ecohydrological and meteorological variables.

5.2 Model comparison using MODIS data

5.2.1 Evaluating 8-day SEB fluxes

Estimates of λE and H from STIC1.2, PT-JPL and MOD16 at 8-day temporal resolution are compared to the EC flux observations at 5 sites (AU-ASM, AU-Dry, AU-How, AU-Stp and AU-Tum). The error statistics (R^2, *MAPD*, *RMSD* and $RMSDs^2/RMSD^2$) of each model are detailed in Table A7 in Appendix 2. Figure 20 is showing R^2, *MAPD* and *RMSD* values of each model when statistics are calculated based on the results from all sites. For λE, STIC1.2 was performing the best of the three models: it has the lowest errors (*RMSD* 86 W m^{-2}, *MAPD* 31%) and the best agreement between observed and modelled values (R^2 0.59) (Figure 20a). PT-JPL was found to be the second best for λE estimation with a slight underestimation and R^2 of 0.48, *RMSD* 102 W m^{-2} and *MAPD* 41% (Figure 20b). MOD16 model had the poorest performance for λE mainly due to overestimation (R^2 0.0, *RMSD* 259 W m^{-2} and *MAPD* 100%, see Figure 20d). The average $RMSDs^2/RMSD^2$ of λE were 23% for STIC1.2, 60% for PT-JPL and 86% for MOD16.

(a) Dry

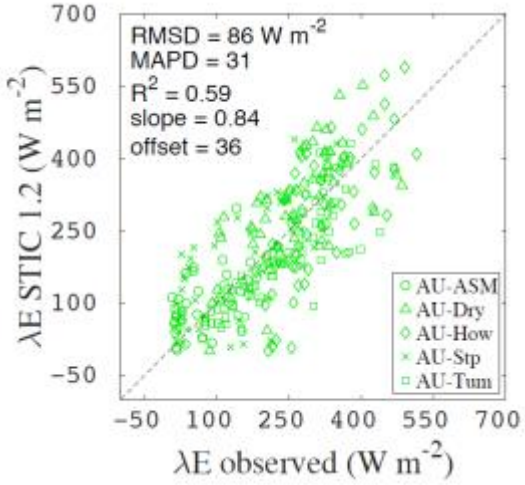

(b) Semi-dry

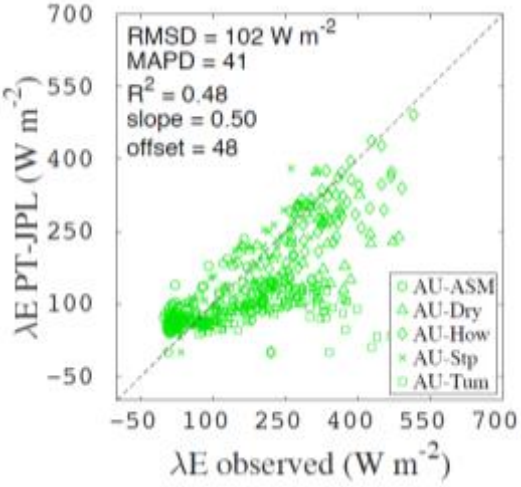

(c) Wet

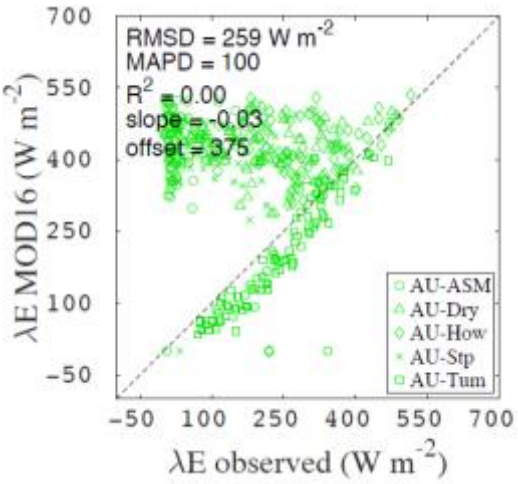

Figure 20 Comparison of STIC1.2, PT-JPL and MOD16 predicted 8-day λE with the measured latent heat flux component within the north Australian tropical transect NATT (AU-ASM, AU-Dry, AU-How, AU-Stp) and Au-Tum in dry (a), semi-dry (b) and wet (c) ecosystems.

Figure 21 shows the results for *H*. When comparing the performance of models, the PT-JPL model has the highest R^2 value of 0.48, the lowest *MAPD* of 29% and the second lowest *RMSD* of 102 W m^{-2}. These results were similar for STIC1.2 model, which has R^2 of 0.43, *MAPD* 33% and the lowest *RMSD* of 86 W m^{-2}. Similar to the modelling of λE, MOD16 performed the poorest for *H* estimation with 0.08 R^2, 100% *MAPD* and 259 W m^{-2} *RMSD*. The poor agreement for *H* estimation in MOD16 model was mainly due to underestimation of modelled *H*. The average $RMSD_S^2/RMSD^2$ of *H* were similar to the values for λE (24% for STIC1.2, 50% for PT-JPL and 88% for MOD16).

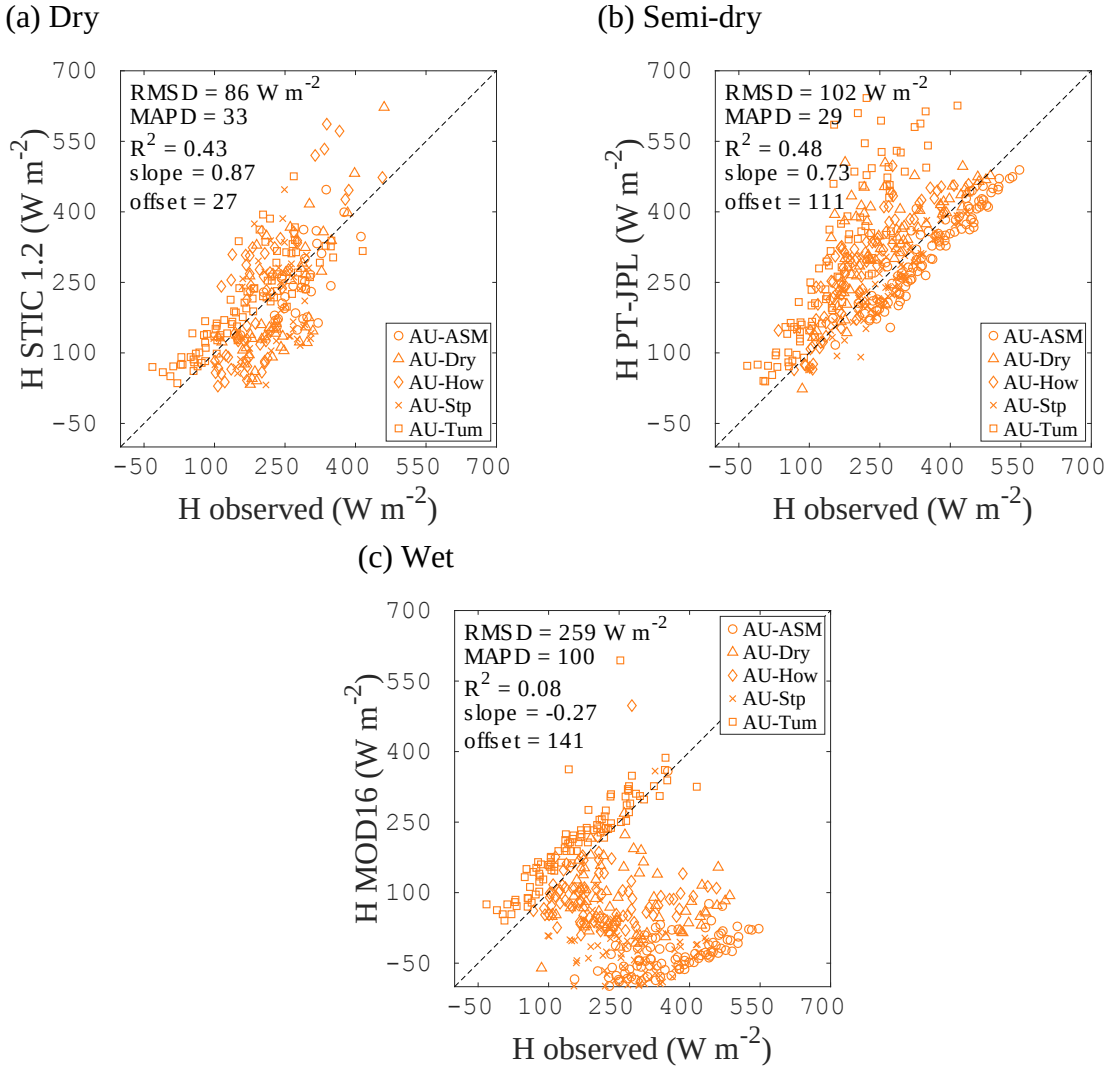

Figure 21 Comparison of STIC1.2, PT-JPL and MOD16 predicted 8-day *H* with measured sensible heat flux component within the north Australian tropical transect NATT (AU-ASM, AU-Dry, AU-How, AU-Stp) and Au-Tum in dry (a), semi-dry (b) and wet (c) ecosystems.

The performance of STIC1.2, PT-JPL and MOD16 to estimate SEB fluxes in separate sites is compared by Taylor diagrams (Figure 22). Figure 22a reveals how the performance of MOD16 for λE is poor for all the sites (correlation coefficient *r* 0–0.01 and $RMSD_N$ 100%) except for AU-Tum (*r* of 0.89 and $RMSD_N$ of 61%). In STIC1.2 model, the errors for all the sites are rather high (68–100%) but *r* moderate (0.26–0.74). Also STIC1.2 is performing the best for AU-Tum. The PT-JPL is performing slightly better than STIC1.2 and MOD16 for all the other sites except AU-Tum: *r* is ranging between 0.61–0.8 and $RMSD_N$ 53–95% when AU-Tum (*r* of 0.14 and $RMSD_N$ of 100%) is excluded.

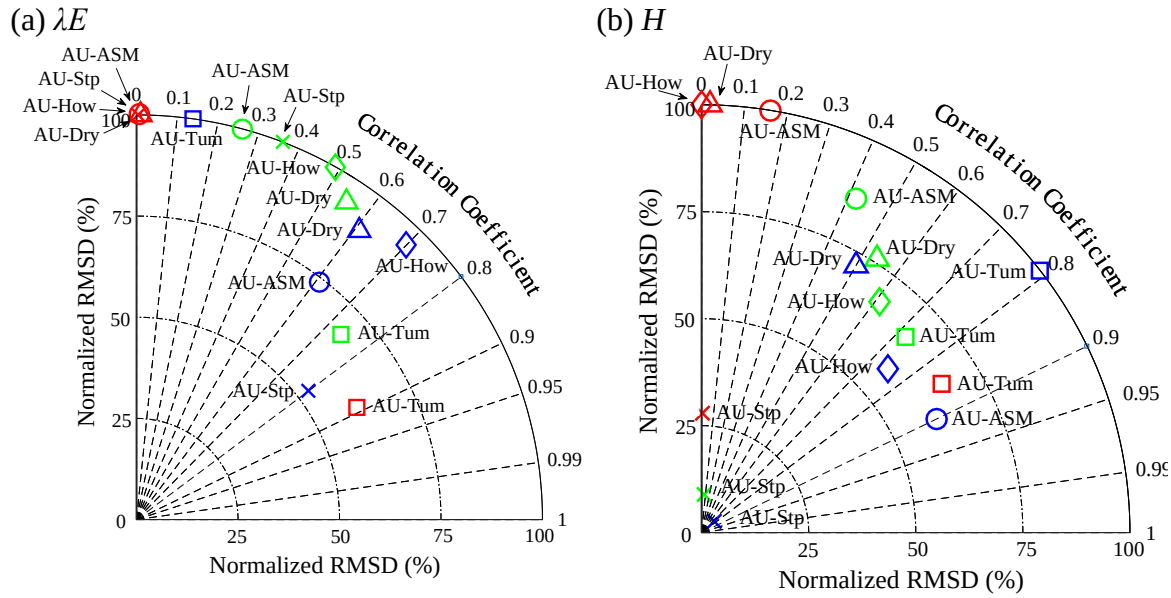

Figure 22 Taylor diagram of error statistics showing the $RMSD_N$ and correlation coefficient between observed and predicted λE (a) and H (b) of 2013–2014 in 5 Australian ecosystems. Green color is representing STIC1.2, blue PT-JPL and red MOD16 model.

The results for λE are similar to the modelling of H (Figure 22b). The correlation coefficient of MOD16 model for the sites excluding AU-Tum varies from 0 to 0.16 and $RMSD_N$ from 28 to 100%. MOD16 is performing its best at AU-Tum with r of 0.85 and $RMSD_N$ of 60%. However, the PT-JPL model has a better agreement between modelled and observed H than the MOD16 model at AU-Tum in two sites: at AU-Stp (r of 0.74 and $RMSD_N$ of 4%) and interestingly also at AU-ASM (r of 0.90 and $RMSD_N$ of 61%). For the other sites, r based on PT-JPL model results is ranging between 0.5–0.79 and $RMSD_N$ 57–100%. STIC1.2 is performing slightly poorer than PT-JPL with r varying from 0.07 (AU-ASM) to 0.72 (AU-Tum) and $RMSD_N$ from 9 (AU-Stp) to 86% (AU-ASM).

5.2.2 Error characterization

The correlation matrices of the residual in the latent heat flux ($\Delta\lambda E = \lambda E_{model} - \lambda E_{observed}$) versus several ecohydrological and meteorological variables for the STIC1.2, PT-JPL and MOD16 models are shown in Figure 23. Figure 23a shows that the correlations for STIC1.2 results are not very strong (r = -0.2–0.2). For PT-JPL (Figure 23b), these relationships are stronger (r = -0.5–0.5) especially between residuals and soil moisture, $NDVI$, T_R and D_A. Similar trend can be also detected for MOD16 (Figure 23c), which has the strongest correlations between the residuals and variables (r = -0.8–0.8). Correspondingly with the PT-JPL results, the relationships were the strongest for the residuals against soil moisture, $NDVI$, T_R and D_A.

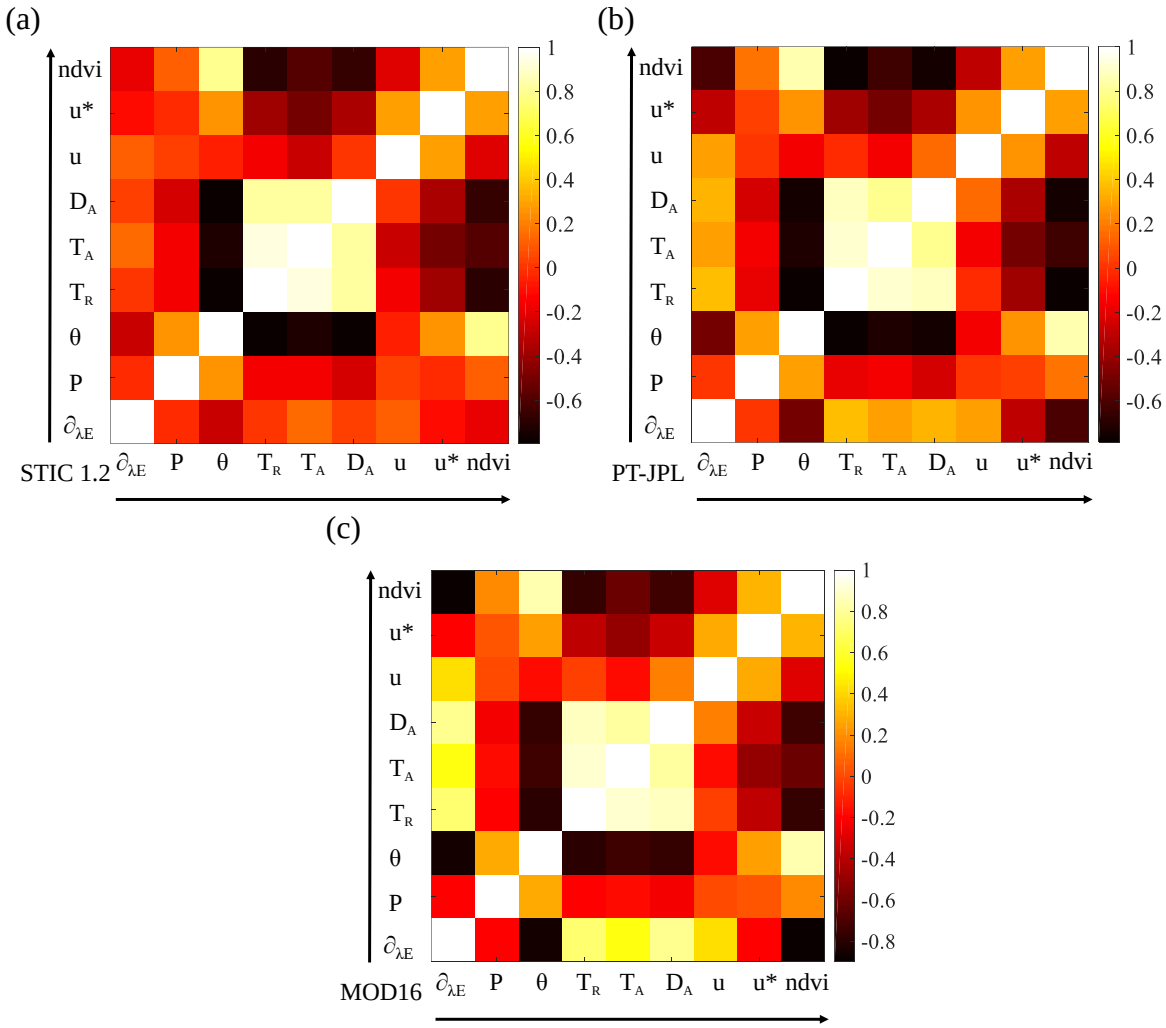

Figure 23 Correlation matrices showing the relationship between the residual in λE ($\Delta\lambda E = \lambda E_{model} - \lambda E_{observed}$) versus ecohydrological and meteorological variables in STIC1.2 (a), PT-JPL (b) and MOD16 (c) models.

Figure 24 shows the correlation matrices of the residuals in the sensible heat flux ($\Delta H = H_{model} - H_{observed}$) against different ecohydrological and meteorological variables for the STIC1.2, PT-JPL and MOD16 models. Similarly to the latent heat flux, STIC1.2 model is not showing any strong correlation between the residuals and variables (r = -0.1–0.2). However, for both PT-JPL and MOD16 models the correlations are stronger varying between -0.3–0.6 and -0.8–0.9, respectively. The strongest relationships are between the residuals and soil moisture and *NDVI* in PT-JPL model and between the residuals and soil moisture, *NDVI*, T_R and D_A in MOD16.

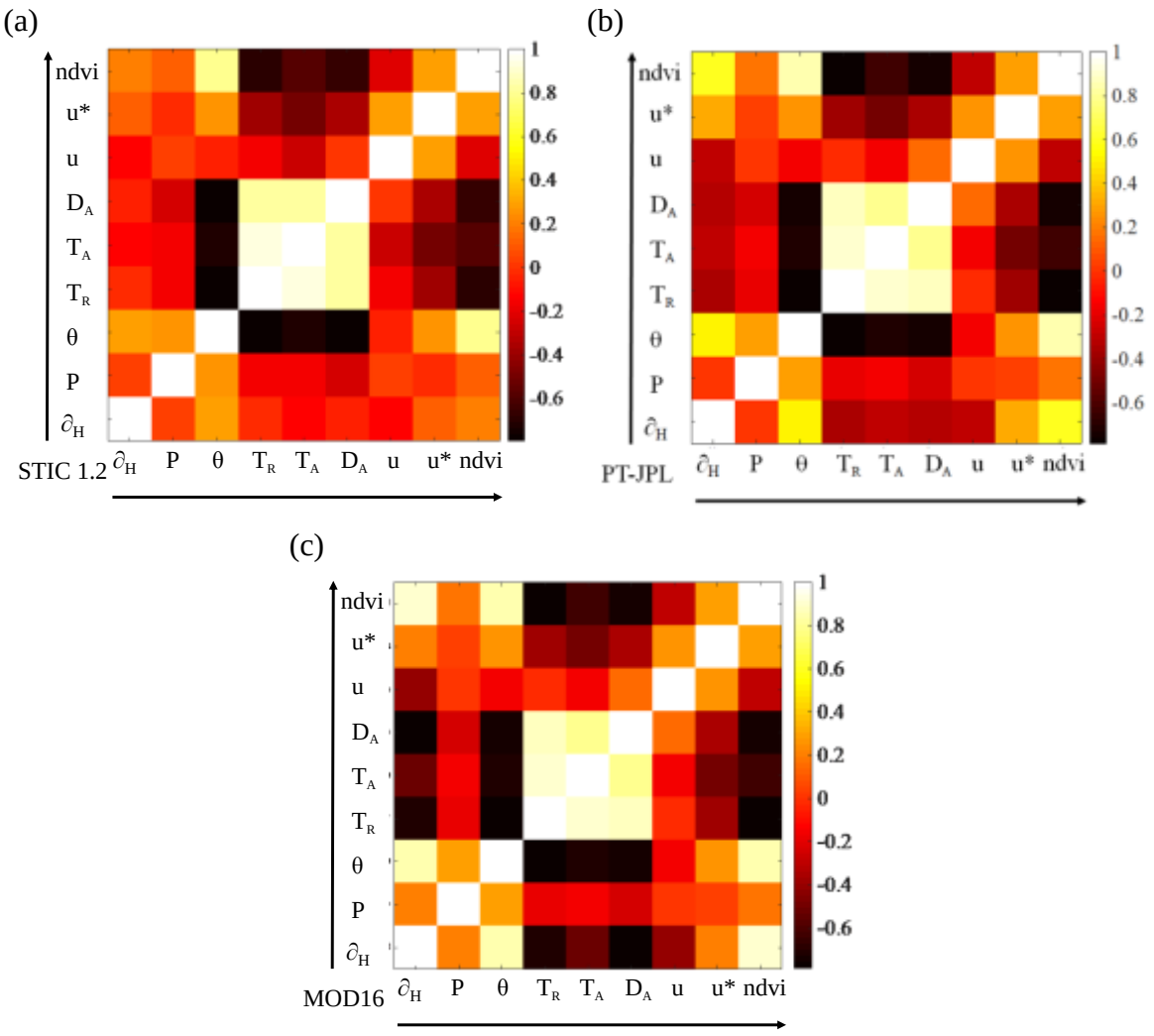

Figure 24 Correlation matrices showing the relationship between the residual in *H* (*ΔH* = H_{model}–$H_{observed}$) versus ecohydrological and meteorological variables in STIC1.2 (a), PT-JPL (b) and MOD16 (c) models.

6 Discussion

6.1 Evaluating multi-temporal SEB fluxes

Evaluation of half-hourly surface fluxes modelled with STIC1.2 at 15 Ozflux sites with different ecohydrological characteristics showed larger differences between predicted and observed λE for the dry ecosystems (0.36 R^2, 61% *MAPD*, 52% $RMSD_S^2/RMSD^2$) compared to the semi-dry and wet ecosystems (0.54–0.85 R^2, 32–55% *MAPD*, 13–37% $RMSD_S^2/RMSD^2$). However, *RMSD* values were smaller for the dry sites (37 W m^{-2}) than for the semi-dry and wet sites (50–53 W m^{-2}). This is due to smaller volume of λE fluxes at dry sites, which makes the absolute *RMSD* values smaller compared to the *RMSD* at semi-dry or wet sites. For estimation of *H*, the pattern was opposite to λE: the best agreement between modelled and observed values were detected at dry sites (0.96 R^2, 15% *MAPD*). In addition, STIC1.2 performed well over the semi-dry and wet sites (0.84–0.91 R^2, 25–40% *MAPD*). As opposed to λE modelling, the average ratio of $RMSD_S^2/RMSD^2$ for *H* varied between 19–23%. However, the absolute errors were in the same range than for λE: at dry sites *RMSD* was 33 W m^{-2} and 50–53 W m^{-2} at semi-dry and wet sites. In general, STIC1.2 showed less difference in the results of *H* for each ecological group compared to the results of λE. Also systematic errors were smaller, and the rate of $RMSD_S^2/RMSD^2$ did not significantly vary between the sites. However, the overall performance of STIC1.2 is comparable for instance with the study of Kalma et al. (2008), who revealed the *RMSD* of approximately 50 W m^{-2} and relative errors of 15–30% when analysing the results of 30 different validations of SEB flux models.

Mallick et al. (2015) reported the earlier version of STIC (STIC1.1) to perform rather well when testing the model performance over 30 different EC towers, which represented agroecosystems (humid and dry semi-arid sites), grassland (temperate) and woody savanna and shrublands (dry semi-arid). For λE (and *H*), the average performance over all sites revealed R^2 of 0.94 (0.87), *RMSD* 43 W m^{-2} (42 W m^{-2}), *MAPD* 13% (42%) and $RMSD_S^2/RMSD^2$ 14% (13%). The earlier study of STIC1.2 performance over Amazon (Mallick et al., 2016) showed similar results when 6 EC towers over sites located in tropical rainforest, tropical moist forest, tropical dry forest and pasture were used. These Amazon sites received over 1500 mm precipitation annually. The study resulted in the average R^2 of 0.94 (λE) and 0.61 (*H*) and *RMSD* of 33 W m^{-2} (λE) and 37 W m^{-2} (*H*). The main difference between these results is the performance of *H*: in the study over Amazon, the *H* component is rather small compared to λE, which might have resulted in poorer R^2, but still smaller *RMSD* values. In the current analysis performed in this study, the average results at sub-daily scale were 0.59 and 0.90 R^2, 48 W m^{-2} and 46 W m^{-2} *RMSD*, 49% and 27% *MAPD* and 46% and 22% $RMSD_S^2/RMSD^2$ for λE and *H*, respectively. Thus, the model performance was similar, but slightly poorer compared to the two earlier studies. This might be due to the higher amount of the dry and semi-dry sites included in this study.

Venturini et al. (2013) presented model results of λE over different climate zones. They used MOD16 and Operational Simplified Surface Energy Balance (SSEBop) models and validated these using EC FLUXNET data at monthly scale (2001–2007) over 60 different sites in the United States. They reported R^2 of 0.26 (MOD16) and 0.55 (SSEBop) over climate type of BSk. *RMSD* values were reported at monthly scale, but if they are scaled at daily scale (by dividing by 30), the obtained *RMSD* values were 22 W m^{-2} for MOD16 and 18 W m^{-2} for SSEBop. Over the climate type of Cfa, the reported values were 0.58 and 0.67 for R^2 and 30 W m^{-2} and 28 W m^{-2} for *RMSD* for MOD16 and SSEBop, respectively. The

Csa results were similar to Cfa with R^2 of 0.63 (MOD16) and 0.65 (SSEBop) and *RMSD* of 24 W m^{-2} (MOD16) and 18 W m^{-2} (SSEBop). In the current STIC1.2 performance analysis, the obtained results at sub-daily scale were R^2 of 0.17, 0.55 and 0.79 and *RMSD* of 33, 54 and 52 at AU-Cpr (representing BSk), AU-Gin (representing Csa) and AU-Cum (representing Cfa), respectively. Thus, these current results show similar pattern to the study of Venturini et al. (2013): R^2 is the poorest, but *RMSD* values the smallest for BSk sites. Also model performance increased in the sites with Csa and Cfa climate types. However, the differences in the results of this study compared to the study of Venturini et al. (2013) might be due to different validation sites, different models as well as different time scales.

The average errors obtained in this study were diminished with increasing temporal frequency (at daily and annual scales). For instance, sub-daily λE estimations had an average R^2 of 0.59, which increased into 0.67 at daily scale and 0.97 at annual scale. Also *MAPD* values decreased from 49% (sub-daily) to 38% (daily) and 10% (annual). *RMSD* values were 48 W m^{-2} and 15 W m^{-2} at sub-daily and daily scale, respectively. When annual *RMSD* value is transformed into daily scale (by dividing by 365), *RMSD* value is even lower, approximately 5 W m^{-2}. In addition, the results for H were similar: *MAPD* values were decreasing (27%, 24% and 10% at sub-daily, daily and annual scales, respectively). The calculated *RMSD* values for H were 46 W m^{-2} at sub-daily scale and 17 W m^{-2} at daily scale. Annual *RMSD* value for H was converted into daily scale in the same way as for λE, leading to the *RMSD* of approximately 7 W m^{-2}. However, the R^2 value at daily scale (0.84) was slightly poorer compared to the sub-daily value of 0.90. At annual scale, R^2 was the highest, 0.93. Similar results have been obtained by Polhamus et al. (2014), who reported an increase of 0.15 in the model's R^2 (used models MOD16 and PT-JPL) when estimating λE at monthly scale instead of daily values. They suggested this to be due to averaging of random variation and errors. Also Velpuri et al. (2013) noted that the uncertainty is reduced further at annual λE estimates compared to monthly values.

As discussed earlier, STIC1.2 was not capable to reliably capture the exceptionally low daily λE values in the sites with annual mean precipitation lower than 350 mm (AU-ASM, AU-Cpr, AU-GWW, AU-TTE), particularly when mean daily λE was close to zero (Figure 11a). These differences may be partly attributed to the inherent uncertainties in the EC λE observations (Masseroni et al., 2014), the noise associated with the low magnitude of λE, and failure of the EC systems to capture advective λE in arid to semi-arid ecosystems (Alfieri et al., 2012). However, the differences between predicted and observed λE values arising from the fundamental uncertainty of the T_R retrieval technique, particularly the definition of the thermal infrared emissivity (ε), are even more important in the water-limited ecosystems.

SEB flux estimates in the current modelling framework are strongly dependent on T_R because it is used to estimate the surface moisture availability (M) and M is one of the core state variables that constrain the two biophysical conductances in STIC1.2. When STIC1.2 was validated using only OzFlux data, retrieval of T_R was based on the $R_{L\uparrow}$ observations and the Stefan-Boltzmann law, and a single value of emissivity was assigned for every individual site. Since ε appears in the denominator in T_R retrieval equation, the obtained T_R is sensitive to uncertainties in ε (Hulley et al., 2012). The sensitivity analysis of STIC framework to T_R (Mallick et al., 2014, 2015) already revealed the sensitivity of g_A and g_C being in the order of 14–30% and 19–36% due to 0.78–0.82 K T_R uncertainties. Underestimation (or overestimation) of T_R would lead to overestimation (or underestimation) of M, which further leads to underestimation (or overestimation) of the g_A/g_C ratio in the denominator of the PM

model, and the resultant SEB flux estimations become uncertain. Therefore, careful handling of infrared ε data is essential for deriving accurate and reliable surface temperature over land (Li et al., 2007; Hulley et al., 2012). In the present study, information on the diurnal variability of ε was unavailable. Although the variations in ε over dense vegetation is not significant, but substantial diurnal variability in ε is expected to occur especially in the sparsely vegetated ecosystems due to the influence of the soil moisture (θ) on ε (Masiello et al., 2014). In the arid and semi-arid environments, a direct water vapor adsorption on the soil leads to diurnal variation of θ between midday and sunrise (Agam and Berliner, 2006), thus leading a diurnal variation of ε. For low soil water content values, the rate of change of ε per unit change of θ (i.e., $\partial\varepsilon/\partial\theta$), at wave numbers of reststrahlen absorption is considerably large; $\partial\varepsilon \approx 0.05$ per change in θ of 0.01 kg kg^{-1} (Masiello et al., 2014). Besides, substantial diurnal variability of ε can also be found during the absence of rainfall due to dew condensation at night (Masiello et al., 2014). Consequently, excluding the sub-daily variability of ε in the T_R estimation affects the obtained results and results in increasing uncertainty. This is evident also in the *MAPD* vs. ε scatter plot (Figure 17a).

It is essential to note that direct water adsorption on the land surface occurs when water vapor is transported due to advection (Agam and Berliner, 2004). One of the theoretical assumptions of the EC technique is based on neglecting advection, which will automatically tend to lead in disagreement between $\lambda E_{\text{STIC1.2}}$ and $\lambda E_{\text{observed}}$ under these specific conditions. The significantly lower errors of predicted H values might be the result of compensation due to partial elimination of the conductance errors in the PM formulation of H (Equation 7). This is specifically applicable for the dry and semi-dry ecosystems, because g_C is more sensitive to uncertainties in T_R when compared to g_A (Mallick et al., 2015). Due to the low fractional vegetation cover in the dry, semi-dry woodlands and savannas, T_R is very close to T_0, and thus estimation of g_A (Equation 9) in STIC1.2 becomes less sensitive to uncertainties related to T_0 (and the canopy source-sink height), which might have been one reason for observing a good agreement between the observed and predicted H. In contrast, the relatively higher uncertainty in g_C (due to T_R) for λE estimates might have introduced higher error in g_A/g_C in the denominator of Equation 6 (see also Mallick et al., 2015), thus causing larger disagreement for λE in the dry and semi-dry ecosystems. For the same reversed reasons, the wet ecosystems have experienced low predictive errors in λE.

Although the used Bowen ratio correction (see Appendix) forces the SEB closure, in the arid and semi-arid ecosystems major corrections are generally seen in H. Thus, λE is negligibly corrected. (Chávez et al., 2005.) In addition, Chávez et al. (2005) noted that the uncertainty in ground-based G estimations results in poorer SEB flux correction. Also, as stated by Masseroni et al. (2014), half-hourly averaging periods are not sufficiently large for taking into account all temporal-scale terms in λE flux measurements by the EC method. As mentioned earlier, based on Glenn et al. (2011) EC method include 10–30% of uncertainty in SEB flux estimation. When taking into account the model's own uncertainty, the modelled and observed values cannot be fully identical (Velpuri et al., 2013). However, substantially low predictive errors of H from half-hourly to annual scales indicate the credibility of surface flux estimates within STIC1.2 modelling framework. Assuming that the differences between predicted and observed H in the dry and semi-dry ecosystems primarily originate from the uncertainties of ε (T_R), a dynamic characterization of ε will further improve H predictions in the water-controlled ecosystems. Again, expecting that the predictive λE errors in the dry and semi-dry ecosystems are originated from the uncertainties of ε (T_R) and underestimation of EC observed λE, a robust surface energy balance closure method (along with the

improvements in the characterization of ε) will significantly reduce the anomalies between predicted versus observed λE fluxes especially in water-controlled ecosystems.

6.2 Ecohydrological sensitivity of SEB fluxes

The Taylor diagram (Figure 16) comparing the errors for the dry and wet season further highlights the predominant ecohydrological controls on the SEB flux evaluation statistics. Although there is a direct response of soil moisture to precipitation in the dry and semi-dry regions, the feedback of soil moisture and precipitation to λE is rather weak and lagged (Dirmeyer, 2011). The relationship between soil moisture and evaporative fraction is nonlinear due to transpiration, and is one reason for a relatively weak sensitivity of E to P during the dry season (Williams and Torn, 2015), as found in the current analysis. For instance, Meyer at al. (2015) state that E rates during the dry season are not significantly changing compared to the wet seasons due to the use of water storage from previous wetter periods, and that plants are responding to limited water availability mainly by leaf area changes. However, a high sensitivity between E and P during the wet season in the dry and semi-dry ecosystems indicates the predominant soil moisture control on E, which is effectively captured by STIC1.2. In the water-limited ecosystems, ϕ is predominantly partitioned into H (García et al., 2008; see also Figure 15a), and soil moisture content (and rainfall) has an impact on this non-evaporative flux component (Dirmeyer, 2011). This became evident in the high sensitivity of H to P (as compared to $S_{E,P}$) in the dry and semi-dry ecosystems (Table 5). Considering H to be the dominant non-evaporative SEB flux in water-limited landscapes (García et al., 2008), the performance of STIC1.2 to capture 76%–95% of the observed H variability over the dry and semi-dry ecosystems with normalized *RMSD* ranging between 28%–63% (Figure 16) shows the potential of this modelling framework to reliably capture sensible heat fluxes. Similarly, the capacity of STIC1.2 to predict 70%–76% of daily λE variability in the semi-dry and wet ecosystems (Figure 16b) also demonstrates its potential for the use in the applications of water management across managed and natural ecosystems with annual P above 350 mm.

Higher E rates in the wet ecosystem (AU-Cow) during the dry season (June–October) than during the wet season (January–May and November–December) (Figure 15c) suggests that soil water availability did not become limiting during the dry season, and these ecosystems sustain high E under dry weather conditions (O'Grady et al., 1999). The sensitivity and correlation analysis of seasonal E to seasonal P and ϕ in the three ecohydrologically diverse ecosystems (Table 5) revealed that the seasonal E in the wet ecosystems is generally limited by the available energy, rather than by water (E is insensitive to P, Table 5). This causes the wet season E to be lower during periods with abnormally large precipitation and to increase in the drier years because E in January to June was limited by ϕ (presumably due to cloudiness). Generally, higher E during the dry season than during the wet season is due to a large evaporative demand and exploitation of soil moisture and groundwater storages by the vegetation (O'Grady et al., 1999; Decker et al., 2013). In drier ecosystems, the sensitivity of STIC1.2 modelled E and H to the variability in P further shows the capability of this T_R-driven physically-based modelling framework in capturing the water induced SEB flux sensitivities in these water-controlled ecosystems. Also, high $S_{H,P}$ for both observations and STIC1.2 estimates in the dry and semi-dry ecosystems indicates direct ecohydrological coupling between P and H in the water-limited ecosystems.

6.3 Ecohydrological controls on error characterization

Understanding the critical role of T_R in the PM-SW based STIC1.2 modelling framework, it is again apparent that the primary source of absolute errors in λE and H at individual study sites originate from uncertainties in T_R (from the assumption of constant ε values) (Figure 17a). This uncertainty is consequently propagated into the *MAPD* versus cV_θ, annual E/R_N, and E_P/P relationships (Figures 17b–d). In the dry ecosystem, frequent variations in ε associated with soil moisture can be expected (Hulley et al., 2010) as discussed before. Thus, assuming a constant ε led to high errors in SEB flux predictions (Figure 17a). Low annual E/R_N and high annual E_P/P are the indicators of water-stressed ecosystems, where low E is the result of low P and θ despite a high amount of available energy in conjunction with a high evaporative potential (i.e., vapor pressure deficit). This kind of ecohydrological stress imposes integrated soil water and atmospheric controls on E (Jarvis and McNaughton, 1986), and enhances also biophysical controls (i.e. g_C and g_A) on E (Mallick et al., 2016). Since our g_C estimates are constrained by T_R (through M), the improvements in the accuracy of T_R is one of the key factors to improve E retrievals especially under water-limited ecosystems. The ecohydrological perspective on error characterization also indicated that in the ecosystems with low annual evaporative index (E/R_N) and very high climatic dryness index (E_P/P), sensible heat flux is dominant and should be given more emphasis to evaluate the performance of the models rather than using λE. An assessment of annual E (from STIC1.2) against annual P (Figure 17e) further showed that the quantity of E is very close to P in the dry ecosystems, and that E becomes less sensitive to P when P exceeds 500 mm.

Despite the occurrence of absolute differences between observed and predicted SEB fluxes, very close correspondence between the flux variances (Figure 18) provides convincing evidence on the absence of any systematic bias in the STIC1.2 modelling scheme and indicates the ability of this model to capture both radiation-limited as well as water-limited variability from both wet to very dry surface conditions. The evidence of ±12–15% correlation between $\Delta\sigma^2_{\lambda E}$ ($\sigma^2_{\lambda E\ STIC1.2} - \sigma^2_{\lambda E\ observed}$) and σ^2_θ, σ^2_P as well as $\sigma^2_{T_R}$ (Figure 19a) might be a result of the assumption of constant value of ε, but may also be related to the uncertainties of λE observations using the EC method under the dry and semi-dry environments. Besides, the negative relationship (r = -0.20) between $\Delta\sigma^2_{\lambda E}$ and σ^2_{u*} can be associated with the errors in EC observations under atmospheric conditions with very low turbulence. A nearly zero correlation between $\Delta\sigma^2_H$ with ecohydrological variances further indicates that H was predominant in water-limited regions, and sensible heat flux consequently affects the boundary layer growth (Koster et al., 2015). This became also evident from the 40% correlation between $\Delta\sigma^2_H$ and $\sigma^2_{T_A}$. Also the absence of relationships between $\Delta\sigma^2_H$ and σ^2_u as well as $\Delta\sigma^2_{\lambda E}$ and σ^2_u strengthens the assumption that excluding wind speed from STIC1.2 modelling framework does not affect the obtained SEB flux estimates.

6.4 Comparison of SEB models

The results of this study shows that STIC1.2 performs the best for λE estimates at 8-day scale (8-day average of λE at noon) with R^2 of 0.59 over the 5 selected OzFlux sites when data is retrieved from MODIS products over the years 2013 and 2014. STIC1.2 had also the lowest predictive errors (*RMSD* 86 W m^{-2}, *MAPD* 31%) among the SEB models selected for this study (PT-JPL and MOD16). These results were similar compared to the error statistics over 15 OzFlux sites (where T_R was retrieved from the OzFlux dataset), which revealed R^2 of 0.59, *MAPD* 49% and *RMSD* 48 W m^{-2} at sub-daily scale as shown before. Thus, the main

difference is detected in absolute errors, which are higher in case of MODIS retrieved T_R as an input of STIC1.2 model. However, the statistics of PT-JPL show similar results with R^2 of 0.48, *MAPD* 41% and *RMSD* 102 W m^{-2}. In contrast, MOD16 model for λE estimations shows the lack of relationship between modelled and observed values (R^2 of 0.00) and very high predictive errors (*MAPD* 100%, *RMSD* 259 W m^{-2}). For sensible heat flux estimates, PT-JPL appears to show slightly better statistics (R^2 of 0.48, *MAPD* 29%) compared to STIC1.2, which has R^2 of 0.43 and *MAPD* around 33%. However, absolute errors are higher for PT-JPL model (values of *RMSD* similar than for λE). MOD16 model performance stays poor, but R^2 value increases to 0.08. For both SEB flux estimations, the systematic error ($RMSD_S^2/RMSD^2$) was found to be smallest for STIC1.2 (23–24%) and the highest in MO16 (86–88%). It is important to notice, that these discrepancies can originate also from the use of different MODIS products. The MODIS T_R data is proven to have an average accuracy of 0.5 K, but higher errors in dry and arid regions because of the higher uncertainty in ε (as mentioned before) as well as the effects of heavy dust aerosols (NASA, 2016d). PT-JPL and MOD16 are using MODIS surface spectral reflectance data (MOD09), which has an overall uncertainty around 5–9% (clear sky to high aerosol load) (Miura et al. 2008).

For example, Polhamus et al. (2013) tested the performance of PT-JPL and MOD16 models over 42 AmeriFlux sites to estimate λE by using MODIS data. Their study revealed R^2 of 0.73 and 0.48 and *RMSD* of 37 and 44 W m^{-2} for PT-JPL and MOD16, respectively. Thus, their study showed better overall performance of the models than the analysis in this study. However, PT-JPL performed better than MOD16 in both studies. Also Vinukollu (2011) performed similar study over 12 EC towers in the USA using Surface Energy Balance System (SEBS), Penman-Monteith algorithm (PM-Mu, earlier version of MOD16) and PT-JPL models. Similar to Polhamus et al. (2013), Vinukollu et al. (2011) found the performance of PT-JPL model to be superior over SEBS and PM-Mu models for λE estimates. More recently, Ershadi et al. (2014) concluded that the PT-JPL model was found to perform better compared to SEBS, single-source Penman-Monteith (PM) and advection-aridity (AA) methods over 20 FLUXNET sites. However, the performance of energy balance approach (SEBS) was found to be close to PT-JPL, and in contrast, PM model showed overall low performance. They argued this to be due to the uncertainties related to the parameterization of PM model (i.e. resistances). Therefore, these earlier studies showed similar overall results to the current analysis made by comparing STIC1.2, PT-JPL and MOD16 models: based on the Taylor diagrams, PT-JPL produced the most robust estimates of both SEB fluxes excluding AU-Tum (Figure 22). However, the results showed that the performance of STIC1.2 was still superior over MOD16. Despite MOD16 is showing overall low performance in this study, Taylor diagram analysis over all sites revealed the performance of MOD16 to be the best of the three models over AU-Tum. Overall, the H estimates evaluated by Taylor diagrams are associated with lower predictive errors.

The evaluation of correlation matrices of λE and H (Figures 23, 24) indicate the lack of any strong relationship between $\Delta\lambda E/H_{STIC1.2}$ ($\lambda E/H_{STIC1.2}$–$\lambda E/H_{observed}$) and the tested ecohydrological and meteorological variables (P, θ, T_R, T_A, D_A, u, u^* and *NDVI*). However, the slight correlation can be found between $\Delta\lambda E_{STIC1.2}$ and θ, T_A or u (r = -0.3–0.3) and $\Delta H_{STIC1.2}$ and θ, u^* and *NDVI* (r = 0.1–0.35). However, the strongest relationships are detected between SEB flux anomalies and soil moisture (-0.3 for λE and 0.35 for H), which can again be linked with the quality of T_R observations. In addition, the links between the differences in observed and modelled fluxes and *NDVI* can be related to the use of two semi-arid sites (AU-ASM and AU-Stp) and two tropical savanna sites with dry winter (AU-Dry

and AU-How) in the analysis: as *NDVI* is a measure of the density of green (Weier and Herring, 2000), most likely these sites have low *NDVI* values indicating water-limitation. As shown earlier, STIC1.2 is not robust over very dry conditions mainly due to the sensitivity of the model to uncertainties in T_R. However, the correlation matrices of λE and H for PT-JPL revealed stronger relationships (r = -0.5–0.6) between anomalies in SEB flux estimations and θ, *NDVI*, T_R and D_A. Further evaluation of correlations in the MOD16 model showed even higher relationships (-0.8–0.9) over the same variables as for PT-JPL.

Based on the obtained results, PT-JPL and MOD16 models showed significant sensitivity over θ as well as *NDVI*, which is also one of the main inputs of both models. Also Fisher et al. (2008) remarked the PT-JPL model sensitivity to *NDVI* as it is one main variables to determine the partitioning of R_N into R_{Ns} and R_{Nc}. However, they concluded that the primary source of uncertainty in PT-JPL model is most likely associated with R_N, which was not evaluated in the analysis performed here. In addition, they argued that e_A is showing only minimal influence in the model. However, in this current study performed over Australia, the correlation between $\Delta\lambda E_{PT\text{-}JPL}$ and D_A which is calculated using e_A (calculated using *RH*), was still rather high (approximately 0.5). This can be explained due to the use of D_A as an input in T_{max} calculations. In addition, Polhamus et al. (2011) argued that one significant source of errors in PT-JPL is the uncertainty in energy balance closure. They also linked the MOD16 model errors with *LAI* (*NDVI* needed for calculation) and the magnitude of λE, and argued this approach to be too simplistic due to the broad assumptions on parameterization.

Also Mu et al. (2011) noted some limitations in the MOD16 algorithm due to the use of a large number of physical variables and site specific parameters, which are still being assigned globally. Especially they remarked that the accurate estimates of λE are hard to obtain under heterogeneous landscapes. However, although PT's formulation is less sophisticated compared to PM, it is easier to parameterize (Fisher et al., 2008), which might be one reason for a slightly smaller uncertainty in PT-JPL model estimates compared to MOD16. Kalma et al. (2008) also noted, that overall uncertainties related to empirical vegetation index models might be due to neglecting advection, and thus the use of these methods should be restricted to radiation-controlled regions (such as AU-Tum). It is also important to note, that the overall moderate performance of both STIC1.2 and PT-JPL (when MODIS data is used) can originate from the differences in the footprint of EC tower and MODIS satellite observations, which is making the validation challenging as also recognized by Vinukollu et al. (2011).

7 Conclusions

The STIC1.2 method particularly overcomes the uncertainties in T_0 estimates as well as the parameterization of biophysical conductances by integrating thermal surface temperature into a combined structure of the PM-SW model. It also establishes a direct feedback between T_R and the SEB flux estimates as opposite to PT-JPL and MOD16 models used in this study. The current analysis showed that this single-source box modelling framework STIC1.2 is capable to reliably capture the energy and water fluxes from hourly to annual scale across a broad spectrum of ecohydrologically diverse ecosystems in Australia. However, the STIC1.2 model estimates over the dry sites in Australia (annual $P < 350$ mm) showed poorer results compared to the semi-dry ($350 < P < 700$ mm) and wet (annual $P > 700$ mm) Australian sites. Interestingly, STIC1.2 showed less difference in the results of H for each ecological group (dry, semi-dry and wet) compared to the results of λE. The accuracy in the estimates of λE and H from STIC1.2 were comparable with PT-JPL, but STIC1.2 showed superior performance compared to MOD16. The STIC1.2 modelling framework is independent of any biome specific or leaf-scale empirical parameterization for the biophysical conductances as it does not require any data on vegetation, thus making it more robust compared to the parameterization depended MOD16.

Despite that thermal infrared data contains relevant information to capture the variability of λE and H under water-limited conditions, the performance of the T_R-driven modelling approaches is depending on more accurate surface emissivity corrections especially over dry landscapes with scarce vegetation cover. Since ε is highly variable in water-stressed ecosystems, the use of inverted T_R using $R_{L\uparrow}$ information is apparently not the optimal method to accurately estimate λE and H. Likewise, using MODIS based T_R data for λE and H estimations led to higher uncertainties especially over the dry sites. Thus, high quality T_R observations from infrared radiometers representing an appropriate footprint area around EC sites would be preferred for SEB flux validation. However, large scale applications of STIC1.2 would need more precise satellite-retrieved T_R data for robust performance over arid and semi-arid landscapes. However, a successful application of STIC1.2 and an improvement of the performance over water-stressed ecosystems can be expected with the availability of more accurate T_R retrieval techniques, e.g. from the recently launched Sentinel-3.

Thermal component of the SEB fluxes is predominant under dry water-controlled ecosystems. Therefore, H might be a favoured indicator of water stress and a better metric to test the skill of any physically-based model under these conditions. Simultaneously, in the semi-dry to wet and humid ecosystems, λE appears to be the better metric to evaluate model performance. This study showed a remarkable capability of STIC1.2 to capture the behavior of these two most important energy-water cycle variables across these ecohydrological extremes.

The modelling of individual water flux components (transpiration and evaporation) when using STIC1.2 needs still further evaluation, as it has so far been conducted only for the densely vegetated Amazonian ecosystem by Mallick et al. (2016). It should also be noted that the now used 8-day MODIS data is providing only a sub-daily estimate, and scaling these estimates into robust daily or monthly values still needs validation. In addition, one critical aspect is that the STIC1.2 model performance should be tested when all the needed model inputs are retrieved from satellites as the previous studies have been using the model inputs provided partly by EC towers.

References

Agam, N. and Berliner, P. 2006. Dew formation and water vapor adsorption in semi-arid environments–A review. Journal of Arid Environments, 65(4): 572–590. doi:10.1016/j.jaridenv.2005.09.004.

Alfieri, J., Kustas, W., Prueger, J., Hipps, L., Evett, S., Basara, J., Neale, C., French, A., Colaizzi, P., Agam, N., Cosh, M., Chavez, J. and Howell, T. 2012. On the discrepancy between eddy covariance and lysimetry-based surface flux measurements under strongly advective conditions. Advances in Water Resources, 50: 62–78. doi:10.1016/j.advwatres.2012.07.008.

Allen, R., Pereira, L., Raes, D. and Smith, M. 1998. Crop evapotranspiration - Guidelines for computing crop water requirements. 1st ed. Rome: Food and Agriculture Organization of the United Nations (FAO). Irrigation and drainage paper 56. Available at: http://www.fao.org/docrep/x0490e/x0490e07.htm.

Anderson, M., Norman, J., Kustas, W., Houborg, R., Starks, P. and Agam, N. 2008. A thermal-based remote sensing technique for routine mapping of land-surface carbon, water and energy fluxes from field to regional scales. Remote Sensing of Environment, 112(12): 4227–4241. doi:10.1016/j.rse.2008.07.009.

Anderson, M., Allen, R., Morse, A. and Kustas, W. 2012. Use of Landsat thermal imagery in monitoring evapotranspiration and managing water resources. Remote Sensing of Environment, 122: 50–65. doi:10.1016/j.rse.2011.08.025.

Baldocchi, D., Luxmoore, R. and Hatfield, J. 1991. Discerning the forest from the trees: an essay on scaling canopy stomatal conductance. Agricultural and Forest Meteorology, 54(2–4): 197–226. doi:10.1016/0168-1923(91)90006-c.

Beringer, J., Hutley, L., McHugh, I., Arndt, S., Campbell, D., Cleugh, H., Cleverly, J., Resco de Dios, V., Eamus, D., Evans, B., Ewenz, C., Grace, P., Griebel, A., Haverd, V., Hinko-Najera, N., Huete, A., Isaac, P., Kanniah, K., Leuning, R., Liddell, M., Macfarlane, C., Meyer, W., Moore, C., Pendall, E., Phillips, A., Phillips, R., Prober, S., Restrepo-Coupe, N., Rutledge, S., Schroder, I., Silberstein, R., Southall, P., Sun, M., Tapper, N., van Gorsel, E., Vote, C., Walker, J. and Wardlaw, T. 2016. An introduction to the Australian and New Zealand flux tower network–OzFlux. Biogeosciences Discussions, 13(21): 5895–5916). doi:10.5194/bg-13-5895-2016.

Boegh, E., Soegaard, H. and Thomsen, A. 2002. Evaluating evapotranspiration rates and surface conditions using Landsat TM to estimate atmospheric resistance and surface resistance. Remote Sensing of Environment, 79(2–3): 329–343. doi:10.1016/S0034-4257(01)00283-8.

Boegh, E. and Soegaard, H. 2004. Remote sensing based estimation of evapotranspiration rates. International Journal of Remote Sensing, 25(13): 2535–2551. doi:10.1080/01431160310001647975.

Bonan, G. 2002. Ecological climatology. 1st ed. New York: Cambridge University Press. 690 pp. ISBN 0521800323. Available at: http://www.cgd.ucar.edu/tss/aboutus/staff/bonan/ecoclim/index-2002.htm.

Bowen, I. 1926. The Ratio of Heat Losses by Conduction and by Evaporation from any Water Surface. Physical Review, 27(6): 779–787. doi:10.1103/PhysRev.27.779.

Brutsaert, W. and Stricker, H. 1979. An advection-aridity approach to estimate actual regional evapotranspiration. Water Resources Research, 15(2): 443–450. doi:10.1029/WR015i002p00443.

Burba, G. 2013. Eddy Covariance Method for Scientific, Industrial, Agricultural, and Regulatory Applications: A Field Book on Measuring Ecosystem Gas Exchange and Areal Emission Rates. Lincoln, USA: LI-COR Biosciences. 331 pp. ISBN 978-0-615-76827-4.

Chávez, J., Neale, C., Hipps, L., Prueger, J. and Kustas, W. 2005. Comparing Aircraft-Based Remotely Sensed Energy Balance Fluxes with Eddy Covariance Tower Data Using Heat Flux Source Area Functions. Journal of Hydrometeorology, 6(6): 923–940. doi: 10.1175/jhm467.1.

Dhungel, R., Allen, R., Trezza, R. and Robison, C. 2014. Comparison of Latent Heat Flux Using Aerodynamic Methods and Using the Penman–Monteith Method with Satellite-Based Surface Energy Balance. Remote Sensing, 6(9): 8844–8877. doi:10.3390/rs6098844.

Decker, M., Pitman, A. and Evans, J. 2013. Groundwater constraints on simulated transpiration variability over Southeastern Australian forests. Journal of Hydrometeorology, 14(2): 543–559. doi:10.1175/jhm-d-12-058.1.

Dirmeyer, P. 2011. The terrestrial segment of soil moisture-climate coupling. Geophysical Research Letter, 38(16): L16702. doi:10.1029/2011GL048268.

Encyclopædia Britannica. 2008. Water cycle. [Visited 21.9.2016]. Available at: https://global.britannica.com/science/water-cycle.

Ershadi, A., McCabe, M., Evans, J., Chaney, N. and Wood, E. 2014. Multi-site evaluation of terrestrial evaporation models using FLUXNET data. Agricultural and Forest Meteorology, 187: 46–61. doi:10.1016/j.agrformet.2013.11.008.

Fatichi, S. and Ivanov V. 2014. Interannual variability of evapotranspiration and vegetation productivity. Water Resources Research, 50(4): 3275–3294. doi:10.1002/2013wr015044.

Fisher, J., Tu, K. and Baldocchi, D. 2008. Global estimates of the land–atmosphere water flux based on monthly AVHRR and ISLSCP-II data, validated at 16 FLUXNET sites. Remote Sensing of Environment, 112(3): 901–919. doi:10.1016/j.rse.2007.06.025.

FLUXNET. 2016. Site Data Availability. [Visited 21.09.2016]. Available at: https://fluxnet.ornl.gov/site_status.

García, M., Oyonarte, C., Villagarcía, L., Contreras, S., Domingo, F. and Puigdefábregas, J. 2008. Monitoring land degradation risk using ASTER data: The non-evaporative fraction as an indicator of ecosystem function. Remote Sensing of Environment, 112(9): 3720–3736. doi:10.1016/j.rse.2008.05.011.

Glenn, E., Doody, T., Guerschman, J., Huete, A., King, E., McVicar, T., Van Dijk, A., Van Niel, T., Yebra, M. and Zhang, Y. 2011. Actual evapotranspiration estimation by ground and remote sensing methods: the Australian experience. Hydrological Processes, 25(26): 4103–4116. doi:10.1002/hyp.8391.

Guerschman, J., Van Dijk, A., Mattersdorf, G., Beringer, J., Hutley, L., Leuning, R., Pipunic, R. and Sherman, B. 2009. Scaling of potential evapotranspiration with MODIS data reproduces flux observations and catchment water balance observations across Australia. Journal of Hydrology, 369(1-2): 107–119. doi:10.1016/j.jhydrol.2009.02.013.

Henderson-Sellers, B. 1986. Calculating the surface energy balance for lake and reservoir modeling: A review. Reviews of Geophysics, 24(3): 625. doi:10.1029/rg024i003p00625.

Hulley, G., Hook, S. and Baldrige, A. 2010. Investigating the effects of soil moisture on thermal infrared land surface temperature and emissivity using satellite retrievals and laboratory measurements. Remote Sensing of Environment, 114(7): 1480–1493. doi:10.1016/j.rse.2010.02.002.

Hulley, G., Hughes, T. and Hook, S. 2012. Quantifying uncertainties in land surface temperature (LST) and emissivity retrievals from ASTER and MODIS thermal infrared data. Journal of Geophysical Research-Atmosphere, 117(23): D23113. doi:10.1029/2012JD018506.

Hulley, G., Hook, S., Abbott, E., Malakar, N., Islam, T. and Abrams, M. 2015. The ASTER Global Emissivity Dataset (ASTER GED): Mapping Earth's emissivity at 100 meter spatial scale. Geophysical Research Letters, 42(19): 7966–7976. doi:10.1002/2015gl065564.

Isaac, P., Cleverly, J., McHugh, I., van Gorsel, E., Ewenz, C. and Beringer, J. 2016. OzFlux Data: Network integration from collection to curation. Biogeosciences Discussions. In review. doi:10.5194/bg-2016-189.

Jackson, R., Idso, S., Reginato, R. and Pinter Jr., P. 1981. Canopy temperature as a crop water stress indicator. Water Resources Research, 17(4): 1133–1138. doi: 10.1029/wr017i004p01133.

Jackson, R., Kustas, W. and Choudhury, B. 1988. A re-examination of the crop water stress index. Irrigation Science, 9(4): 309–317. doi:10.1007/BF00296705.

Jarvis, P. 1976. The Interpretation of the Variations in Leaf Water Potential and Stomatal Conductance Found in Canopies in the Field. Philosophical Transactions of the Royal Society B: Biological Sciences, 273(927), 593–610. doi:10.1098/rstb.1976.0035.

Jarvis, P. and McNaughton, K. 1986. Stomatal control of transpiration: scaling up from leaf to region. Advances in Ecological Research, 15: 1–49. doi:10.1016/s0065-2504(08)60119-1.

Kalma, J., McVicar, T. and McCabe, M. 2008. Estimating Land Surface Evaporation: A Review of Methods Using Remotely Sensed Surface Temperature Data. Surveys in Geophysics, 29(4-5): 421–469. doi:10.1007/s10712-008-9037-z.

Koster, R., Salvucci, G., Rigden, A., Jung, M., Collatz, G. and Schubert, S. 2015. The pattern across the continental United States of evapotranspiration variability associated with water availability. Frontiers in Earth Sciences, 3. doi:10.3389/feart.2015.00035.

Kumagai, T., Saitoh, T., Sato, Y., Morooka, T., Manfroi, O., Kuraji, K. and Suzuki, M. 2004. Transpiration, canopy conductance and the decoupling coefficient of a lowland mixed dipterocarp forest in Sarawak, Borneo: dry spell effects. Journal of Hydrology, 287(1-4): 237–251. doi:10.1016/j.jhydrol.2003.10.002.

Lauenroth, W. and Bradford, J. 2006. Ecohydrology and the Partitioning AET Between Transpiration and Evaporation in a Semiarid Steppe. Ecosystems, 9(5): 756–767. doi:10.1007/s10021-006-0063-8.

Legates, D. and McCabe, G. 1999. Evaluating the use of "goodness-of-fit" Measures in hydrologic and hydroclimatic model validation. Water Resources Research, 35(1): 233–241. doi:10.1029/1998WR900018.

Leuning, R., Zhang, Y., Rajaud, A., Cleugh, H. and Tu, K. 2008. A simple surface conductance model to estimate regional evaporation using MODIS leaf area index and the Penman-Monteith equation. Water Resources Research, 44(10): W10419. doi: 10.1029/2007WR006562.

Li, J., Li, J., Weisz, E. and Zhou, D. 2007. Physical retrieval of surface emissivity spectrum from hyperspectral infrared radiances. Geophysical Research Letters, 34(16): L16812. doi:10.1029/2007GL030543.

Liou, Y. and Kar, S. 2014. Evapotranspiration Estimation with Remote Sensing and Various Surface Energy Balance Algorithms - A Review. Energies, 7(5): 2821–2849. doi: 10.3390/en7052821.

Liu, K., Wu, Y., McHugh, M., Baled, H., Enick, R. and Morreale, B. 2010. Equation of state modeling of high-pressure, high-temperature hydrocarbon density data. The Journal of Supercritical Fluids, 55(2): 701–711. doi:10.1016/j.supflu.2010.10.004.

LP DAAC. (2016a). Dataset Discovery - NASA Land Data Products and Services - MOD11A2. [Visited 21.9.2016]. Available at: https://lpdaac.usgs.gov/dataset_discovery/modis/modis_products_table/mod11a2.

LP DAAC. (2016b). Dataset Discovery - NASA Land Data Products and Services - MOD09A1. [Visited 21.9.2016]. Available at: https://lpdaac.usgs.gov/dataset_discovery/modis/modis_products_table/mod09a1.

Lundin, L-C. 2000. Sustainable Water Management in the Baltic Sea Basin, Book 2: Water use and Management. Uppsala, Sweden: Uppsala University. 240 pp. A Baltic University Programme Publication. ISBN 91-973579-4-4.

Ma, W., Hafeez, M., Ishikawa, H. and Ma, Y. 2012. Evaluation of SEBS for estimation of actual evapotranspiration using ASTER satellite data for irrigation areas of Australia. Theoretical and Applied Climatology, 112(3–4): 609–616. doi:10.1007/s00704-012-0754-3.

Mallick, K., Jarvis, A., Boegh, E., Fisher, J., Drewry, D., Tu, K., Hook, S., Hulley, G., Ardö, J., Beringer, J., Arain, A. and Niyogi, D. 2014. A Surface Temperature Initiated Closure (STIC) for surface energy balance fluxes. Remote Sensing of Environment, 141: 243–261. doi: 10.1016/j.rse.2013.10.022.

Mallick, K., Boegh, E., Trebs, I., Alfieri, J., Kustas, W., Prueger, J., Niyogi, D., Das, N., Drewry, D., Hoffmann, L. and Jarvis, A. 2015. Reintroducing radiometric surface temperature into the Penman-Monteith formulation. Water Resources Research, 51(8): 6214–6243. doi:10.1002/2014WR016106.

Mallick, K., Trebs, I., Boegh, E., Giustarini, L., Schlerf, M., Drewry, D., Hoffmann, L., von Randow, C., Kruijt, B., Araùjo, A., Saleska, S., Ehleringer, J., Domingues, T., Ometto, J., Nobre, A., de Moraes, O., Hayek, M., Munger, J. and Wofsy, S. 2016. Canopy-scale biophysical controls of transpiration and evaporation in the Amazon Basin. Hydrology and Earth System Sciences Discussions, 20(10): 4237–4264. doi:10.5194/hess-20-4237-2016.

Masiello, G., Serio C., Venafra, S., DeFeis, I. and Borbas, E. 2014. Diurnal variation in Sahara desert sand emissivity during the dry season from IASI observations. Journal of Geophysical Research-Atmosphere, 119(3): 1626–1638. doi:10.1002/jgrd.50863.

Masseroni, D., Corbari, C. and Mancini, M. 2014. Limitations and improvements of the energy balance closure with reference to experimental data measured over a maize field. Atmósfera, 27(4): 335–352. doi:10.1016/s0187-6236(14)70033-5.

Meyer, W., Kondrlovà, E. and Koerber, G. 2015. Evaporation of perennial semi-arid woodland in southeastern Australia is adapted for irregular but common dry periods. Hydrological Processes, 29(17): 3714–3726. doi:10.1002/hyp.10467.

Miura, T., Yoshioka, H., Fujiwara, K. and Yamamoto, H. 2008. Inter-comparison of ASTER and MODIS surface reflectance and vegetation index products for synergistic applications to natural resource monitoring. Sensors, 8(4): 2480–2499. doi:10.3390/s8042480.

Monteith, J. 1965. Evaporation and environment. In: Fogg, G. (ed.) The State and Movement of Water in Living Organisms. Symposia of the Society for Experimental Biology, 19. London, UK: Cambridge University Press. pp. 205–234.

Moran, M., Rahman, A., Washburne, J., Goodrich, D., Weltz, M. and Kustas, W. 1996. Combining the Penman-Monteith equation with measurements of surface temperature and

reflectance to estimate evaporation rates of semiarid grassland. Agricultural and Forest Meteorology, 80(2–4): 87–109. doi:10.1016/0168-1923(95)02292-9.

Morillas, L., García, M., Nieto, H., Villagarcía, L., Sandholt, I., Gonzalez-Dugo, M., Zarco-Tejada, P. and Domingo, F. 2013. Using radiometric surface temperature for energy flux estimation in Mediterranean drylands from a two-source perspective. Remote Sensing of Environment, 136: 234–246. doi:10.1016/j.rse.2013.05.010.

NASA. 1999a. Science writers' guide to Terra. Greenbelt, USA: NASA Earth Observing System Project Science Office. 28 pp. [Visited 21.9.2016]. Available at: http://terra.nasa.gov/wp-content/uploads/2014/04/Terra-Science-Writer-Guide-terra_sw_guide.pdf.

NASA. 1999b. Terra: Flagship of the Earth Observing System. Press Kit. [Visited 21.9.2016]. Available at: http://terra.nasa.gov/wp-content/uploads/2014/04/Terra-Press-Kit-terra_press_kit.pdf.

NASA. 2016a. MODIS - About. [Visited 21.9.2016]. Available at: https://modis.gsfc.nasa.gov/about/.

NASA. 2016b. MODIS - About - MODIS Design. [Visited 21.9.2016]. Available at: https://modis.gsfc.nasa.gov/about/design.php.

NASA. 2016c. About Terra. [Visited 21.9.2016]. Available at: http://terra.nasa.gov/about.

NASA. 2016d. MODIS land team – Validation - Status for: Land Surface Temperature and Emissivity (MOD11). [Visited 13.12.2016]. Available at: https://landval.gsfc.nasa.gov/ProductStatus.php?ProductID=MOD11.

O'Grady, A., Eamus, D. and Hutley, L. 1999. Transpiration increases during the dry season: patterns of tree water use in eucalypt open-forests of northern Australia. Tree Physiology, 19(9): 591–597. doi:10.1093/treephys/19.9.591.

ORNL DAAC. 2016. Global Subsetting Tool: MODIS Land Products. [Visited 31.10.2016]. Available at: http://daacmodis.ornl.gov/cgi-bin/MODIS/GLBVIZ_1_Glb/modis_subset_order_global_col5.pl.

OzFlux. 2016a. Home - Welcome to OzFlux. [Visited 19.9.2016]. Available at: http://www.ozflux.org.au/.

OzFlux. 2016b. OzFlux - Monitoring Sites. [Visited 19.9.2016]. Available at: http://www.ozflux.org.au/monitoringsites/index.html.

Peel, M., Finlayson, B. and McMahon, T. 2007. Updated world map of the Köppen-Geiger climate classification. Hydrology and Earth System Sciences Discussion, 4(2): 439–473. doi:10.5194/hessd-4-439-2007.

Penman, H. 1948. Natural Evaporation from Open Water, Bare Soil and Grass. Proceedings of the Royal Society A: Mathematical, Physical and Engineering Sciences, 193(1032): 120–145. doi:10.1098/rspa.1948.0037.

Polhamus, A., Fisher, J. and Tu, K. 2013. What controls the error structure in evapotranspiration models?. Agricultural and Forest Meteorology, 169: 12–24. doi:10.1016/j.agrformet.2012.10.002.

Priestley, C. and Taylor, R. 1972. On the Assessment of Surface Heat Flux and Evaporation Using Large-Scale Parameters. Monthly Weather Review, 100(2): 81–92. doi:10.1175/1520-0493(1972)100<0081:otaosh>2.3.co;2.

Risbey, J., Pook, M., McIntosh, P., Wheeler, M. and Hendon, H. 2009. On the Remote Drivers of Rainfall Variability in Australia. Monthly Weather Review, 137(10): 3233–3253. doi:10.1175/2009MWR2861.1.

Rochford, P. 2015. Skill Metrics Toolbox. Toolbox for Matlab. [Visited 3.10.2016]. Available at: https://se.mathworks.com/matlabcentral/fileexchange/52943-skill-metrics-toolbox.

Shuttleworth, W., and Wallace, J. 1985. Evaporation from sparse crops – an energy combination theory, Quarterly Journal of the Royal Meteorological Society, 111(469): 839–855. doi:10.1002/qj.49711146910.

Shuttleworth, W., Leuning, R., Black, T., Grace, J., Jarvis, P., Roberts, J. and Jones, H. 1989. Micrometeorology of Temperate and Tropical Forest [and Discussion]. Philosophical Transactions of the Royal Society B: Biological Sciences, 324(1223): 299–334. doi:10.1098/rstb.1989.0050.

Sommer, B., Boggs, D., Boggs, G., van Dijk, A. and Froend, R. 2016. Spatio-temporal patterns of evapotranspiration from groundwater-dependent vegetation. Ecohydrology, 9(8): 1620–1629. doi:10.1002/eco.1752.

Sun, D. and Pinker R. 2003. Estimation of land surface temperature from a Geostationary Operational Environmental Satellite (GOES-8). Journal of Geophysical Research, 108(D11): 4326. doi:10.1029/2002JD002422.

Taylor, K. 2001. Summarizing multiple aspects of model performance in a single diagram. Journal of Geophysical Research: Atmospheres, 106(D7): 7183–7192. doi:10.1029/2000jd900719.

UCLA. 2016. FAQ: What is the coefficient of variation?. [Visited 5.12.2016]. Available at: http://www.ats.ucla.edu/stat/mult_pkg/faq/general/coefficient_of_variation.htm.

Velpuri, N., Senay, G., Singh, R., Bohms, S. and Verdin, J. 2013. A comprehensive evaluation of two MODIS evapotranspiration products over the conterminous United States: Using point and gridded FLUXNET and water balance ET. Remote Sensing of Environment, 139: 35–49. doi:10.1016/j.rse.2013.07.013.

Venturini, V., Islam, S. and Rodriguez, L. 2008. Estimation of evaporative fraction and evapotranspiration from MODIS products using a complementary based model. Remote Sensing of Environment, 112(1): 132–141. doi:10.1016/j.rse.2007.04.014.

Vinukollu, R., Wood, E., Ferguson, C. and Fisher, J. 2011. Global estimates of evapotranspiration for climate studies using multi-sensor remote sensing data: Evaluation of three process-based approaches. Remote Sensing of Environment, 115(3): 801–823. doi:10.1016/j.rse.2010.11.006.

Wang, K. and Dickinson, R. 2012. A review of global terrestrial evapotranspiration: Observation, modeling, climatology, and climatic variability. Reviews of Geophysics, 50(2): RG2005. doi:10.1029/2011rg000373.

Weier, J. and Herring, D. 2000. Measuring vegetation (*NDVI* & EVI).[Visited 13.12.2016]. Available at: http://earthobservatory.nasa.gov/Features/MeasuringVegetation/measuring_vegetation_1.php.

Williams, I. and Torn, M. 2015. Vegetation controls on surface heat flux partitioning, and land-atmosphere coupling. Geophysical Research Letters, 42(21): 9416–9424, doi:10.1002/2015GL066305.

Willmott, C. 1982. Some comments on the evaluation of model performance. Bulletin American Meteorological Society, 63(11): 1309–1313. doi:10.1175/1520-0477(1982)063<1309:scoteo>2.0.co;2.

Yebra, M., Van Dijk, A., Leuning, R., Huete, A. and Guerschman, J. 2013. Evaluation of optical remote sensing to estimate actual evapotranspiration and canopy conductance. Remote Sensing of Environment, 129: 250–261. doi:10.1016/j.rse.2012.11.004.

List of appendices

Appendix 1 Derivation of STIC1.2 and Bowen ratio closure

A1 Derivation of state variables g_A, g_C, T_0 and Λ

A1.1 Expression for g_A and g_C (following Mallick et al., 2014, 2015, 2016)

The surface energy balance equation can be expressed as follows:

$$\phi = H + \lambda E \tag{A1}$$

where ϕ is the net available energy ($\cong R_N - G$) (W m^{-2}), H the sensible heat flux (W m^{-2}), λE the latent heat flux (W m^{-2}), R_N the net radiation (W m^{-2}) and G the ground heat flux (W m^{-2}).

The sensible and latent heat fluxes can be expressed according to the aerodynamic transfer equations (Boegh et al., 2002; Boegh and Soegaard, 2004):

$$H = \rho c_P g_A (T_O - T_A) \tag{A2}$$

$$\lambda E = \frac{\rho c_P}{\gamma} g_A (e_0 - e_A) = \frac{\rho c_P}{\gamma} g_C (e_0^* - e_0) \tag{A3}$$

where λ is the latent heat of evaporation (J kg^{-1}), ρ the air density (kg m^{-3}), c_P the specific heat of dry air (MJ kg^{-1} K^{-1}), g_A the aerodynamic conductance (m s^{-1}), g_C the canopy conductance (m s^{-1}), T_0 the aerodynamic temperature (°C), T_A the air temperature (°C), γ the psychrometric constant (hPa K^{-1}), e_0 the atmospheric vapor pressure at the source/sink height (hPa), e_0^* the saturation vapor pressure at the source/sink height (hPa) and e_A the atmospheric vapor pressure at the level of T_A measurements (hPa). By combining equations (A1)–(A3) and solving for g_A, the equation of g_A can be expressed as follows:

$$g_A = \frac{\phi}{\rho c_P \left[(T_O - T_A) + \left(\frac{e_0 - e_A}{\gamma}\right)\right]} \tag{A4}$$

Combining the aerodynamic equations of λE (A3) and solving for g_C, the expression of g_C is as follows:

$$g_C = g_A \frac{(e_0 - e_A)}{(e_0^* - e_A)} \tag{A5}$$

A1.2 Expression for T_0 (following Mallick et al., 2014, 2015, 2016):

An expression of T_0 can be derived from evaporative fraction (Λ) and the Bowen ratio (β) (Bowen, 1926) equation, which is expressed as follows:

$$\beta = \gamma \frac{(T_0 - T_A)}{(e_0 - e_A)} \tag{A6}$$

Assuming a surface balance closure, β can be expressed in terms of Λ ($= \frac{\lambda E}{H + \lambda E}$) (Shuttleworth et al., 1989):

$$\beta = \frac{1-\Lambda}{\Lambda} \tag{A7}$$

Combining equations (A6) and (A7) and solving for T_0, we get:

$$T_0 = T_A + \left(\frac{e_0 - e_A}{\gamma}\right)\left(\frac{1-\Lambda}{\Lambda}\right) \tag{A8}$$

A1.3 Expression for Λ (following Mallick et al. 2014, 2015, 2016):

One of the key novelties of the STIC framework is the derivation of Λ. The derivation is based on advection-aridity (AA) hypothesis by Brutsaert and Stricker (1979). Mallick et al. (2015) introduced a water stress constraint in the original AA hypothesis to find an expression of Λ by using the modified AA hypothesis in conjunction with evapotranspiration according to Penman-Monteith (Monteith, 1965). The modified form of AA hypothesis can be expressed as follows:

$$E_{PM}^* = 2E_{PT}^* - E \tag{A9}$$

where E_{PM}^* is the potential evapotranspiration for any surface based on Penman-Montheith and E_{PT}^* the potential evapotranspiration according to Priestley-Taylor (Priestley and Taylor, 1972). Dividing both sides of Equation A9 by E, we get the following result:

$$\frac{E}{E_{PM}^*} = \frac{E}{2E_{PT}^* - E} \tag{A10}$$

By dividing both numerator and denominator of the right of the equation by E_{PT}^*, we are able to write the equation as follows:

$$\frac{E}{E_{PM}^*} = \frac{\frac{E}{E_{PT}^*}}{2 - \frac{E}{E_{PT}^*}} \tag{A11}$$

Assuming that E_{PT}^* is a modification of E_{PM}^* for any surface, we can derive an expression for E_{PT}^* as follows:

$$E_{PM}^* = \frac{s\phi + \rho c_P g_A D_A}{s + \gamma\left(1 + \frac{g_A}{g_{Cmax}}\right)} \tag{A12}$$

$$= \frac{s\phi}{s + \gamma\left(1 + \frac{g_A}{g_{Cmax}}\right)}\left(1 + \frac{\rho c_P g_A D_A}{s\phi}\right)$$

$$= \frac{\alpha s\phi}{s + \gamma\left(1 + \frac{g_A}{g_{Cmax}}\right)} = E_{PT}^* \tag{A13}$$

where s is the slope of the saturation vapor pressure versus air temperature (hPa K^{-1}), D_A is the saturation deficit of the air (hPa) or vapor pressure deficit at the reference level and α is the unitless Priestley-Taylor parameter. g_{Cmax} is described as the maximum g_C value under the predominant atmospheric conditions, and moisture availability (M) is the limiting factor that prevents g_C to reach g_{Cmax}. Therefore, we can define g_{Cmax} as the ratio of g_C and M similarly than Jarvis (1976) and Baldocchi et al. (1991):

$$g_{Cmax} = \frac{g_C}{M} \tag{A14}$$

If net available energy (ϕ) is expressed as $\phi = E/\Lambda$, we can express E/E_{PT}^* as follows:

$$\frac{E}{E_{PT}^*} = \frac{\Lambda\left[s+\gamma\left(1+\frac{g_A}{g_{Cmax}}\right)\right]}{\alpha s} \tag{A15}$$

Combining Equations A11 and A15, and substituting E/E_{PT}^*, we can obtain the following form:

$$\frac{E}{E_{PM}^*} = \frac{\Lambda\left[s+\gamma\left(1+\frac{g_A}{g_{Cmax}}\right)\right]}{2\alpha s - \Lambda\left[s+\gamma\left(1+\frac{g_A}{g_{Cmax}}\right)\right]} \tag{A16}$$

On the other hand, we are able to write the ratio of E/E_{PM}^* according to the PM equations by Monteith (1965):

$$\frac{E}{E_{PM}^*} = \frac{\frac{s\phi+\rho c_P g_A D_A}{s+\gamma\left(1+\frac{g_A}{g_C}\right)}}{\frac{s\phi+\rho c_P g_A D_A}{s+\gamma\left(1+\frac{g_A}{g_{Cmax}}\right)}} = \frac{s+\gamma\left(1+\frac{g_A}{g_{Cmax}}\right)}{s+\gamma\left(1+\frac{g_A}{g_C}\right)} \tag{A17}$$

Now we are able to combine equations A16 and A17, and substitute g_{Cmax} according to Equation A14 to get the following result:

$$\frac{s+\gamma\left(1+\frac{Mg_A}{g_C}\right)}{s+\gamma\left(1+\frac{g_A}{g_C}\right)} = \frac{\Lambda\left[s+\gamma\left(1+\frac{Mg_A}{g_S}\right)\right]}{2\alpha s - \Lambda\left[s+\gamma\left(1+\frac{Mg_A}{g_S}\right)\right]} \tag{A18}$$

Finally, we can solve equation A18 for Λ:

$$\Lambda = \frac{2\alpha}{2s+2\gamma+\gamma\frac{g_A}{g_C}(1+M)} \tag{A19}$$

To solve the state equations presented above, we need to derive expressions for e_0^*, e_0, M and α.

A2 Derivation of the unknowns e_0, e_0, M and α*

A2.1 Derivation of e_0^* and e_0 (following Mallick et al., 2016):

Saturation vapor pressure at the source/sink height (e_0^*) can be derived from the aerodynamic equation (A3) as follows:

$$\lambda E = \frac{\rho c_P}{\gamma} g_A (e_0 - e_A) = \frac{\rho c_P}{\gamma} g_C (e_0^* - e_0) \rightarrow \lambda E = \frac{\rho c_P}{\gamma} \frac{g_A g_C}{g_A + g_C} (e_0^* - e_A) \tag{A20}$$

$$e_0^* = e_a + \left[\frac{\gamma \lambda E (g_A + g_C)}{\rho c_P g_A g_C}\right] \tag{A21}$$

The atmospheric vapor pressure deficit (D_0) and vapor pressure at the source/sink height (e_0) can be expressed as (Shuttlewort and Wallace, 1985):

$$D_0 = D_A + \left[\frac{\{s\emptyset - (s+\gamma)\lambda E\}}{\rho c_P g_A}\right] \tag{A22}$$

$$e_0 = e_0^* - D_0 \tag{A23}$$

A2.2 Derivation of *M* (following Mallick et al., 2015, 2016):

M can be expressed as following Venturini et al. (2008):

$$M=\frac{(e_0-e_A)}{(e_0^*-e_A)}=\frac{(e_0-e_A)}{\kappa(e_S^*-e_A)}=\frac{s_1(T_{SD}-T_D)}{\kappa s_2(T_R-T_D)} \tag{A24}$$

where T_{SD} is the dew-point temperature at the source/sink height (ºC), T_D is the dew-point temperature (ºC), T_R is the radiometric surface temperature (ºC), κ is the ratio between (e_0^*–e_A) and (e_S^*–e_A) (unitless), s_1 is the ratio of difference in temperature (T_{SD}–T_R) to difference in vapor pressure (e_0–e_A) (hPa K^{-1}) and s_2 is the ratio of difference in temperature (T_R–T_D) to difference in vapor pressure (e_S^*–e_A) (hPa K^{-1}).

Equation of T_{SD} can be found using aerodynamic equation of λE:

$$\lambda E = \frac{\rho c_P}{\gamma} g_A(e_0 - e_A) = \frac{\rho c_P}{\gamma} g_A s_1(T_{SD} - T_D) \rightarrow T_{SD} = T_D + \frac{\gamma \lambda E}{\rho c_P g_A s_1} \tag{A25}$$

We assume that *M* is an indicator of surface wetness that controls only evaporation from the upper part of the surface. However, if λE is limited because of low surface wetness and high D_A demand, we assume that root-zone moisture becomes dominant. In these cases, the optional expression of *M* is as follows (for detailed derivations please see Mallick et al., 2015):

$$M=\frac{\gamma s_1(T_{SD}-T_D)}{s_3(T_R-T_{SD})s+\gamma s_4(T_A-T_D)} \tag{A26}$$

where s_4 is the ratio of difference in temperature (T_A–T_D) to difference in vapor pressure (e_0–e_A) (hPa K^{-1}). Equation A26 for *M* is applied if potential evaporation by Penman is more than net radiation ($\lambda E_P^* = \frac{s\phi+\rho c_P g_A D_A}{s+\gamma} > \emptyset$) or T_D is less than 0.

A2.3 Derivation of *α* (following Mallick et al., 2016):

An equation of α can be derived from the aerodynamic equations of *H* and λE (Equations A2 and A3) by substituting these into to following equation of Λ:

$$\Lambda = \frac{\lambda E}{H+\lambda E} \tag{A27}$$

$$= \frac{\frac{\rho c_P}{\gamma}\frac{g_A g_C}{g_A+g_C}(e_0^*-e_A)}{\rho c_P g_A(T_O-T_A)+\frac{\rho c_P}{\gamma}\frac{g_A g_C}{g_A+g_C}(e_0^*-e_A)}$$

$$= \frac{g_C(e_0^*-e_A)}{[\gamma(T_0-T_A)(g_A+g_C)+g_C(e_0^*-e_A)]} \tag{A28}$$

and further combining Equations A28 and A19, eliminating Λ and solving for α, we get:

$$\alpha = \frac{g_C(e_0^*-e_A)\left[2s+2\gamma+\gamma\frac{g_A}{g_C}(1+M)\right]}{2s[\gamma(T_0-T_A)(g_A+g_C)+g_C(e_0^*-e_A)]} \tag{A29}$$

A3 Constants and initial values used in STIC1.2

A3.1 The used constants used in this study

The used constants used in this study are presented in Table A1.

Table A1 The used constants and their values

Constant	Symbol	Used value	Unit
Air density	ρ	1.234	kg/m^3
Latent heat of evaporation	Λ	2264.76	kJ/kg
Psychrometric constant	γ	0.67	hPa/K
Specific heat of air at constant pressure	c_p	1013	J/kg/K
Stefan-Boltzmann constant	σ	5.670×10^{-8}	J K^{-4} m^{-2} s^{-1}

A3.2 Psychrometric equations used in this study:

Initial values for saturation vapor pressures e_A^* and e_S^* are calculated as follows (modification of Clausius-Clapeyron equation):

$$e_A^* = 6.13753e^{\frac{17.27T_A}{T_A+273.3}} \quad \text{(A30)}$$

$$e_S^* = 6.13753e^{\frac{17.27T_R}{T_R+273.3}} \quad \text{(A31)}$$

By inverting Equation A30 and replacing e_A^* with e_A, we are able to find an estimate of T_D:

$$T_D = \frac{273.3\log(\frac{e_A}{6.13753})}{17.27-\log(\frac{e_A}{6.13753})} \quad \text{(A32)}$$

Values for e_A and D_A can be obtained as follows:

$$e_A = e_A^*\left(\frac{RH}{100}\right) \quad \text{(A33)}$$

$$D_A = e_A^* - e_A \quad \text{(A34)}$$

Slopes s, s_1 and s_3 and are calculated as follows (s as in Venturini et al., 2012, s_1 and s_3 as in Jackson et al., 1988):

$$s = 4098\frac{e_a^*}{(T_A-273.3)^2} \quad \text{(A35)}$$

$$s_1 = (45.03 + 3.014T_D + 0.05345T_D^2 + 0.00224T_D^3)^{-2} \quad \text{(A36)}$$

$$s_3 = (45.03 + 3.014T_R + 0.05345T_R^2 + 0.00224T_R^3)^{-2} \quad \text{(A37)}$$

Slope s_2 is calculated using Clausius-Clapeyron relationship, if the difference between T_R and T_A is more than 5°C or lower than -20°C. If the difference is outside this range, the assumption of linearity of the saturation vapor pressure and temperature might lead errors in the calculation (Mallick et al., 2015). In this case, s_2 is calculated similarly than s_3.

$$s_2 = \frac{(e_s^* - e_A)}{(T_R - T_D)}, \text{when } -20°\text{C} < (T_R - T_A) < 5°C \quad \text{(A38)}$$

$$s_2 = (45.03 + 3.014T_R + 0.05345T_R^2 + 0.00224T_R^3)^{-2} \quad \text{(A39)}$$

Slope s_4 is calculated as follows:

$$s_4 = \frac{(e_A^* - e_A)}{(T_A - T_D)} \quad \text{(A40)}$$

A3.3 Initial values and their equations used in this study (values changed after iteration):

Initial value for α is 1.26, and later it is estimated as presented in Equation A29. Initial value for the saturation vapor pressure e_0^* is calculated as follows:

$$e_0^* = 6.13753e^{\frac{17.27T_R}{T_R + 273.3}} \quad \text{(A41)}$$

The first estimate of T_{SD} is calculated as follows (for the derivation please see Mallick et al. 2014, 2015):

$$T_{SD} = \frac{(e_0^* - e_A) - s_3T_R + s_1T_D}{(s_1 - s_3)} \quad \text{(A42)}$$

The first estimate of e_0 is calculated as follows after the first estimate of M (Equation A24 or A26) (following Mallick et al., 2015, 2016):

$$e_0 = e_A + M(e_0^* - e_A) \quad \text{(A43)}$$

A4 Bowen ratio correction applied to measured surface flux data:

As the used input data is already level-3 corrected, we are using Bowen ratio correction only for surface fluxes λE and H following Chávez et al (2005). The used equations are as follows:

$$Available\ energy = R_N - G = (H + \Delta H) + (\lambda E + \Delta\lambda E) \quad \text{(A44)}$$

$$Bowen\ ratio = \beta = \frac{H + \Delta H}{\lambda E + \Delta\lambda E} \quad \text{(A45)}$$

By combining Equations A44 and A45, we get the presentation of $\Delta\lambda E$:

$$\Delta\lambda E = \left[(R_N - G) - \frac{\{(1+\beta)\lambda E\}}{(1+\beta)}\right] \quad \text{(A46)}$$

Further combining Equations A45 and A46, we can derive equation of ΔH, and finally close the energy balance:

$$\Delta H = [\beta(\lambda E + \Delta\lambda E) - H] \quad \text{(A47)}$$

$$\lambda E\ (closure) = \lambda E(measured) + \Delta\lambda E \quad \text{(A48)}$$

$$H\ (closure) = H(measured) + \Delta H \quad \text{(A49)}$$

In this study, Bowen ratio is expressed also as in Equation A7, and therefore we can express β as follows:

$$\beta = \frac{H}{\lambda E} \quad \text{(A50)}$$

Finally, using the Bowen ratio (Equation A50), we are able to estimate $\Delta\lambda E$ and ΔH followed by the closure of λE and H.

Table A2 An overview of the sites used in this study and their characteristics

Ecohydrological class	Site name	OzFlux ID	Region	Latitude (S) Longitude (E)	World ecoregion	Land cover
***P*<350 mm**	Alice Springs	AU-ASM	Northern Territory	-23.28° 133.25°	Deserts and Xeric shrublands	Semi-arid mulga (Acacia aneura) ecosystem
	Calperum	AU-Cpr	South Australia	-34.00° 140.59°	Mediterranean woodlands	Recovering mallee woodland
	Great Western Woodlands	AU-GWW	Western Australia	-30.19° 120.65°	Mediterranean woodlands	Temperate woodland, shrubland and mallee
	Ti Tree East	AU-TTE	Northern Territory	-22.29° 133.64°	Deserts and Xeric shrublands	Grassy mulga woodland and Corymbia/Triodia savanna
350<*P* <700 mm	Gingin	AU-Gin	Western Australia	-31.38° 115.71°	Mediterranean woodlands	Coastal heath Banksia woodland
	Jaxa (Yanco)	AU-Ync	New South Wales	-34.99° 146.29°	Temperate grassland	Grassland
	Riggs Creek	AU-Rig	Victoria	-36.65° 145.58°	Pasture	Dryland agriculture
	Sturt plains	AU-Stp	Northern Territory	-17.15° 133.35°	Tropical grassland	Low lying plain dominated by Mitchell Grass
	Whroo	AU-Whr	Victoria	-36.67° 145.03°	Temperate woodlands	Box woodland
	Wombat	AU-Wom	Victoria	-37.42° 144.09°	Temperate broadleaf forest	Dry sclerophyll eucalypt forest
***P*>700 mm**	Cowbay	AU-Cow	Queensland	-16.24° 145.43°	Tropical and sub-tropical moist broadleaf forests	Complex mesophyll vine forest
	Cumberland Plains	AU-Cum	New South Wales	-33.62° 150.72°	Temperate woodlands	Dry sclerophyll
	Dry River	AU-Dry	Northern Territory	-15.26° 132.37°	Tropical savannas	Open forest savanna
	Howard Springs	AU-How	Northern Territory	-12.49° 131.15°	Tropical savannas	Tropical savanna (wet)
	Tumbarumba	AU-Tum	New South Wales	-35.66° 148.15°	Temperate broadleaf and mixed forest	Wet temperate sclerophyll eucalypt

Table A3 The climatic and ecohydrological characteristics of the study sites and data availability

Ecohydrological class	OzFlux ID	Annual T_A (°C)	Annual P (mm)	Annual E (mm)	Annual E/R_N	Emissivity (ε)	Data availability λE & H (%)
P <350 mm	AU-ASM	-4 – 46	306	141	0.1	0.8	75
	AU-Cpr	12 – 45	240	257	0.13	0.8	75
	AU-GWW	5 – 33	240	135	0.17	0.81	80
	AU-TTE	-4 – 46	305	144	0.11	0.835	76
350<P<700 mm	AU-Gin	19 – 30	641	486	0.29	0.805	74
	AU-Ync	12 – 37	465	207	0.1	0.8	76
	AU-Rig	12 – 26	650	297	0.3	0.91	70
	AU-Stp	11 – 39	640	454	0.28	0.88	80
	AU-Whr	3 – 30	558	443	0.27	0.81	90
	AU-Wom	1 – 30	650	653	0.43	0.925	63
P>700 mm	AU-Cow	11 – 39	4000	745	0.61	0.955	78
	AU-Cum	3 – 29	800	486	0.43	0.885	85
	AU-Dry	14 – 37	895	679	0.47	0.97	65
	AU-How	20 – 33	1700	1190	0.56	0.87	86
	AU-Tum	-10 – 30	1000	955	0.68	0.97	79

Table A4 The Biome Properties Look-Up Table for MOD16 model. Biomes are ENF (evergreen needleleaf forest), EBF (evergreen broadleaf forest), DNF (deciduous needleleaf forest), DBF (deciduous broadleaf forest), MF (mixed forest), WL (woody savannas), SV (savannas), CSH (closed shrubland), OSH (open shrubland), Grass (grassland or urban and built-up, barren or sparsely vegetated), and Crop (cropland). (Following Mu et al., 2011.) Biome types for each OzFlux sites are checked at https://fluxnet.ornl.gov/site_status (FLUXNET, 2016).

Parameter	T_{min_open} (°C)	T_{min_close} (°C)	VPD_{close} (Pa)	VPD_{open} (Pa)	gl_{sh} (m s^{-1})	gl_{e_wv} (m s^{-1})	Cl (m/s)	RBL_{min} (s m^{-1})	RBL_{max} (s m^{-1})
ENF	8.31	−8.00	3000	650	0.04	0.04	0.0032	65.0	95.0
EBF	9.09	−8.00	4000	1000	0.01	0.01	0.0025	70.0	100.0
DNF	10.44	−8.00	3500	650	0.04	0.04	0.0032	65.0	95.0
DBF	9.94	−6.00	2900	650	0.01	0.01	0.0028	65.0	100.0
MF	9.50	−7.00	2900	650	0.04	0.04	0.0025	65.0	95.0
CSH	8.61	−8.00	4300	650	0.04	0.04	0.0065	20.0	55.0
OSH	8.80	−8.00	4400	650	0.04	0.04	0.0065	20.0	55.0
WL	11.39	−8.00	3500	650	0.08	0.08	0.0065	25.0	45.0
SV	11.39	−8.00	3600	650	0.08	0.08	0.0065	25.0	45.0
Grass	12.02	−8.00	4200	650	0.02	0.02	0.0070	20.0	50.0
Crop	12.02	−8.00	4500	650	0.02	0.02	0.0070	20.0	50.0

Table A5 Dry and wet seasons used in the study for 15 EC sites

Ecohydrological class	Site name	Season (months)		
***P*<350 mm**		Wet	Dry	Wet
	AU-ASM*	Jan-Apr	May-Oct	Nov-Dec
	AU-GWW*	Jan-May	Jun-Oct	Nov-Dec
	AU-TTE*	Jan-Feb	Mar-Oct	Nov-Dec
		Dry	Wet	Dry
	AU-Cpr*	Jan-Mar	Apr-Sep	Oct-Dec
350<*P*<700 mm		Wet	Dry	Wet
	AU-Stp	Jan-Mar	Apr-Oct	Nov-Dec
		Dry	Wet	Dry
	AU-Gin	Jan-Apr	May-Oct	Nov-Dec
	AU-Ync*	Jan-Mar	Apr-Sept	Oct-Dec
	AU-Rig	Jan-Mar	Apr-Sept	Oct-Dec
	AU-Whr	Jan-May	Jun-Sept	Oct-Dec
	AU-Wom	Jan-Apr	May-Oct	Nov-Dec
***P*>700 mm**		Wet	Dry	Wet
	AU-Cow	Jan-May	Jun-Oct	Nov-Dec
	AU-Cum	Jan-Apr	May-Oct	Nov-Dec
	AU-Dry	Jan-Mar	Apr-Oct	Nov-Dec
	AU-How	Jan-Mar	Apr-Oct	Nov-Dec
		Dry	Wet	Dry
	AU-Tum	Jan-Mar	Apr-Oct	Nov-Dec

Table A6 Error statistics of STIC1.2 derived sub-daily λE and H over 15 EC sites (* = statistics calculated using only positive values of λE and H)

Ecohydrological class	Site name	Year	λE				H			
			RMSD (W m^{-2})	R^2	*MAPD* (%)	$RMSD_S^2/RMSD^2$ (%)	*RMSD* (W m^{-2})	R^2	*MAPD* (%)	$RMSD_S^2/RMSD^2$ (%)
***P*<350 mm**	AU-ASM*	2013	29	0.23	73	60	25	0.99	9	2
		2014	39	0.60	52	52	35	0.97	14	14
	AU-Cpr*	2013	37	0.13	58	34	33	0.97	15	37
		2014	29	0.21	58	37	27	0.96	14	30
	AU-GWW*	2013	41	0.28	47	60	34	0.94	19	7
		2014	37	0.38	43	42	33	0.96	15	11
	AU-TTE*	2013	35	0.37	100	56	32	0.97	15	47
		2014	49	0.64	60	76	41	0.91	19	3
700>*P*> 350 mm	AU-Gin	2013	53	0.55	50	34	53	0.90	25	17
		2014	54	0.54	54	24	54	0.91	24	20
	AU-Ync*	2013	45	0.13	65	77	39	0.94	16	3
		2014	38	0.13	88	45	37	0.96	16	38
	AU-Rig	2013	63	0.43	61	51	63	0.84	33	34
		2014	61	0.36	79	45	61	0.86	45	44
	AU-Stp	2013	44	0.75	51	38	44	0.88	24	13
		2014	52	0.78	51	42	52	0.87	26	24
	AU-Whr	2013	43	0.56	51	21	43	0.94	21	18
		2014	47	0.58	50	32	47	0.93	24	18
	AU-Wom	2013	48	0.83	27	1	48	0.94	20	31
		2014	56	0.81	30	31	56	0.89	29	16
***P*>700 mm**	AU-Cow	2013	38	0.91	24	9	38	0.82	46	23
		2014	47	0.85	31	5	47	0.81	45	46
	AU-Cum	2013	51	0.81	41	25	51	0.89	36	14
		2014	52	0.77	40	8	52	0.90	31	22
	AU-Dry	2013	54	0.88	25	21	54	0.80	34	12
		2014	64	0.80	38	26	64	0.82	30	30
	AU-How	2013	57	0.88	25	7	57	0.80	38	42
		2014	59	0.87	26	16	59	0.79	38	25
	AU-Tum	2013	56	0.87	32	6	56	0.87	48	2
		2014	53	0.88	34	3	53	0.88	49	2

Table A7 Error statistics of STIC1.2, PT-JPL and MOD16 derived 8-day λE and H fluxes over 5 EC sites during the years 2013 and 2014

Site name	Model	λE				H			
		RMSD (W m^{-2})	R^2	*MAPD* (%)	$RMSD_S^2/RMSD^2$ (%)	*RMSD* (W m^{-2})	R^2	*MAPD* (%)	$RMSD_S^2/RMSD^2$ (%)
AU-ASM	STIC 1.2	69	0.26	96	36	69	0.42	21	28
	PT-JPL	49	0.61	99	73	49	0.9	12	62
	MOD16	400	0.01	100	98	401	0.16	100	98
AU-Dry	STIC 1.2	95	0.55	31	20	95	0.54	33	21
	PT-JPL	91	0.61	28	59	91	0.5	23	42
	MOD16	228	0.01	83	95	228	0.02	70	91
AU-How	STIC 1.2	97	0.49	5	5	97	0.61	40	18
	PT-JPL	82	0.7	23	52	82	0.75	33	54
	MOD16	157	0.01	43	79	159	0.00	60	85
AU-Stp	STIC 1.2	103	0.36	58	19	19	0.07	38	16
	PT-JPL	44	0.8	32	21	44	0.74	14	12
	MOD16	309	0.0004	95	95	309	0.01	100	95
AU-Tum	STIC 1.2	66	0.74	21	36	66	0.72	30	38
	PT-JPL	176	0.14	61	96	166	0.79	87	80
	MOD16	59	0.89	22	61	59	0.85	31	70